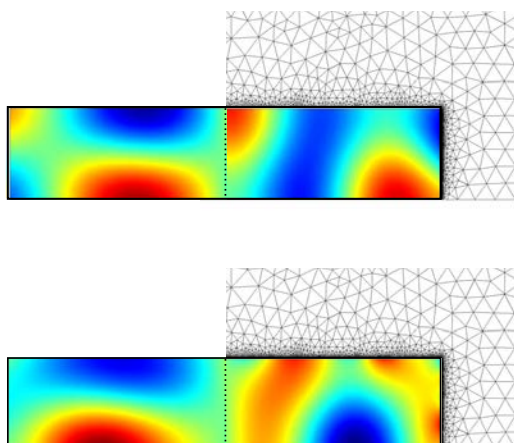**DTU Physics**
Department of Physics

Master's Thesis

Surface Acoustic Waves in Microfluidic Devices
Simulation and Instrumentation

Nils Refstrup Skov
s103403

Supervisor: Henrik Bruus

Department of Physics
Technical University of Denmark

18 March 2016

Abstract

In this thesis numeric models simulating first order acoustic fields in a Newtonian fluid domain bounded by a solid and an actuating surface are presented. The numeric models are used to investigate boundary conditions commonly used in microfluidic simulations to model either pressure or velocity fields along fluid-solid interfaces. The conditions are; 1) The hard wall condition, used to model fluid-solid interfaces assumed to not yield due to fluid pressure. 2) The lossy wall condition, used to model fluid-solid interfaces that yield, based on an the relation between the fluid and solid acoustic impedances.

By comparing the acoustic fields resulting from simulations coupling linear elasticity and fluid dynamics along interfaces, with simulations relying solely on fluid dynamics and aforementioned approximative boundary condition along boundaries, the validity of said approximations can be investigated.

The validity of the boundary conditions are found to depend on fluid and solid geometries as well as resonance with regards to the fluid-solid system. The hard wall was found to be a reasonable approximation solid domains were thick, and the system was actuated off-resonance with regards to the solid structure. The lossy wall condition was found to be a misrepresentation of the physical conditions along PDMS-solid interfaces. No cases in which the lossy case was truly representable were found.

The outcome of a six week stay at the Microfluidics Research Group headed by Bjørn T. Stokke, at the Norwegian University of Technology and Science (NTNU) is also presented, in the form of an automation software to be used for experiments to validate the numerical model. The software accommodates easy experiment control, automation and data acquisition, enabling high experimental resolution and good repeatability of experiments.

Resumé

I denne afhandling præsenteres nummeriske modeller til at simulere første ordens akustiske felter i en newtonsk væske, omkranset af et fast stof og en overflade i bevægelse. De nummeriske modeller bruges til at undersøge randbetingelser der ofte anvendes i mikrofluidiske simuleringer til at modellere tryk eller hastighedsfelters værdi langs rande mellem væsker og faststoffer. Randbetingelser er 1) Hård væg betingelsen som bruges til at modellere væske-faststof rande hvor det faste stof ikke giver sig for væsketrykket. 2) Væg med tab betingelsen, som bruges til at modellere væske-faststof rande der giver sig, baseret på forholdet mellem væskens og faststoffets akustiske impedans.

Ved at sammenligne de akustiske felter fundet vha. simuleringer der kopler lineær elasticitet og strømningsdynamik langs rande, med simuleringer der udelukkende bygger på strømningsdynamik og de førnævnte randbetingelser langs væskerande, kan randbetingelsernes validitet undersøges.

Validiteten viser sig at være afhængig af geometrien af væskens og faststoffets geometri og resonans i systemet. Hård væg betingelser er en rimelig approksimation når faststoffet er tykt og når systemet ikke påvirkes ved resonans. Væg med tab betingelsen viser sig generelt ikke at være en god approksimation, og ingen tilfælde hvori det modsatte gælder er fundet.

Yderligere præsenteres udbyttet af et seks uger langt ophold ved afdelingen 'NTNU Mikrofluidikk' ledet af Bjørn T. Stokke, ved Norges Teknisk-Naturvitenskapelige Universitet (NTNU), i form af et program til at automatisere forsøg, der skal bruges til at validere den nummerisk model. Programmet lader brugere styre og automatisere eksperimenter og dataopsamling, hvilket giver en god eksperiment-opløsning og repetérbarhed.

Preface

Preface

This thesis is submitted as partial fulfilment of the requirements for obtaining the degree, Master of Science in Engineering Design and Applied Mechanics at the Technical University of Denmark (DTU). The thesis was written at the department of Physics at the group of Theoretical Microfluidics (TMF), headed by Professor Henrik Bruus. The work carried out for the thesis was conducted from the 31. of August 2015 to March the 18. of March 2016 and corresponds to a workload of 35 ECTS points. From from the 26th of October to the 6th of December 2015, experimental work was carried out at the NTNU Microfluidics Group headed by Bjørn T. Stokke, at the Norwegian University of Science and Technology (NTNU).

The work carried out for the thesis is comprised of a theoretic and an experimental section. The theoretic work mainly consists of creating a numeric model with which the validity of commonly used boundary conditions is investigated. The experimental section is primarily focused on the process of developing a piece of software to ease experiments, with a view to experimentally verify the numeric model.

First and foremost I would like to thank Henrik Bruus, for his impressive dedication to all his students and his patience in teaching a mechanical engineer such as myself to better understand, and truly appreciate, physics. I would also like to thank the rest of the TMF group for perfectly exemplifying the open-door policy, particularly PhD students Jonas Karlsen and Mikkel Ley who have unfailingly been encouraging and willing to take a quick discussion on physics.

I also owe a great thanks to professor Bjørn T. Stokke of the Microfluidics Research Group at NTNU for letting me come work alongside his group. I would also like to thank the members of the group, particularly Jonas M. Ribe and Ole-Andreas Kavli for including me in their work and the rest of the group for including me socially from day one, and giving me an warmer welcome than I could have imagined.

<div align="center">

Nils Refstrup Skov
Department of Mechanics
Technical University of Denmark
March 18 2016

</div>

Contents

List of Figures

List of Tables

List of symbols

Symbol	Description	Unit
f	Frequency	Hz
$\omega = 2\pi f$	Angular frequency	s^{-1}
$i = \sqrt{-1}$	The imaginary unit	
e	Euler's number	
ρ	Mass density	kg m^{-3}
p	Pressure	Pa
$\boldsymbol{v}$	Velocity vector	m s^{-1}
c_0	Sound velocity of water	m s^{-1}
v	Velocity magnitude	m s^{-1}
$\boldsymbol{\sigma}_{\text{f}}$	Cauchy stress tensor	Pa
$\boldsymbol{\tau}$	Deviatoric stress tensor	Pa
$\boldsymbol{f}$	Body force density	N m^{-3}
$\boldsymbol{g}$	Gravity	N kg^{-1}
η	Dynamic shear viscosity	$\text{kg m}^{-1}\,\text{s}^{-1}$
ν	Kinematic shear viscosity	$\text{m}^2\,\text{s}^{-1}$
β	Ratio between shear and dilatational viscosities	
ϵ	Perturbation scale	
$\boldsymbol{v_1}$	First order velocity field	m s^{-1}
p_1	First order pressure field	Pa
ρ_1	First order mass desnity field	kg m^{-3}
$\boldsymbol{F}_{\text{drag}}$	Particle velocity relative to second order velocity field	m s^{-1}
$\tilde{\boldsymbol{v}}_2$	Particle velocity relative to second order velocity field	m s^{-1}

$\boldsymbol{u}_\mathrm{s}$	Solid displacement vector	m
$\boldsymbol{\sigma}_\mathrm{s}$	Solid stress tensor	$\mathrm{N\,m^{-2}}$
$c_\mathrm{T,s}$	Solid transverse speed of sound	$\mathrm{m\,s^{-1}}$
$c_\mathrm{L,s}$	Solid longitudinal speed of sound	$\mathrm{m\,s^{-1}}$
$\boldsymbol{\sigma}_\mathrm{pz}$	Piezoelectric stress tensor	$\mathrm{N\,m^{-2}}$
V	Electric potential	V
$\boldsymbol{\gamma}$	Strain tensor	$\mathrm{s^{-1}}$
$\mathbf{P}$	Piezoelectric coupling tensor	$\mathrm{C\,m^{-2}}$
$\boldsymbol{\Sigma}$	Piezoelectric stiffness matrix	Pa
$\boldsymbol{\epsilon}$	dielectric permittivity tensor	$\mathrm{F\,m^{-1}}$
u_0	Surface acoustic wave maximum displacement	m
a	Particle radius	m
δ_s	Viscous boundary layer	m
κ_0	Water compressibility	$\mathrm{Pa^{-1}}$
κ_p	Particle compressibility	$\mathrm{Pa^{-1}}$
ρ_0	Water mass density	$\mathrm{kg\,m^{-3}}$
ρ_p	Particle mass density	$\mathrm{kg\,m^{-3}}$
$\mathcal{L}$	Differential operator	
Ω	Computational domain	$\mathrm{m^2}$
$\partial\Omega$	Domain boundary	m
h	Mesh size	
λ	Wavelength	m
$\boldsymbol{n}$	Surface outward normal vector	
I	Identity matrix	
$\boldsymbol{\nabla}$	Gradient	$\mathrm{m^{-1}}$
$\boldsymbol{\nabla}\cdot$	Divergence	$\mathrm{m^{-1}}$
$|X|$	The absolute value of X	
$\langle X,,Y\rangle$	Inner product of X and Y	

Chapter 1

Introduction

Microfluidics is the study of fluid motion in sub-millimetre dimensions, usually realized in so-called microdevices. Due to small length scales and low velocities, inertia is largely negligible in microfluidics and viscous forces dominate the flow picture. Flows dominated by viscosity are laminar, making them highly predictable. The combination of microfluidics with acoustics is a field termed acoustofluidics. Particles in fluid suspension will undergo acoustophoresis in the presence of acoustic fields, as scattering of these give rise to an acoustic radiation force. The magnitude and direction of said force is dependent on the particle's mechanical properties; size, shape, compressibility and density [2, 6, 3]. Due to the specificity of the force acoustofluidics enable precise particle manipulation, particularly useful for biotechnological applications. Due to the small necessary sample volumes and form factor of microfluidic devices, acoustofluidics show a great promise to replace some of the current bulk processes in biotechnology, e.g. blood sample purification[4].

While acoustic fields can be introduced in a number of ways, this thesis will focus on acoustic fields in microdevices induced by *surface acoustic waves*. Specifically a numerical model and tools to experimentally verify said model will be introduced. The modelling will be a 2D representation of a microdevice, as shown in Fig. 1.1.

The following contains a short introduction to surface acoustic waves; how they are realized, how they create acoustic fields in microfluidic devices, the application of these fields in particle

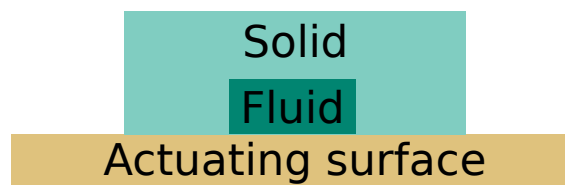Figure 1.1: Sketch of the modelled microdevice. The modelled device is a rectangular fluid domain, partially encased by a solid domains. Both domains are bounded downwards by a surface along which surface acoustic waves propagate. Kinetic energy is transferred from the surface wave to the fluid and solid domains, giving rise to acoustic fields dependent of surface acoustic wave frequency and amplitude.

migration and what approaches are used to numerically model such devices. This is followed by a brief introduction to the contents of each of the following chapters.

1.1   Introduction to surface acoustic waves

Surface acoustic waves - henceforth SAWs - are mechanical waves that primarily propagate along the surface of an elastic material. The waves are composed of a longitudinal compression motion coupled with a transversal shear motion. As SAWs are evanescent in the depth of the material, the energy is largely localized at the surface - unlike bulk acoustic waves, wherein the energy is distributed throughout the material. As they were initially described by Lord Rayleigh in 1885 [5], they are no new phenomenon and SAW-devices have a wide array of applications in electronics and measurement devices. However, it is only in recent years that SAWs have been introduced to the field of microfluidics, where they are used to manipulate fluids and suspended particles in a number of ways.

One way to realize SAWs is *via* piezoelectricity. Piezoelectricity is the coupling between an electrical charge and an applied mechanical stress, due to the asymmetric, crystalline structure of a material. Applying a stress to a piezoelectric material, e.g. quartz creates an electrical charge in the material *via* the direct piezoelectric effect. Vice versa applying a charge causes stress, due to the inverse or converse piezoelectric effect. The magnitude of the resulting charge or stress is dependent on the orientation of the crystalline structure of the material as described by a coupling tensor. While many materials exhibit piezoelectric behaviour, years of research have resulted in synthetic materials with coupling coefficient far surpassing naturally occurring materials.

Due to the very small relaxation time scale of the piezoelectric effect ($\approx 10\,\mathrm{ns}$), piezoelectricity is well suited for generating SAWs with frequencies up to the GHz scale. Interdigital transducers (IDTs) are etched onto a piezoelectric material as shown on Fig. 1.2. By applying an alternating voltage to the IDTs, the piezoelectric material will periodically contract and expand. The longitudinal movement between fingers will result in an transversal movement, i.e. a contraction between two fingers will cause an expansion in the direction pointing out of the IDT-plane. This combination of longitudinal and transverse motion is a surface acoustic wave, which will propagate away from the IDT along the surface of the substrate. Placing two IDTs parallel to each other will cause interference as two SAW waves propagating toward each other, causing a standing surface acoustic wave (SSAW) - see Figs. 1.3. For two SAWs with the same frequency, stationary displacement nodes and antinodes will form. At nodes, no displacements take place, while antinodes are the points at which the maximum displacement amplitude can be observed.

By having a SSAW in contact with a fluid, acoustic fields will form within the fluid. Fluid in contact with the excited substrate is set in motion, which spreads to the rest of the fluid, forming aforementioned fields. The features of these fields depend on a number of factors, such as channel geometry and material, as well as the character of the standing surface acoustic wave. The material surrounding the fluid is of importance as an encasing may reflect energy back in to the field. The harder the material, the more reflection and thus lower dissipation of energy out of the fluid.
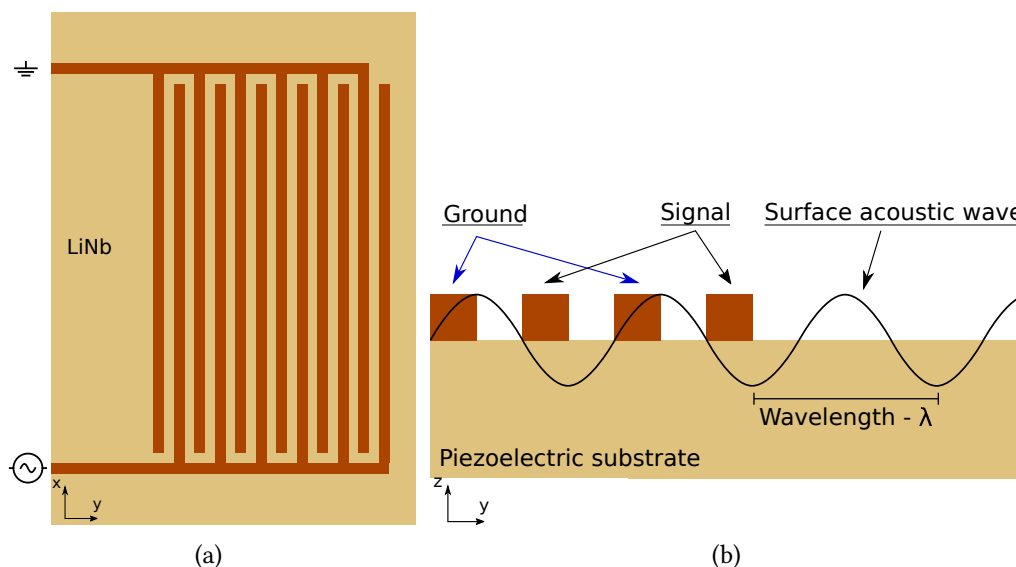
Figure 1.2: Interdigital transducer etched on to a piezoelectric medium. (a) Interdigital transducers are made by etching deposits of gold in fingerlike electrodes closely aligned without being in contact. (b) Applying a radiofrequency signal of a resonant frequency generates periodic contraction and elongation, causing a surface acoustic wave to form, which propagates beyond the interdigital transducer. The wavelength of the generated surface acoustic waves is four times the width of electrode fingers. Note that the drawing is stylized and not to scale.

The pressure and velocity fields appearing in the fluid are what occasion the possibility of particle manipulation. Due to scattering of the two fields, particles suspended in the fluid will experience a radiation force $F_{rad} \propto a^3$ [2, 3, 6], as described in section 2.6. This force will move particle towards equilibrium positions within the fluid, based on their mechanical properties.

By combining fields with specific retention times, suspended particles can in effect be sorted based on their size. For a polydisperse solution large particles will more quickly assume equilibrium positions. Limiting the time particles are affected by the fields will hence have the affect that particles below a given cut-off size will not have had time to move to equilibrium positions, in theory sorting above and below the cut-off point from each other. Due to the plethora of factors affecting a device functioning as the one described above, a complete numeric model is quite complex. Hence, the literature is abundant with applied simplifications. Examples include simple analytical expressions to describe particle movement [7, 8, 9], simplified expressions of the acoustic radiation force [10, 11, 12], analytical expressions to represent saw-actuation [1, 13, 12], replacing surrounding material with boundary conditions in simulations [1, 12], etc.

Although several influential factors exist, this thesis focuses primarily on the effect of the factors mentioned previously: channel geometry and material, and characteristics of the applied standing surface acoustic wave. This is primarily done by way simulation. A numerical model is created to obtain acoustic fields within a microchannel when a SSAW is applied, examining the
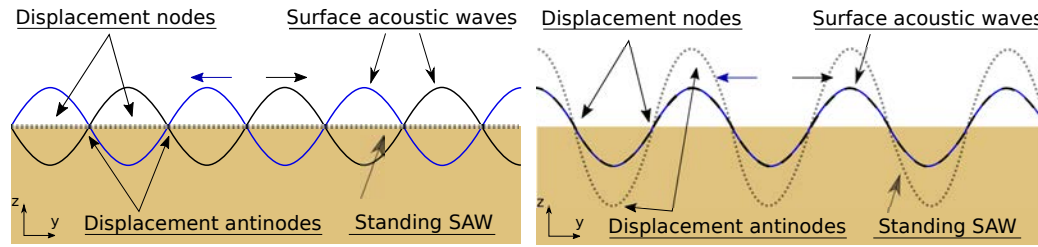
(a) At a given time, $t = t_0$ two harmonic waves will have complete destructive interference, canceling all displacement.

(b) At a later time, $t = t_0 + \phi$, the waves will be completely in phase for complete constructive interference, leading to maximum amplitude.

Figure 1.3: Standing surface acoustic wave resulting from interference. Two SAWs of equal amplitude propagating towards each other interfere, ranging from maximum destructive interference (a) to maximum constructive interference (b), causing a standing surface acoustic wave to form. At displacement nodes, no transversal movement is observed, while maximum amplitude is observed in displacement antinodes. While the movement of the substrate is more complex - consisting of longitudinal and transversal displacements - the principle is the same.

effect of boundary condition simplifications. Experiments performed were planned to be carried out, at the Norwegian University of Science and Technology NTNU Microfluidics Research Group headed by Bjørn T. Stokke, to verify the numeric model. To this end, a program was developed in LabVIEW to automate experiments. However, due to technical difficulties not related to the program, verification experiments have yet to be carried out.

1.2 Thesis contents

Chapter 2: Physics of microfluidic devices driven by surface acoustic waves

The governing equations of motion in a fluid, a solid and a piezoelectric substrate are outlined. Additionally, their coupling, possible simplifications of this, and some general material considerations are described.

Chapter 3: Numerical modelling

A 2D representation of a microfluidic device is introduced as the numerical model. An introduction to the finite element method and the weak formulation is given. The implementation of the governing equations and boundary conditions as weak formulations in COMSOL is explained. Mesh refinement studies of the fluid and of the solid are introduced to verify the model.

Chapter 4: Experimental Work

The experimental work done at NTNU is presented. The process from experiment design to final execution is presented. The chapter mainly serves as an introduction to the necessity of the software described in chapter 5, and as a description of the physical counterpart of the numeric model.

1.2.1 Chapter 5: Automation program

An piece of software developed to ease experimentation at the NTNU group is presented. The software is developed in the programming environment LabVIEW, which will briefly be presented. The work involved in creating the software is presented in the form of a product development process. The intended functionality of the software itself is discussed, while the technicalities of programming will be largely untouched.

Chapter 6: Numerical and experimental results and comparison

Based on simulations the commonly employed boundary condition 'hard wall' and the 'lossy wall' condition employed by Ref. [1] are discussed. This includes an analysis of the validity of the condition, based on geometries, materials, and SAW characteristics. Particle tracing is introduced, as a possible application of the numerical model. In addition some preliminary experimental results are presented.

Chapter 7: Conclusion and Outlook

Conclusions based on the numerical and experimental work are presented. Future improvements of both are discussed.

Chapter 2

Physics of microdevices driven by surface acoustic waves

This chapter describes the governing equations of the microfluidic device modelled in the thesis, and the coupling of said governing equations. The governing equations describe the physics of three domains as shown in figure 2.1; *(i)* a viscous fluid, *(ii)* a linearly elastic solid, and *(iii)* a piezoelectric material. The implementation of the governing equations in a numerical model will be discussed in Chapter 3. Additionally, acoustic scattering in the fluid domain and mechanical properties of the materials used are described.

In the following, all fields are considered from an Eulerian frame of reference, i.e. field values are evaluated at different times in fixed spatial coordinates **r**. Regarding time-dependence, all fields are considered to be harmonic with an angular frequency $\omega = 2\pi f$, where f is the actuation frequency of the SAW. For ease of reading, the spatial and temporal dependence of fields is henceforth implicit, e.g: $p = p(\boldsymbol{r}) \cdot e^{-\mathrm{i}\omega t}$.
Physical values of fields with a harmonic time-dependence are given as

$$p_{\text{physical}}(\boldsymbol{r}, t) = Re\left[p(\boldsymbol{r}) \cdot e^{-\mathrm{i}\omega t}\right]. \tag{2.1}$$

where $Re[\zeta] = \alpha$ denotes the real part of the complex number $\zeta = \alpha + \mathrm{i}\beta$.

Partial derivatives are denoted using the notation $\frac{\partial}{\partial x} = \partial_x$. As the fields are harmonic the time derivative is of course; $\partial_t = -\mathrm{i}\omega$.

2.1   Fluid Dynamics

The governing equations are the continuity equation - Eq. (2.2a) - and the Cauchy momentum equation equation - Eq. (2.2b) - which holds for any continuum. As a constitutive equation, a linear relation between pressure and density is assumed - Eq. (2.2e). The equations relate the scalar fields pressure p, and density ρ, with the vector field velocity $\boldsymbol{v}$. The temperature is assumed a constant 298 K throughout the fluid domain.

Solid - Ω_1

$$\rho\partial_t^2\mathbf{u}_s - \boldsymbol{\nabla}\cdot\boldsymbol{\sigma}_s \quad = \mathbf{0}$$

$$\partial_t\rho + \boldsymbol{\nabla}\cdot(\rho\mathbf{v}) = 0$$

Fluid - Ω_2

$$\rho\partial_t\mathbf{v} + \mathbf{v}\cdot\boldsymbol{\nabla}\mathbf{v} - \boldsymbol{\nabla}\cdot\boldsymbol{\sigma}_l \quad = \mathbf{0}$$

$$\rho\partial_t^2\mathbf{u}_{pz} + \boldsymbol{\nabla}\cdot\boldsymbol{\sigma}_{em} = \mathbf{0}$$

Piezoelectric

$$\boldsymbol{\nabla}\cdot\mathbf{d}_{em} = \mathbf{0}$$

substrate - Ω_3

Figure 2.1: Domains of interest. The governing equations of three domains dictate the physics of SAW-driven microdevices. The solid domain Ω_1, with field $\boldsymbol{u}_\mathrm{s}$ governed by Eq. (2.10). The fluid domain with fields p, ρ, and $\boldsymbol{v}$ governed by Eq. (2.2). The piezoelectric domain with fields $\boldsymbol{u}_\mathrm{pz}$ and $\boldsymbol{e}$, governed by Eq. (2.11)

$$\partial_t\rho = -\boldsymbol{\nabla}\cdot(\rho\boldsymbol{v}) \tag{2.2a}$$

$$\rho\partial_t\boldsymbol{v} + \boldsymbol{v}\cdot\boldsymbol{\nabla}\boldsymbol{v} = \boldsymbol{\nabla}\cdot\boldsymbol{\sigma} + \rho\boldsymbol{g} \tag{2.2b}$$

$$\boldsymbol{\sigma} = -p\boldsymbol{I} + \boldsymbol{\tau} \tag{2.2c}$$

$$\boldsymbol{\tau} = \eta\left(\boldsymbol{\nabla}\boldsymbol{v} + (\boldsymbol{\nabla}\boldsymbol{v})^T\right) + (\beta - 1)\,\eta\left(\boldsymbol{\nabla}\cdot\boldsymbol{v}\right)\boldsymbol{I} \tag{2.2d}$$

$$p = c_0^2\rho \tag{2.2e}$$

where η is the dynamic shear viscosity of the fluid, β is the ratio between the shear viscosity and the dilatational viscosity, $\boldsymbol{\sigma}$ is the Cauchy stress tensor, $\boldsymbol{\tau}$ is the deviatoric stress tensor - both of a Newtonian fluid, $\boldsymbol{g}$ is the body force density, and c_0 is the speed of sound of the fluid.

One may be tempted to assume that inertial effects can be neglected on grounds of small characteristic length scales and low velocities. While this is true for most microfluidic flows driven by pumps, the velocities induced by acoustics can easily be too high to ignore inertial effects. As section 2.6 will show, the non-linear term vanishes nonetheless in acoustics. For simplicity a single, uniform liquid is considered and no exterior fields are applied. Consequentially the only possible body forces are gravity and bouyance, which with good approximation cancel out. A non-uniform density distribution will appear as can be seen in section 2.6. However, due to the high actuation frequencies of the SAW, the time scale of these fluctuations is very small. This combined with the marginal changes in density, justifies the exclusion of gravitation forces on the liquid. Given these simplifications - and the time harmonic nature of the fields - Eq. (2.2b) simplifies to Eq. (2.3), similar to the unsteady or time-dependent Stokes flow, albeit with inertial

terms included

$$-\mathrm{i}\omega t\rho\boldsymbol{v} - \boldsymbol{\nabla}\cdot\boldsymbol{\sigma} = 0 \tag{2.3}$$

First order Acoustics

In order to linearize the governing equations perturbation theory is employed. Initially a quiescent liquid is considered, i.e. no flow, even pressure and density distribution.

$$\partial_\alpha \rho_0 = 0 \quad \partial_\alpha p_0 = 0 \quad \boldsymbol{v} = \boldsymbol{0} \quad \partial_\alpha \boldsymbol{v} = \boldsymbol{0} \tag{2.4}$$

where $\alpha = x, y, z, t$. If subjected to a small perturbation, the acoustic fields can mathematically be described as:

$$\rho = \rho_0 + \epsilon\rho_1 \quad p = p_0 + \epsilon p_1 \quad \boldsymbol{v} = \epsilon\boldsymbol{v}_1 \tag{2.5}$$

where $\epsilon = \rho_1/\rho_0$ is a scale of the smallness of the first order velocity field. A requirement for the validity of perturbation theory is that perturbations are small, e.g. $\epsilon \ll 1$. Reasonable values in microfluidics are $\approx 10^{-5} - 10^{-4} \ll 1$, leading to a good validity of the application of the theory in microfluidic acoustics. Inserting Eqs. (2.4) and (2.5) into Eqs. (2.2a) and (2.3) while utilizing Eq. (2.2e) yields:

$$\partial_t(\rho_0 + \epsilon\rho_1) = -\boldsymbol{\nabla}\cdot[(\rho_0 + \epsilon\rho_1)\epsilon\boldsymbol{v}_1] \tag{2.6a}$$

$$(\rho_0 + \epsilon\rho_1)\partial_t\epsilon\boldsymbol{v}_1 + \epsilon\boldsymbol{v}_1 \cdot \boldsymbol{\nabla}\epsilon\boldsymbol{v}_1 = \boldsymbol{\nabla}\cdot\boldsymbol{\sigma}_1 \tag{2.6b}$$

$$\boldsymbol{\sigma}_1 = -(p_0 + \epsilon p_1)\boldsymbol{I} + \boldsymbol{\tau}_1 \tag{2.6c}$$

$$\boldsymbol{\tau}_1 = \eta\left[\epsilon\boldsymbol{\nabla}\boldsymbol{v}_1 + (\epsilon\boldsymbol{\nabla}\boldsymbol{v}_1)^T\right] + (\beta - 1)\eta\left(\epsilon\boldsymbol{\nabla}\cdot\boldsymbol{v}_1\right)\boldsymbol{I} \tag{2.6d}$$

Collecting only terms of the first order, and dividing by ϵ yields:

$$\partial_t p_1 = -\rho_0 c_0^2 \boldsymbol{\nabla} \cdot \boldsymbol{v}_1 \tag{2.7a}$$

$$\rho_0\partial_t\boldsymbol{v}_1 = \boldsymbol{\nabla} \cdot \boldsymbol{\sigma}_1 \tag{2.7b}$$

With appropriate boundary conditions, the first order acoustic fields, $p_1, \rho_1, \boldsymbol{v}_1$ can be fully determined with Eq. (2.7). The applied boundary conditions depend the model, as discussed in sections 2.4 and 2.5.

Similarly perturbation theory can be used to calculate fields of increasing orders. In acoustics, second order fields are used when effects on a slower time scale must be taken into account. The second order flow is called streaming flow. Streaming flows generally have low velocities - and hence low Reynolds numbers - so drag induced on particles from them can be estimated as the Stokes drag

$$\boldsymbol{F}_{\text{drag}} = 6\pi\eta a\tilde{\boldsymbol{v}}_2, \tag{2.8}$$

where $\tilde{\boldsymbol{v}}_2$ is the particle velocity relative to the streaming flow velocity.

Second order fields are not in the scope of this thesis as they do not influence first order fields and consequently have no merit in discussing the validity of boundary conditions. Their existence does, however, limit the validity of the size of particles in the particle tracing method described in section 2.6.

2.2   Linear Elasticity

The equation of motion in linear elastics is derived from Cauchy's momentum equation. Instead of the viscous fluid stress tensor of Eq. (2.3), an isotropic solid stress tensor is defined. This tensor is defined based on strain using displacements rather than velocities, so the field of interest is $\boldsymbol{u}$. In an isotropic material, the stress tensor can be defined using any 2 of a number of constitutive constants, relating stress and strain states. The stress tensor used - Eq. (2.9b) - is based on the longitudinal $c_{L,s}$ and transverse $c_{T,s}$ speeds of sound of a solid.

$$\rho_s \partial_t{}^2 \boldsymbol{u}_{\mathrm{s}} = \boldsymbol{\nabla} \cdot \boldsymbol{\sigma}_{\mathrm{s}} + \rho \boldsymbol{g} \tag{2.9a}$$

$$\boldsymbol{\sigma}_{\mathrm{s}} = \rho \left[c_{\mathrm{T,s}}^2 (\boldsymbol{\nabla} \boldsymbol{u}_{\mathrm{s}} + \boldsymbol{\nabla} \boldsymbol{u}_{\mathrm{s}}^T) + (c_{\mathrm{L,s}}^2 - 2c_{\mathrm{T,s}}^2)(\boldsymbol{\nabla} \cdot \boldsymbol{u}_{\mathrm{s}})\boldsymbol{I} \right] \tag{2.9b}$$

The field $\boldsymbol{u}_{\mathrm{s}}$ has the same harmonic time-dependence as the acoustic fields of the fluid, and body forces are neglected in the solid, simplifying Eq. (2.9a) to Eq. (2.10),

$$-\rho_s \omega^2 \boldsymbol{u}_{\mathrm{s}} = \boldsymbol{\nabla} \cdot \boldsymbol{\sigma}_{\mathrm{s}} \tag{2.10}$$

As no non-linear terms appear in Eq. (2.10), the expression can be readily implemented in the numerical modelling when boundary conditions are implemented along all boundaries. It should be noted, that linear elasticity is only valid for small deformations, and a linear stress-strain relationship.

2.3   Piezoelectricity

The governing equations of the piezoelectric substrate are the linear stress-charge constitutive equations, adapted from [14]. The equations - Eqs. (2.11a) and (2.11b) are modified versions of the cauchy momentum equation and the constitutive relation between electric displacement and electric field, $\boldsymbol{d} = \epsilon e = \epsilon \boldsymbol{\nabla} \phi$. The modification is mediated by the third-order piezoelectric coupling tensor $\mathbf{P}$, which appears in both equations, adding a electrostatic potential term to the stress tensor and a strain term to the electric displacement.

$$\rho_{\mathrm{pz}} \partial_t^2 \boldsymbol{u}_{\mathrm{pz}} = \boldsymbol{\nabla} \cdot \boldsymbol{\sigma}_{\mathrm{pz}} \,, \tag{2.11a}$$

$$\boldsymbol{\nabla} \cdot \mathbf{d}_{\mathrm{pz}} = 0 \,, \tag{2.11b}$$

$$\boldsymbol{\sigma}_{\mathrm{pz}} = \boldsymbol{\Sigma} : \boldsymbol{\gamma} + \mathbf{P}^\dagger \boldsymbol{\nabla} \phi \,, \tag{2.11c}$$

$$\mathbf{d}_{\mathrm{pz}} = \mathbf{P} : \boldsymbol{\gamma} - \boldsymbol{\epsilon} \boldsymbol{\nabla} \phi \,, \tag{2.11d}$$

where Σ is the fourth-order stiffness tensor $P^\dagger$ is the hermitian of conjugate transpose of P, and colon ':' is the inner tensor product.

In this thesis, the piezoelectric substrate will not be modelled. Rather, the displacement along the surface of the substrate will be modelled as an analytical expression. While this may not accurately represent the motion of the substrate, it is implemented as the main focus is not on the piezoelectric effect, but rather the wall boundary conditions.

2.4 Coupling governing equations

The coupling between the three domains are shown in 2.2, using the subscripts s, f and pz as short-hand for solid, fluid and piezoelectric substrate. Note that in order to be fully determined boundary conditions must be applied at the outer boundaries of the solid and the substrate.

In effect, a coupling between two domains is imposed as two one-way boundary conditions, one acting from each domain toward the other. This means that 6 boundary conditions must be imposed to fully couple the three domains, as three domain-domain interfaces exist; fluid-solid, fluid-substrate, and solid-substrate. For each coupling described below, there are two possible sets of boundary conditions, as each coupling can go either way.
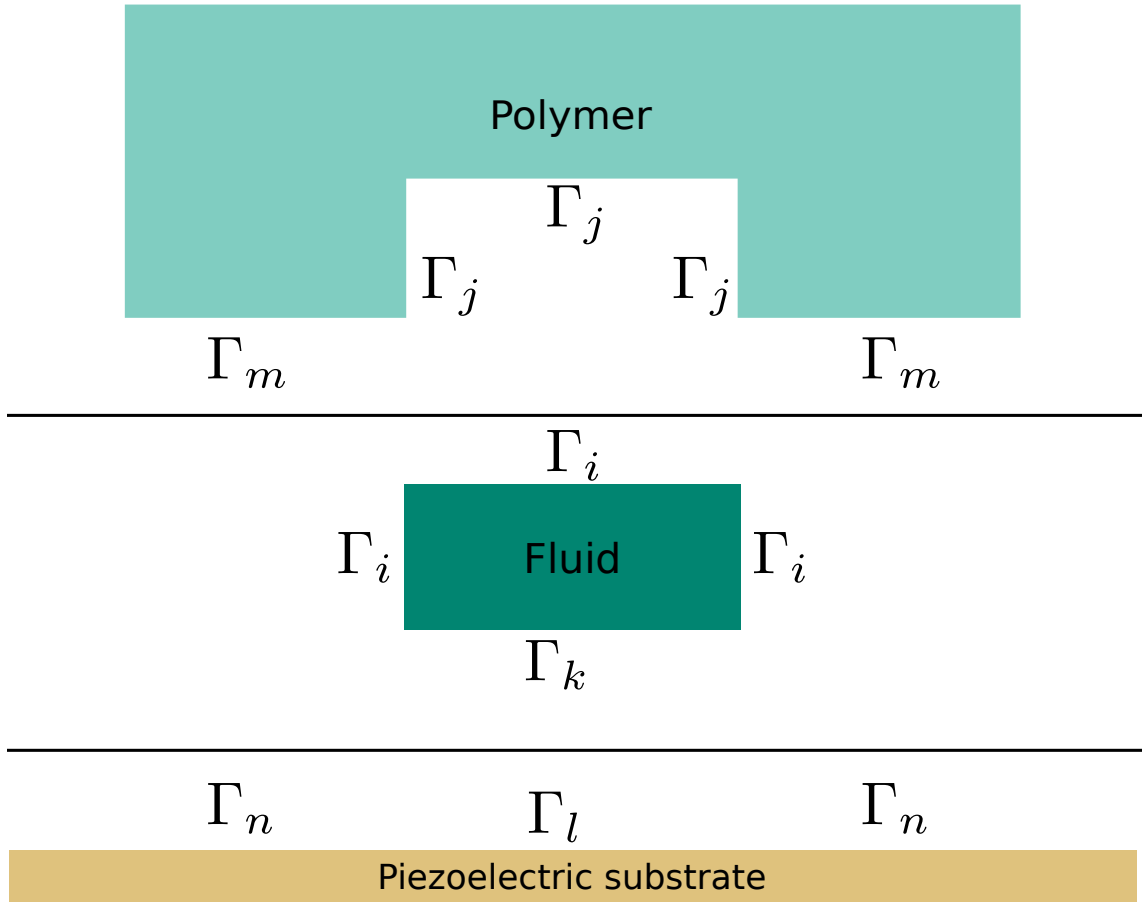

Figure 2.2: Illustration of the coupling between governing equations.
Γ_i couples the solid displacement with the fluid velocity; $\boldsymbol{v} = \partial_t \boldsymbol{u_s}$.
Γ_j couples the fluid pressure to the solid pressure; $\boldsymbol{n} \cdot \boldsymbol{\sigma}_f = \boldsymbol{n} \cdot \boldsymbol{\sigma}_s$
Γ_k couples the displacement of the piezoelectric substrate to the fluid velocity; $\boldsymbol{v} = \partial_t \boldsymbol{u}_{pz}$.
Γ_l couples the fluid pressure to the pressure of the piezoelectric substrate: $\boldsymbol{n} \cdot \boldsymbol{\sigma}_f = \boldsymbol{n} \cdot \boldsymbol{\sigma}_{p}z$
Γ_m couples the displacement of the piezoelectric substrate to solid ditto; $\boldsymbol{u}_s = \boldsymbol{u}_{pz}$.
Γ_n couples the solid pressure to the pressure of the piezoelectric substrate; $\boldsymbol{n} \cdot \boldsymbol{\sigma}_s = \boldsymbol{n} \cdot \boldsymbol{\sigma}_{p}z$.

Fluid-solid interface

Along the fluid-solid interface, a no-slip condition is imposed. This means that the velocity of
the fluid must match the velocity of the solid both tangentially and normally.
From the perspective of the solid, the coupling is implemented as a stress continuity across the
interface. The conditions are shown in Eq. (2.12).

$$\Gamma_i : \boldsymbol{v} \qquad = \partial_t \boldsymbol{u}_s = -i\omega \boldsymbol{u}_s \tag{2.12a}$$

$$,\Gamma_j : \boldsymbol{n}_s \cdot \boldsymbol{\sigma}_s = \boldsymbol{n}_s \cdot \boldsymbol{\sigma}_f \,. \tag{2.12b}$$

Fluid-substrate interface

The coupling of the fluid-piezo interface is the same as the fluid-solid interface. Eq. (2.13) show
the boundary conditions.

$$\Gamma_k : \boldsymbol{v} \qquad = \partial_t \boldsymbol{u}_{pz} = -i\omega \boldsymbol{u}_{pz} \tag{2.13a}$$

$$,\Gamma_l : \boldsymbol{n}_{pz} \cdot \boldsymbol{\sigma}_{pz} = \boldsymbol{n}_{pz} \cdot \boldsymbol{\sigma}_f \,. \tag{2.13b}$$

Solid-substrate interface

The coupling of the solid-piezo interface is very simple. As the solid is assumed to adhere per-
fectly to the substrate the displacements must be equal along the interface. Also stress must be
continuous along the interface. Eq. (2.14) show the boundary conditions.

$$\Gamma_m : \boldsymbol{u}_s \qquad = \boldsymbol{u}_{pz} \,, \tag{2.14a}$$

$$\Gamma_n : \boldsymbol{n}_{pz} \cdot \boldsymbol{\sigma}_{pz} = \boldsymbol{n}_{pz} \cdot \boldsymbol{\sigma}_s \,. \tag{2.14b}$$

2.5   Boundary conditions

Including the piezoelectric substrate and the solid surrounding the fluid in numerical models
can be computationally heavy - and give rise to numerical difficulties for some materials, as
mentioned in section 2.7. Hence, many numerical models in the literature solely model the fluid
domain and replace Γ_i and Γ_k in Fig. 2.2 with boundary conditions, to emulate the interactions.
For Γ_i one of three boundary conditions - depending on the interfacing material - are usually
applied; soft wall, hard wall, lossy wall, as shown in Eqs. (2.15c), (2.16b) and (2.17e) [15].

Soft Wall

The soft wall condition is used to model fluid-air interfaces, and interfaces between fluids and
encasings of negligible width. Along such an interface, the acoustic pressure of the fluid must
match the pressure of the surroundings;

$$p = p_0 + p_1 = p_{atm} \tag{2.15a}$$

.

For the unperturbed liquid considered in perturbation theory, this condition is fulfilled:

$$p_0 = p_{atm} \,. \tag{2.15b}$$

Combining the two expressions, the soft wall condition - Eq. (2.15c) - appears:

$$p_1 = 0 \,. \tag{2.15c}$$

Hard Wall

The hard wall condition is used to model indeformable interfaces, i.e. interfaces with an infinitely hard material. If no deformation takes place, and no flow through the interface is permitted, the normal velocity of the liquid at the wall must be 0. For inviscid liquids, an expression for the velocity as a function of the pressure gradient can be derived from Eq. (2.7b):

$$\boldsymbol{v}_1 = \frac{-i}{\rho_0 \omega} \boldsymbol{\nabla} p_1 \,. \tag{2.16a}$$

This yields two possible formulations of the hard wall condition; a velocity, and a pressure formulation, both shown in Eq. (2.16b)

$$\boldsymbol{n} \cdot \boldsymbol{v}_1 = 0 \quad \text{or} \quad \boldsymbol{n} \cdot \boldsymbol{\nabla} p_1 = 0 \,. \tag{2.16b}$$

Lossy Wall

The lossy wall was used by Ref. [1] to approximate fluid-solid interfaces through which some radiative losses occur. Along the interface two conditions must hold: the normal velocity and the pressure across the interface must be continuous.

$$\boldsymbol{n} \cdot \boldsymbol{v}_1 = \boldsymbol{n} \cdot \boldsymbol{v}_s \quad , \quad p_1 = p_s \,, \tag{2.17a}$$

where the index s, denotes solid. From Eq. (2.16a), it can be seen that for inviscid liquids the velocity can be described as the gradient of a potential ϕ_1:

$$\boldsymbol{v}_1 = \boldsymbol{\nabla} \phi_1, \quad \phi_1 = \frac{-i}{\rho_0 \omega} p_1 \,. \tag{2.17b}$$

By defining the radiative losses for a planar wave as a potential with purely right-ward propagation, $\phi_m = A e^{ik_m x}(e^{-i\omega t})$, the velocity and the pressure of the wall give the following expressions for the potential at the wall.

$$v_m = \boldsymbol{\nabla} \phi_s = ik_s \phi_s \qquad \phi_s = -i\frac{c_s}{\omega} v_s \,, \tag{2.17c}$$

$$\phi_s = \frac{-i}{\rho_s \omega} p_s \,. \tag{2.17d}$$

Combining above expression with Eq. (2.17a) yields the velocity lossy wall condition, which also can be expressed as a pressure lossy wall condition:

$$\boldsymbol{n} \cdot \boldsymbol{v}_1 = \frac{1}{\rho_s c_s} p_1 \quad \text{or} \quad \boldsymbol{n} \cdot \boldsymbol{\nabla} p_1 = \frac{i\rho_0 \omega}{c_s \rho_s} p_1 \,. \tag{2.17e}$$

Notice, that the hard and lossy wall conditions can be imposed as a Dirichlet condition on the velocity, or a Neumann condition on the pressure. The distinction between Dirichlet and Neumann boundary conditions is of importance as described in the section 3.2. In either case, a second condition is necessary in the tangential direction. Here, a no slip condition is employed regardless of the wall:

$$\boldsymbol{t} \cdot \boldsymbol{v}_1 = 0 \,, \tag{2.18}$$

where $\boldsymbol{t} = \hat{\boldsymbol{n}}$ is the tangential unit vector of the surface.

Piezoelectric substrate

The surface acoustic waves are usually not simulated, but rather implemented as an analytical expression. In this thesis the expression used in Refs. [1, 13] is implemented as prescribed displacements in y and z directions along the substrate surface:

$$u_{y,pz} = 0.6 u_0 e^{-C_d y} \left[sin \left(\frac{-2\pi(y - w/2)}{\lambda} + \omega t - \Delta\phi \right) + sin \left(\frac{-2\pi(w/2 - y)}{\lambda} + \omega t \right) \right], \tag{2.19a}$$

$$u_{z,pz} = -u_0 e^{-C_d y} \left[cos \left(\frac{-2\pi(y - w/2)}{\lambda} + \omega t - \Delta\phi \right) + cos \left(\frac{-2\pi(w/2 - y)}{\lambda} + \omega t \right) \right], \tag{2.19b}$$

where u_0 is the max z-displacement of the substrate, w is the width of the fluid-domain, λ is the wavelength of the SAW, and $\Delta\phi$ is a phase angle between the SAWs.
The expression does not take into account the displacement decay of the SAW that occurs along the solid-PDMS interface. The argument for employing the lossy wall condition in Ref. [1] is a PDMS layer width > 2mm, which in turn leads to a higher decay of the SAW displacements in the channel itself, compromising the validity of the analytical expression in the supposedly valid region of the lossy wall condition. The actuation is thus not necessarily representative of a piezoelectric SAW, but will be used for comparison purposes.

2.6   Acoustic scattering

When neglecting temperature, the first order acoustic fields in the fluid are comprised of 3 complex, linearly independent fields p, v_y, v_z. This complicates qualitative comparison between various boundary conditions, as all three fields must be compared, as well as their phase differences. By rather relating how the combined effect of the fields would affect particles suspended in the fluid, a more straightforward comparison can be made. This can be done by calculating the acoustic radiation force $\boldsymbol{F}_{rad}$, which arises from scattering of acoustic fields of particles[2, 3, 6]. The

acoustic radiation force on a thermoelastic particle derived in [3] in the limit of small boundary layers $\delta_t, \delta_s \ll a$ will be used here. Thermal effects are neglected in this thesis though, simplifying the dipole coeffiecient to the expression in the limit $\delta_t/a = 0$. Only the bare minimum parts of the theory will be recapitulated here, as the derivations of the expressions is beyond the scope of this thesis. Refer to [3] for derivations.

The force exerted on particles suspended in a fluid is the surface integral of the fluid stress tensor.

$$\boldsymbol{F}_{rad} = \left\langle \oint_{\delta\omega} \boldsymbol{n} \cdot \boldsymbol{\sigma} \, d\mathrm{A} \right\rangle$$

where $\langle X \rangle$ is the time-averaged value of X.

From this the following expression of the force - as a function of the acoustic first order fields and particle properties - can be derived:

$$\boldsymbol{F}_{rad} = -\pi a^3 \left[\frac{2\kappa_0}{3} Re \left[f_0^* p_1^* \boldsymbol{\nabla} p_1 \right] - \rho_0 Re \left[f_1^* v_1^* \cdot \boldsymbol{\nabla} v_1 \right] \right], \tag{2.20}$$

where the monopole f_0 and dipole f_1 coefficients relate the compressibility and density of particles and fluid respectively, and x^* indicates the conjugate of x, as shown in Eq. (2.21) & Eq. (2.22).

$$f_0 = 1 - \tilde{\kappa}, \tag{2.21}$$

$$\tilde{\kappa} = \frac{\kappa_p}{\kappa_0},$$

$$f_1 = \frac{2(\tilde{\rho} - 1)}{2\tilde{\rho} + 1} \left[1 + 3(1 + i)\frac{\tilde{\rho} - 1}{2\tilde{\rho} + 1} \frac{\delta_s}{a} \right], \tag{2.22}$$

$$\tilde{\rho} = \frac{\rho_p}{\rho_0},$$

where κ_p and κ_0 are the compressibilities of particle and fluid respectively, ρ_p ρ_0 are the ditto densities, and

$$\delta_s = \sqrt{\frac{2\eta_0}{\rho_0 \omega}}, \tag{2.23}$$

is the viscous boundary layer of the fluid. Water at 298 K, excited with an angular frequency of 6.65 MHz scale has a viscous boundary layer of $\approx 0.21 \, \mu m$.

The expression for force in Eq. (2.20) is comprised of two terms: a relative compressibility term and a relative density-viscosity term. The former relates to the gradient of the pressure while the latter relates to the gradient of the magnitude of the velocity field.

It is important to note that the magnitude and sign of these terms depend heavily on the material parameters of the suspended particles compared to those of the suspension fluid. Considering the monopole term, three scenarios can be imagined; particles with (*i*) lower, (*ii*) equal or (*iii*) higher compressibility than the suspension fluid.

$$\begin{array}{llll} (i) & \kappa_p < \kappa_0 & \tilde{\kappa} < 1 & f_0 > 0, \\ (ii) & \kappa_p = \kappa_0 & \tilde{\kappa} = 1 & f_0 = 0, \\ (iii) & \kappa_p > \kappa_0 & \tilde{\kappa} > 1 & f_0 < 0. \end{array}$$

For these cases monopole scattering give a tendency of particle migration (*i*) towards, (*ii*) unaffected by, and (*iii*) away from so-called pressure nodes, i.e. areas of low fluctuations in pressure. The second term depends on the size ratio between the viscous boundary layer and the particle diameter, as well as the relative densities. Unlike the monopole coefficient, f_1 will take on complex values for all cases, except $\tilde{\rho} = 1$, $f_1 = 0$. For this value, the particle migration will be independent of velocity magnitudes, and depend solely on monopole scattering.

As the acoustic radiation force is a superposition of the two mentioned terms, the acoustic radiation force is always particle-relative. Thus, particles of similar size, but differing density and compressibility may show radically different behavior, in the same acoustic fields.

2.7   Material properties

Prior to implementing the governing equations in a numerical model, some reflections on the physics and materials involved are in order, to ensure the model is not used inappropriately. The following are some points, which should be kept in mind, when applying the numerical model.

Polydimethylsiloxane

Incompressibility:
Polidimethylsiloxane (PDMS) is a polymer commonly used in microfluidic device prototypes as it is cheap and easy to mass fabricate once a master mold has been made. While it has some clear advantages experimentally, it introduces some complexities numerically which are described below. As mentioned in section 2.2, the stress tensor can be described using other constitutive relations, than the speeds of sound. One formulation is based on the Young's modulus and Poisson's ratio.

$$\boldsymbol{\sigma}_{\mathrm{s}} = \left[\frac{1}{2}(\boldsymbol{\nabla}\boldsymbol{u}_{\mathrm{s}} + \boldsymbol{\nabla}\boldsymbol{u}_{\mathrm{s}}^{T}) + \frac{\sigma}{1 - 2\cdot\sigma}(\boldsymbol{\nabla}\cdot\boldsymbol{u}_{\mathrm{s}})\boldsymbol{I} \right] \frac{E}{1 + \sigma}, \qquad (2.24)$$

where σ is the Poisson's ratio, and E is the Young's modulus.

For PDMS, Poisson's ratio varies from $\sigma \approx 0.5 - 0.41$ depending on the mixing ratio and curing temperature [16, 17]. Combining this with Eq. (2.24) clearly introduces numerical difficulties, as the divergence term of the stress tensor equals infinity for $\sigma = 0.5$. Physically, $\sigma = 0.5$ means the solid is incompressible; $\boldsymbol{\nabla}\cdot\boldsymbol{u} = 0$, and as such would negate the infinite fraction. Numerically, this will not necessary hold though, so as a precaution the modelled PDMS has a Poisson's ratio of ≈ 0.41 to ease simulations and give a wide berth to regions where the divergence term may approach infinity.

Acoustothermal heating:
Another unfortunate trait of PDMS is its degree of internal damping at high frequencies. This causes a large part of the kinetic energy to be converted to thermal energy.[18] At peak frequencies (approx. $28\,\mathrm{MHz}$ to $32\,\mathrm{MHz}$) this invalidates the model if thermal effects and damping is not included. While acoustothermal heating also occurs at the lower frequencies, it is to a lower extent and will be neglected from the numeric model.

Piezoelectric substrates

Unlike isotropic solids encasing the fluid, the asymmetric crystalline structure of piezoelectric materials make them directionally aligned. For surface acoustic waves, this means the SAW velocity depends on the propagation direction relative to the crystal structure. Thus, when referring to the piezoelectric substrate used, the orientation should always be mentioned as well. In manufacture, the crystalline orientation relative to the IDTs is of utmost importance, as IDT designs must be based around the SAW velocity, as described in section 4.1. The piezoelectric substrate used throughout this thesis will be lithium niobate 128 ° XY-cut.

Chapter 3

Numerical modelling in COMSOL

This chapter will cover the generation of a numerical model, based on the governing equations, couplings, and boundary conditions introduced in the previous chapter. The model can be used to relate the results found using boundary conditions to those found when modelling interactions. This will be done by comparing results of a model containing only a fluid domain Ω_2 with boundary conditions - the simple model - to the results of a model containing the fluid and the solid domain Ω_1 and Ω_2 and their interactions - henceforth the full model.

The model is generated in COMSOL Multiphysics, a commercial simulation software which accomodates implementation of *weak formulations* of equations using the *finite element method* (FEM).

3.1   Device used as model basis

The numerical modelling represents a stop flow situation, $v_x = 0$, on the microdevice outlined in figure 3.1. The design and material parameters are adapted from Ref. [1], to compare results from this to the simple model, before in turn comparing these to results of the full model. As described in Chapter 2 three domains are taken into consideration in the modelling. The modelling is performed two-dimensionally in the y,z-plane, shown in 3.1b. In the active area, i.e. along the length of the electrodes, L, the field values are considered to solely depend spatially on y and z, with a harmonic time dependence

$$\partial_x s = 0 \, , \; s(\boldsymbol{r}, t) = s(y, z)e^{-\mathrm{i}\omega t} \, , \tag{3.1}$$

where s is any field value, $p_1, \rho_1, \boldsymbol{v}_1, \boldsymbol{u}_\mathrm{s}$.

The models estimate the physical situation anywhere along the active area - shown in the box with dashed lines in Fig. 3.1a.

3.2   Weak formulation

Prior to explaining the generation of the numeric model, an introduction to the finite element method and the weak formulation is appropriate. FEM is a method to solve field problems, by discretizing the computation domain into a finite number of elements. This mesh makes the

(a)
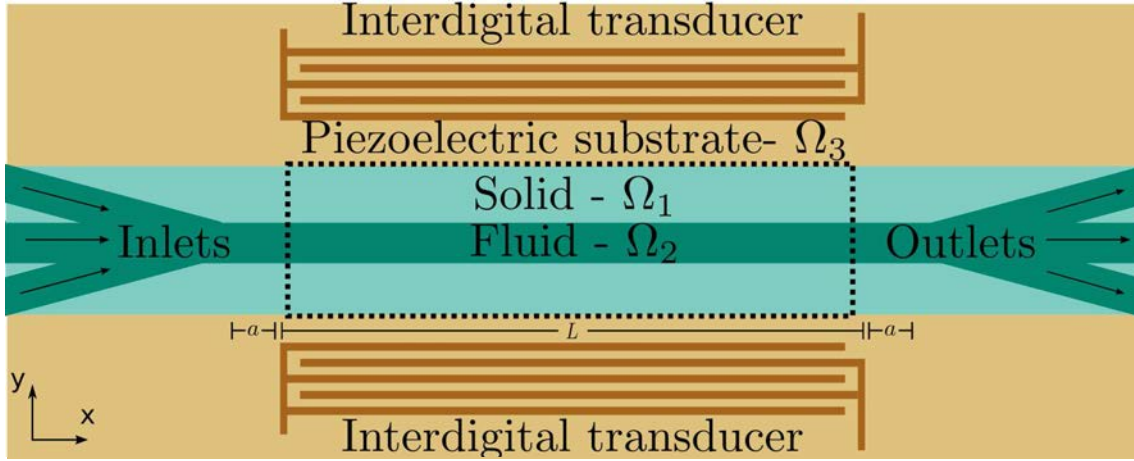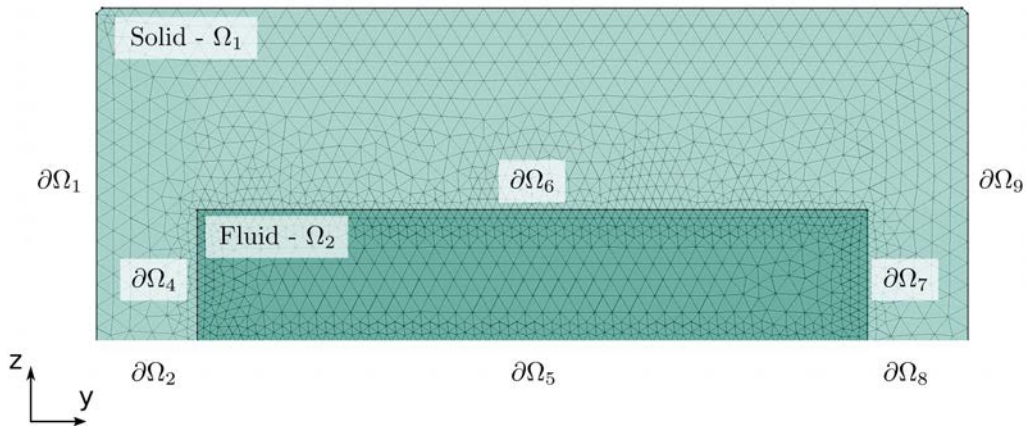
(b)

Figure 3.1: Sketch of the device being modelled. (a) Outline of the modelled chip as viewed from above. Due to the parallelism of the IDTs and the microchannel, SAWs propagate orthogonal to flow direction, leading to a SSAW with no *x*-dependence along the active area, i.e. the length of the IDTs *L*. Fringe effects may occur some distance *a* from the ends of the IDTs, as SAWs here will not exclusively propagate orthogonal to the flow. The numerical model is valid within the dashed box. (b) Two-dimensional finite element representation of the microfluidic device, consisting of two domains and 9 boundaries. Domain Ω_1 is a solid microchannel, with displacement field $\mathbf{u}_s$, and domain Ω_2; is a fluid with acoustic fields p_1, ρ_1 and $\boldsymbol{v}_1$. Two numeric models are set up. One containing Ω_1 and Ω_2 and their interactions, and one containing Ω_2 where interactions are modelled as boundary conditions.

Table 3.1: Domain dimensions and actuation parameters used in the numeric model. From Ref.
[1]

	Solid Domain Ω_1	Fluid Domain Ω_2	Actuation parameters	
Width	750 µm	600 µm	Frequency	6.5 MHz
Height	300 µm	125 µm	Wavelength	600 µm

basis of the weak formulation. The weak form of governing equations need not be met at every
material point as the strong form does, but may instead only be met in an integral sense near
each mesh node. In fact, the weak form and the strong form are identical in the limit of infinite
mesh elements. The weak formulation is found by rewriting a partial differential equation (PDE)
to a sum of integrals - one for each element of the grid. The following theory is based on [19]

Consider a general, linear differential operator for the field $g(\boldsymbol{r})$:

$$\mathcal{L}\{g(\boldsymbol{r})\} = F(\boldsymbol{r}),$$ (3.2)

where $F(\boldsymbol{r})$ is a source term. The defect is defined as

$$d(\boldsymbol{r}) \equiv \mathcal{L}\{g(\boldsymbol{r})\} - F(\boldsymbol{r}),$$ (3.3)

which for the strong solution is zero. In order to obtain a number of integral equations, the field
$g(\boldsymbol{r})$ is approximated as a linear combination of basis functions $\hat{g}_n$, multiplied with a correspond-
ing field coefficient c_m

$$g(\boldsymbol{r}) \approx \sum_n c_m \hat{g}_n.$$ (3.4)

Basis functions $\hat{g}_i$ vary between 0 and 1 at around their corresponding mesh node i, while the
field coefficient c_i is the field value at the position of node i.
As an approximation to the strong solution - in which Eq. (3.2) holds for every material point
- the projection of the defect on the basis function can be limited to be zero within each mesh
element, by demanding the inner product of each basis function and the defect be zero.

$$\langle \hat{g}_m, d(\boldsymbol{r}) \rangle = 0 \,\forall\, m,$$ (3.5)

where the inner produt of two functions is defined as $\langle a(\boldsymbol{r}), b(\boldsymbol{r}) \rangle \equiv \int_\Omega a(\boldsymbol{r})b(\boldsymbol{r})\mathrm{d}V$. Inserting
the defect - Eq. (3.3) - expressed *via* basis functions - Eq. (3.4) - into Eq. (3.5) yields

$$\sum_n c_n \langle \hat{g}_m, \mathcal{L}\{\hat{g}_n\} \rangle - \langle \hat{g}_m, F \rangle = 0 \quad \forall\, m$$ (3.6)

where it is assumed that $\mathcal{L}$ is linear, allowing $\mathcal{L}\{\sum_n c_n \hat{g}_n\} = \sum_n \mathcal{L}\{c_n \hat{g}_n\}$
Eq. (3.6) can be reconized as a matrix equation

$$\mathbf{K}\boldsymbol{c} - \boldsymbol{f} = \mathbf{0},$$ (3.7)

where $K_{mn} = \langle \hat{g}_m, \mathcal{L}\{\hat{g}_n\} \rangle$, vector $\boldsymbol{c}$ contains the field coefficients, and $\boldsymbol{f} = \langle \hat{g}_m, F \rangle$. By
solving Eq. (3.7) for $\boldsymbol{c}$ the weak solution is found.

3.2.1   Boundary conditions.

In order to obtain an expression that includes boundary conditions, it is assumed that the differential operation can be rewritten to continuity form - Eq. (3.8) - which holds true for the governing equations of this thesis.

$$\boldsymbol{\nabla}\cdot\boldsymbol{\Gamma} - \boldsymbol{F} = \boldsymbol{0}. \tag{3.8}$$

Inserting the divergence form Eq. (3.8) in the defect requirement Eq. (3.5), yields

$$\int_{\Omega} \hat{g}_n \boldsymbol{\nabla}\cdot\boldsymbol{\Gamma} - \hat{g}_n \boldsymbol{F}\, \mathrm{d}V = \boldsymbol{0}. \tag{3.9}$$

Using the vector calculus identity $\boldsymbol{\nabla}\cdot(\hat{g}_n\boldsymbol{\Gamma}) = \boldsymbol{\Gamma}\cdot\boldsymbol{\nabla}\hat{g}_n + \hat{g}_n\boldsymbol{\nabla}\cdot\boldsymbol{\Gamma}$ and Gauss' theorem, Eq. (3.9) can be rewritten from a volume integral to the sum of a surface integral and a volume integral.

$$\oint_{\partial\Omega} \hat{g}_n \boldsymbol{n}\cdot\boldsymbol{\Gamma}\, \mathrm{d}A + \int_{\Omega} -\boldsymbol{\Gamma}\cdot\boldsymbol{\nabla}\hat{g}_n - \hat{g}_n\boldsymbol{F}\, \mathrm{d}V = \boldsymbol{0}. \tag{3.10}$$

The derivative is thus moved from the continuity tensor to the test function, which is analytically known.

Applying *Neumann* boundary conditions in the weak formulation is very straightforward. If the flux of $\boldsymbol{\Gamma}$ on a surface $\partial\Omega_i$ is a known function $h(\boldsymbol{r})$ it is merely a matter of inserting the value in the surface integral, ie.

$$\boldsymbol{n}\cdot\boldsymbol{\Gamma} = \boldsymbol{h}(\boldsymbol{r}) \quad \text{for} \quad \boldsymbol{r}\in\partial\Omega_i. \tag{3.11}$$

Implementing *Dirichlet* conditions is slightly more difficult. If the value of $g(\boldsymbol{r})$ along a boundary is know to be $j(\boldsymbol{r})$, the Dirichlet condition is implemented as a constraint on the function;

$$R\left[g(\boldsymbol{r})\right] = g(\boldsymbol{r}) - j(\boldsymbol{r}) = 0, \tag{3.12}$$

along a boundary. The constraint is realized by adding a Lagrange multiplier $\lambda(\boldsymbol{r})$, which only exist on the domain boundary $\partial\Omega_i$. Analogous with the field value, the Lagrange multiplier can be defined by a set of basis functions $\hat{\lambda}_m$ and constraint coefficients b_m

$$\lambda(\boldsymbol{r}) \approx \sum_m b_m\hat{\lambda}_m. \tag{3.13}$$

By demanding the the inner product of the Lagrange multiplier and the constraint be zero, the weak form of the Dirichlet condition can be enforced

$$\left\langle \hat{\lambda}_m, R \right\rangle = 0 \quad \forall\, m. \tag{3.14}$$

The Lagrange multiplier only assumes values along the boundary, and the constraint can therefore be inserted in the continuity equation Eq. (3.8);

$$\boldsymbol{\nabla}\cdot\boldsymbol{\Gamma} - \boldsymbol{F} - \sum_n \lambda(\boldsymbol{r}) = \boldsymbol{0}. \tag{3.15}$$

In COMSOL, the Dirichlet conditions can be imposed by merely prescribing function values along boundaries, while COMSOL handles the Lagrange multiplier and the constraint.

3.3 Modelling steps

The steps involved in creating the numeric model are outlined below, with an emphasis on inputting the weak formulation in the model.

3.3.1 Definitions

Parameters, variables and analytic expressions to be used in the modelling are defined. Listing 3.1 shows examples of definitions made at the start of the file.

```
wWa = 600 [um]
fY = rho*dt^2*uy1
dt = −i*omega
divu1 = uy1y+uz1z
```

Listing 3.1: COMSOL definitions include any value, or mathematical expression, that may be reused throughout the model

3.3.2 Computational domains

The simple two-dimensional geometry shown in Fig 3.1b is drawn. It consists of two rectangles to represent the solid and fluid domains Ω_1 and Ω_2. In simulations, the geometries and material parameters of both domains are varied to observe how the system response depends on surrounding conditions.

3.3.3 Physics interfaces

Each domain is assigned one or more 'physics interfaces'. These interfaces are sets of bulk equations, initial values and boundary conditions that collectively describe the behaviour of one or more dependent variables within a domain. In the model a physics interface is included for the solid displacement $\boldsymbol{u}_{\mathrm{s}}$, and one for the fluid velocity $\boldsymbol{u}$ and pressure p each. The interfaces are where the weak form governing equations are introduced to the model. The physics interface for the solid domain is detailed below:

In COMSOL, basis functions - called test functions within COMSOL - of dependent variables are automatically generated. Spatial derivatives of dependent variables and their basis functions are also generated. The notation used in COMSOL is shown in table 3.2.

Table 3.2: COMSOL notation

	Math notation	COMSOL notation
Field variable	ϕ	`phi`
Basis/test function of the field variable	$\hat{\phi}_m$	`test(phi)`
Spatial derivative of field variable	$\partial_x \phi$	`phix`
Spatial derivative of field variable's test function	$\partial_x \hat{\phi}_m$	`test(phix)`

The governing equation in the solid domain - Eq. (2.7b) - expressed in divergence form take the on appearance

$$\boldsymbol{\nabla} \cdot \boldsymbol{\sigma}_\mathrm{s} + \rho_\mathrm{s} \omega^2 \boldsymbol{u}_\mathrm{s} = \boldsymbol{0} \tag{3.16}$$

Inserting this continuity equation into Eq. (3.10) yields

$$\underbrace{\oint_{\partial \Omega} \hat{u}_m \boldsymbol{n} \cdot \boldsymbol{\sigma}_\mathrm{s} \, \mathrm{d}A}_{\text{Neumann BC, List. 3.3}} + \underbrace{\int_{\Omega} -\boldsymbol{\sigma}_\mathrm{s} \cdot \boldsymbol{\nabla} \hat{u}_m + \hat{u}_m \rho_\mathrm{s} \omega^2 \boldsymbol{u}_\mathrm{s} \, \mathrm{d}V}_{\text{Bulk equation, List. 3.2}} \quad \underbrace{= \boldsymbol{0}}_{\text{Implicit in COMSOL}} \tag{3.17}$$

In COMSOL, the surface and volume integrals are implemented separately, and it is implicit that the sum of integrals is equal to zero. Furthermore, only one dimension is handled in each command. The volume integral in Eq. (3.17) is inserted in the physics interface as a 'Weak Form PDE', by entering the first line shown in Listing 3.2

```
−sigmaYY*test(uy1y) − sigmaYZ*test(uy1z) − test(uy1)*fY
```

Listing 3.2: Solid bulk equations in the y-direction, valid for Ω_1 in Fig. 3.1b.

where $sigmaYY$ and $sigmaYZ$ are components of the solid stress tensor, and fY is the rate of change of momentum in the solid.

As a default, COMSOL sets the initial values of dependent variables and the flux along boundaries to be zero. On boundaries where this is not desired, it can be overridden by setting any specific value. Along the fluid-solid boundary $\partial \Omega_4$, $\partial \Omega_6$ & $\partial \Omega_7$, the stres continuity described in Section 2.4 couples the solid to the fluid,

$$\boldsymbol{n}_\mathrm{s} \cdot \boldsymbol{\sigma}_\mathrm{s} = \boldsymbol{n}_\mathrm{s} \cdot \boldsymbol{\sigma}_\mathrm{f} \tag{2.12b}$$

This condition is enforced by inserting it in Eq. (3.17), effectively adding the pressure from the fluid as a flux to the displacement. In COMSOL, this is implemented by adding a 'Weak Contribution' to the physics interface, and marking relevant boundaries. The input text is shown in Listing 3.3.

```
test(uy1)*(ny*ss1YY+nz*ss1YZ)+test(uz1)*(ny*ss1ZY+nz*ss1ZZ)
```

Listing 3.3: One-way coupling from liquid to solid, implemented as a stress flux term in Eq. (3.17).

where $ss1YY$, $ss1YZ$, $ss1ZY$ & $ss1ZZ$ are components of the fluid stress tensor.

Along the solid-piezo interface $\partial \Omega_2$ and $\partial \Omega_8$, the displacement of the solid is fixed to follow an prescribed analytic expression - Eq. (2.19). The numerics of implementing the Lagrange multiplier used for this is handled by COMSOL, and the only necessary input is the value to impose on the boundary.

On the remaining boundaries $\partial \Omega_1$, $\partial \Omega_3$ and $\partial \Omega_9$, the default no flux condition holds. This corresponds to an assumption of no pressure on the boundaries, which although not entirely correct is a reasonable approximation.

A similar approach is taken to set up the fluid velocity and pressure physics interfaces. Interfaces allow multiple conflicting boundary conditions to be defined, as long as the conflicts are resolved prior to solving the system. This allows the simple model and the full model to be defined in the same COMSOL file. It is thus only the configuration set in the solver, that determines whether or not the system solved for is the simple or full model.

3.3.4 Meshing

After setting up the physics interfaces, the domains are meshed. Triangular grids are used in both the solid and the fluid domains, with varying degrees of fineness for various parts of the geometry. In the following, mesh size is defined as the side length of the grid triangles h_{feature}, and fineness is inversely proportional to this length. The mesh is finest at vertices and boundaries. The bulk fluid is somewhat coarser, and the bulk solid is even coarser still. To implement a parametric approach to mesh sizing, the viscous boundary layer ∂_s, introduced in section 2.6 is used as a characteristic length.

$$\delta_s = \sqrt{\frac{2\eta}{\rho\omega}} \approx 0.21\,\mu\text{m} \quad \text{for}\,\omega = 6.5\,\text{MHz} \tag{2.23}$$

The viscous boundary layer is a measure of how far wall effects influence the bulk motion. Large velocity gradients can be present within a few times this distance, so a resolution finer than this size is expected to be necessary.

The parametric approach involves relating all mesh sizes to a parameter of the fluid and solid each k_{p} & $k_{\text{p,solid}}$, so the proportional fineness of the mesh in the domain is maintained at all times. Along the boundaries $\partial\omega_4$, $\partial\omega_5$, $\partial\omega_6$ and $\partial\omega_7$ and all vertices the size of mesh elements h_{Edge} h_{Vertex} is defined as

$$h_{\text{Edge}} = h_{\text{Vertex}} = \frac{1}{k_{\text{p}}}\delta_s\,, \tag{3.18a}$$

where k_{p} is the parameter controlling mesh fineness.

In the bulk fluid, velocity and pressure gradients are a lot less prominent and a coarser mesh is appropriate. Moving from the boundaries towards the bulk, the mesh element size gradually increases with a fixed growth rate, up to a value h_{Bulk}

$$h_{\text{Bulk}} = \frac{50}{k_{\text{p}}}\delta_s = 50 h_{\text{Edge}} \tag{3.18b}$$

The factor 50 is chosen so that the bulk element size matches the fixed size used in Ref. [1] at $k_{\text{p}} = 5$.

In the full model, element size must be defined in the solid as well. This is done using yet another parameter, $k_{\text{p,solid}}$ which relates the size of the solid bulk elements to the fluid ones. Along the solid-fluid interface, the element size in the fluid and the solid are the same, while the size of bulk elements h_{Solid} in the solid is

$$h_{\text{Solid}} = \frac{1}{k_{\text{p,solid}}}h_{\text{Edge}} = \frac{1}{k_{\text{p,solid}}k_{\text{p}}}\delta_s \tag{3.18c}$$

With these parameters set, COMSOL will draw a mesh for both the simple and the full model, based on the values of k_{p} & $k_{\text{p,solid}}$, and assign the elements with test functions for all dependent variables. Section 3.4 shows a study of the optimal mesh parameters.

3.3.5 Solving options and results

The final step is solving the equation system defined through the steps above. Before solving the system, any conflicts in physics interfaces must be resolved. This can be done, by setting up

specific studies. In studies it can be specified which physics interface should be included, and which components the interfaces should be composed of. In this thesis, four studies are defined to investigate boundary condition simplifications. (*i*) A fluid domain with hard wall conditions imposed, (*ii*) a fluid domain with lossy wall conditions imposed, (*iii*) coupled fluid and glass domains, and (*iv*) coupled fluid and a polymer domains. Comparisons between results from studies (*i*) & (*iii*), and (*ii*) & (*iv*) should give insight into the validity of wall boundary conditions as replacements for full models.

3.4   Model validity

The model is verified through a check of boundary condition compliance, a mesh refinement study, and a comparison with simulations from the literature.

3.4.1   Coupling/boundary condition compliance.

To ensure the numerical model complies with the couplings and boundary conditions outlined in Sections 2.4 and 2.5, the coupled values are inspected along interfaces for which continuity is required. Fig. 3.2 shows sample compliance plots along the left fluid-solid interface $\partial\Omega_4$.
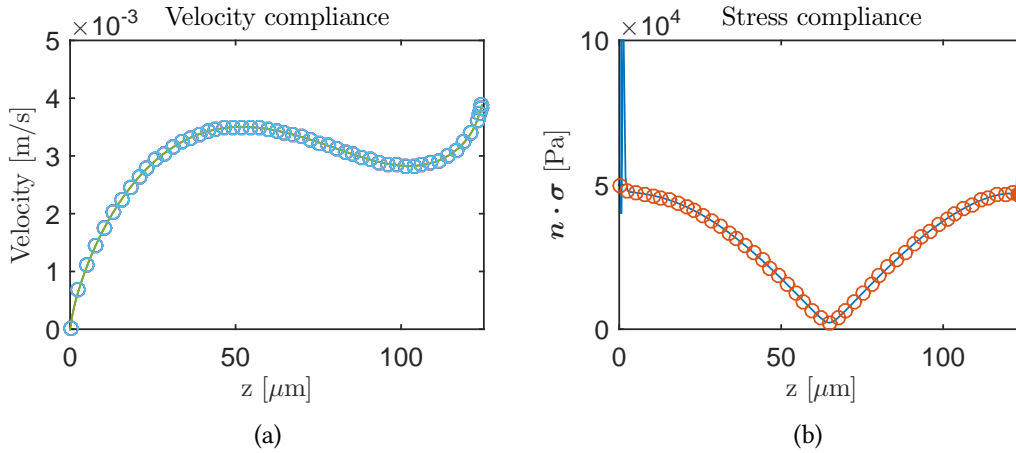

Figure 3.2: Boundary condition compliance evaluation along $\partial\Omega_4$. Circles indicate values in the fluid, while the line shows the values in the solid. The degree of congruence show coupling between domains. The velocity and displacement are perfectly coupled along the interface. The solid and fluid stress match well along the majority of the interface, but near vertices a numerical issue generates peak stresses. The effects are localized, however, and do not prevent convergence.

It is seen, that the couplings are generally complied along the boundaries. The velocity-displacement coupling from solid to liquid is entirely satisfied along the boundary, while the stress-stress coupling shows discrepansies at $z = 0$ and $z = 125\,\mu$m, e.g. at the top and bottom vertices. The same inspection is applied to all interfaces, which show same results, velocity and displacement are perfectly coupled, while the spatial derivatives diverge at vertices. It is shown

in the follow section, that these effects do not hinder convergence, and are thus considered not to affect the overall solution, but only act locally.

3.4.2 Mesh refinement study

To investigate the convergence of the model, a mesh refinement study is carried out. If the model converges, mesh parameter values exist at which decreasing element size only marginally increases the accuracy of the solution. Beyond this value, the added cost of computation is not made up for by better accuracy. The values may be found using a refinement study, which is performed by comparing solutions s, of increasing mesh fineness with a reference solution s_{ref}, where s is a field variable. Each field variable solution is compared to the reference solution, using the average relative variance of the field variable

$$C(s) \equiv \frac{\int_{\Omega}(s(\boldsymbol{r}) - s(\boldsymbol{r})_{\text{ref}})^2 \mathrm{d}A}{\int_{\Omega}(s(\boldsymbol{r})_{\text{ref}})^2 \mathrm{d}A}. \tag{3.19}$$

Ideally, s_{ref} is an analytical solution, but as one such does not exist for this problem, the solution for $k_{\text{p}} = 5$, i.e. a very fine mesh is chosen as reference. Figure 3.3 shows convergence plots for the lossy wall condition field variables, and for a modelled PDMS case.
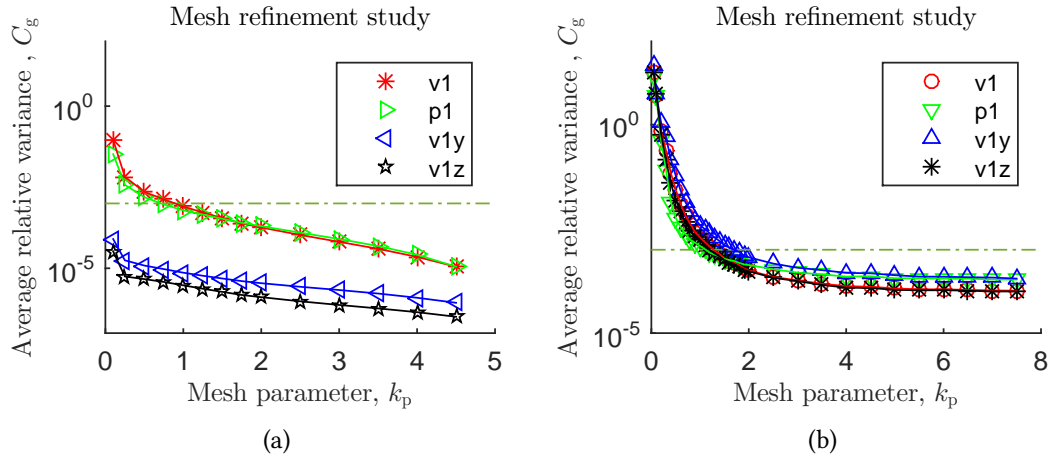

Figure 3.3: Fluid domain mesh refinement study results. The deviation from a reference solution of field values is shown as a function of mesh fineness, for the (a) lossy wall condition and (b) modelled PDMS. The dashed lines mark $C(s) = 10^{-3}$. Beginning at a given mesh parameter k_{p} the average relative variance will only decrease marginally with increasing fineness of the mesh. Beyond this point, the added solution accuracy is not worth the added computational cost.

The model clearly converges, as seen in Fig. 3.3. For mesh $k_{\text{p}} > 1$, the average relative variance is $C(s) < 10^{-3}$ for all field values. As the results are mostly of a comparative nature, 10^{-3} is an acceptable average relative variance. Hence refining the mesh beyond $k_{\text{p}} = 1$, will not be necessary in this thesis.

3.4.3   Comparison to literature

A final verification is made by comparing the model to simulation results from the literature and which correspond to an analytical solution. As shown in Ref. [15], acoustic eigenmodes exist in ideal water-filled rectangular channels. Placing a fluid domain in the y,z-plane with corners $(0,0)$ and (w, h) where h and L is the height and width of the channel. The analytical expression of the first order pressure field in such channels is

$$p_1(y, z) = p_\mathrm{a} \cos\left(k_y y\right) \cos\left(k_z z\right) \quad , \quad k_j = n_j \frac{\pi}{L_j},$$ (3.20)

where p_a is the pressure at walls, n_j is the number of half wavelengths in direction j, and $L_y = w$ and $L_z = h$.

It can easily be seen, that for the first eigenmode purely in the y-direction, i.e. a standing half-wave along the width of the channel; $n_y = 1$, $n_z = 0$, the pressure field is simply a standing cosine wave in the y-direction,

$$p_1(y) = p_\mathrm{a} \cos\left(\frac{y}{L}\pi\right).$$ (3.21)

The resonant frequencies of this eigenmode is found from Eq. 2.30 in Ref. [15]

$$f_{n_y,n_z} = \frac{c_{wa}}{2}\sqrt{\frac{n_y^2}{w} + \frac{n_z^2}{h}}$$ (3.22)

From this expression, the first resonant frequency in the y-direction is found as;

$$f_{1,0} = \frac{c_{wa}}{2w} \approx 1.17\,\mathrm{MHz}.$$ (3.23)

If the fluid is actuated symmetrically at this frequency, the system will settle into the eigenmode described by Eq. (3.21). At eigenmodes the acoustic fields of the system will be a superposition of the actuation response and the eigenmode, but compared to the eigenmode, the actuation response will be of a negligible magnitude, meaning the acoustic field will largely be independent of the actuation, as long as its symmetric and near the resonant frequency.

As seen in Fig. 3.4, the model compares well to analytical results, and bears resemblance to the results from Ref. [20]. Note, however, that the results shown are the physical values of the pressure fields at a given time t. In order to compare harmonic fields, the absolute value of fields should be compared to include time-dependence in comparisons, as be discussed in Section 6.1. The physical values are solely used here, to obtain a basis for comparing with Ref. [20].

3.5   List of assumptions

Below a list of assumptions, on which the numeric model is based are presented. Cases in which the assumptions are not upheld, cannot be expected to be represented using the model.

Table 3.3: List of assumptions made in the numeric model

| Assumption	Applied in
Acoustic perturbations are small	Perturbation theory
Linear displacements are small	Perturbation theory
Piezoelectric displacements can be approximated by analytic expression	Couplings and Boundary conditions
PDMS heating is neglected	PDMS modelling
Viscous boundary layers are small compared to particles	Acoustic radiation force
Particles are spherical	Acoustic radiation force
Walls do not yield	Hard wall boundary condition
Walls yield to pressure	Lossy wall boundary condition
No-slip condition along walls in	Hard and lossy wall boundary conditions
Only linear differential operators in governing equations	Weak formulation

(a)

(b)

(c)

(d)

(e)
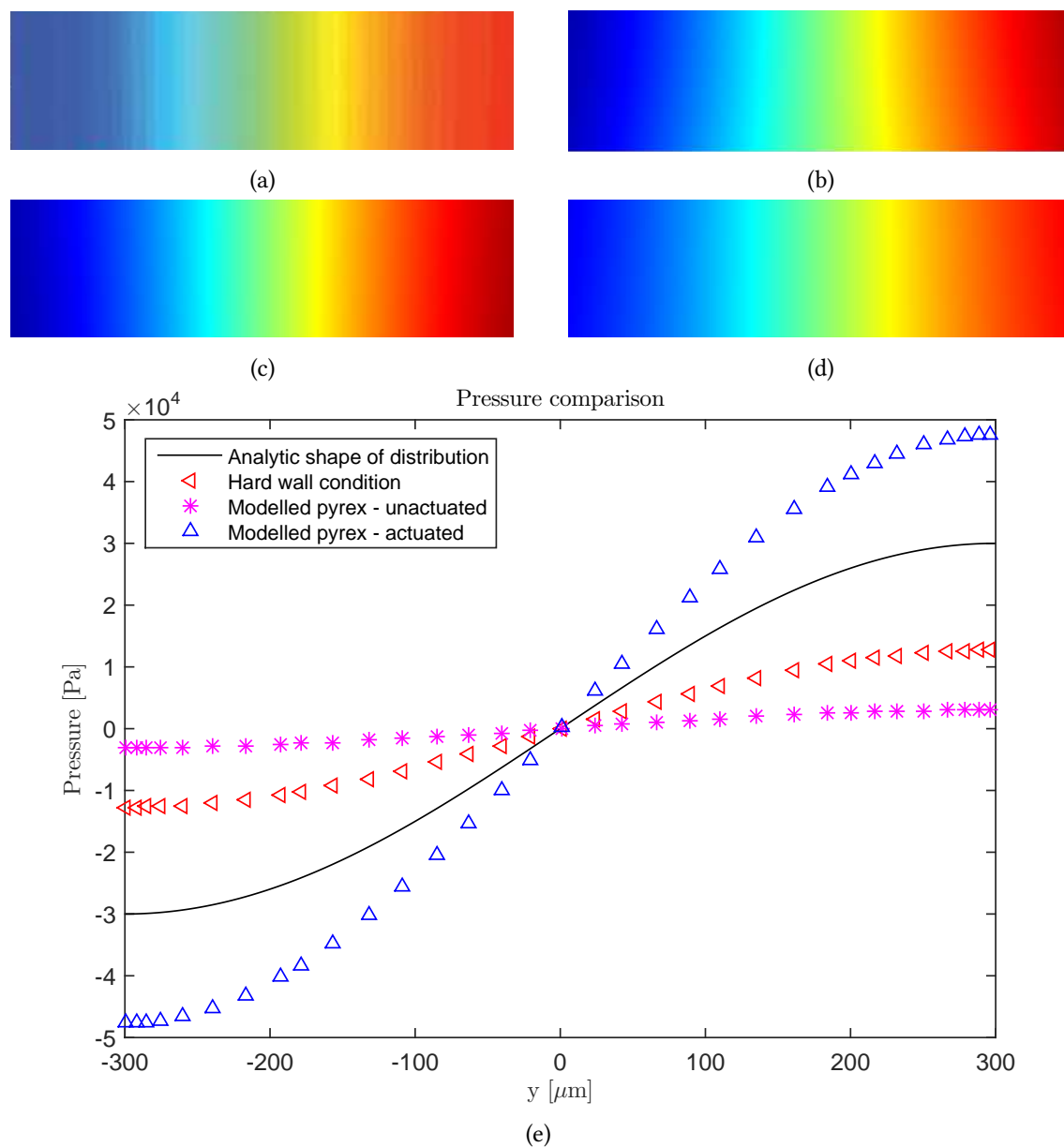
Figure 3.4: Qualitative result study. Fluid domains actuated at the frequency of the first acoustic eigenmode in the y-direction $f_{1,0}$. At this frequency, the first order pressure fields is described by a standing wave along the y-direction of the fluid. Values are not included as the comparison is qualitative. The color legends are, however, the same for (a), (b) and (c). (a) Result adapted from Ref. [20]. While the size and actuation frequency vary from the numerical model used here, the behaviour exhibited remains unchanged. (b) Simulation result using hard wall condition. (c) Simulation result including glass actuated by the SSAW. (d) Simulation result inclduing glas that **not** actuated. (e) Pressure profile along the horizontal centre-lines of the four cases shown above.

Chapter 4

Experiments

The experimental work of this thesis was carried out from the 26th of October to the 6th of December at the Microfluidics Research Group[1] headed by Bjørn T. Stokke, at the Norwegian University of Science and Technology NTNU in Trondheim. The purpose of the group's ongoing experiments is to realize selective particle manipulation of sub-micron particles based on mechanical properties, utilizing the acoustic radiation force, paired with streaming drag. While the group has a high level of experience with experimental work, yours truly was able to contribute in an advisory role regarding fluid mechanics. For the author of this thesis, the main aim of the visit was to work on a tool to experimentally verify the numerical model. However, due to technical difficulties at NTNU beyond the control of the author, no verification has been achieved by the deadline of this thesis. However, an insight into the relation between the physical and the numerical aspects of SAW was obtained, and an automation program to improve future experimental work was developed, as described in Chapter 5.

This chapter gives a brief introduction to the devices and the set-up used, as well as manufacture of said devices. The chapter is mainly dedicated to put the automation program into perspective, and provide talking points on the connection between theoretical and experimental work.

4.1   Device and set-up

Only a very limited amount of work had been done with regards to surface acoustic waves at NTNU. Hence, the devices used in experiments were designed to have parameters similar to a functioning device from the literature[7], and may not be ideal.
Each device consists of three components; (*i*) A polydimethylsiloxane (PDMS) microchannel attached on top of (*ii*) a substrate of $128\,^\circ$ XY-cut lithium niobate $LiNbO_3$ (LN). The substrate has two gold interdigital transducers (IDTs) etched on top of it. The LN is placed on top of (*iii*) a microscope slide modified to act as a connection between the device and the signal generator. The PDMS and substrate chips are single-use while the microscope slide is reusable. The designs of the PDMS and LN masks, and the final assembly are shown in figure 4.1. The manufacture

---

[1]http://www.ntnu.edu/microfluidics/

of each of the components as well as the assembly of the final device are described in detail in section 4.2.

Table 4.1: Approximate device dimensions and actuation parameters used in the experiments.

	PDMS	**Channel** Ω_2	**Actuation parameters**	
Width	$\approx 1250\,\mu m$	$60\,\mu m$	Frequency	$\approx 39\,MHz$
Height	$10\,000\,\mu m$	$40\,\mu m$	Wavelength	$100\,\mu m$

Device design

A centre/inner flow and a sheath/outer flow are introduced *via* two inlets. The sheath flow is divided into two identical flows. The centre flow contains polydisperse solution to perform particle manipulation on, while the outer flow is a suitable sheath fluid - usually ultra pure water. The centre flow and the two sheath flows are united at a junction, with the sheath flow encasing the centre flow on both sides. In the x,z-plane the centre flow is thus bounded to the sides by the sheath flows, upwards by the channel and downwards by the substrate. A short distance beyond the junction, the fluid enters the active region of the channel adjacent to the IDTs. This is the region modelled in the numerical simulations.

A transition region exists on both sides of the active region, wherein the acoustic fields vary in the x-direction. Beyond the active region and the following transition region, the flow runs to another junction, where the flow is split into a centre flow, and two outer flows. The centre flow is led to an outlet, and the outer flows are connected and led through a single outlet.

Set-up

The set-up is comprised of two syringe pumps, 'Pump s' and 'Pump C' (Harvard Apparatus PHD Ultra), a signal generator (Agilent AG33611), an amplifier with radio frequency-capabilities (AMP), an oscilloscope (Agilent DSO1001A), and an inverted microscope (Olympus IX70) with mounting possibilities for a sensor or an SLR.

Both 'Pump s' and 'Pump C' contain a single syringe. The syringe in Pump s is filled with a sheath fluid, usually ultra pure water. The solution subject to particle manipulation is filled in the syringe in Pump C. For simple validation experiments this will generally be a polydisperse solution of polystyrene beads in ultra pure water. The syringes of Pump s are connected to the outer inlet, shown on Fig. 4.1, while the syringe in Pump C is connected to the centre inlet.

The signal generator is connected to the amplifier. The output from the amplifier is split in two identical signals and connected to the modified microscope slide presented in Section 4.2.7 and shown in Fig. 4.2. The slide is placed on the microscope. Using the sensor the a portion of the X,Y-plane of the channel can be monitored using the program 'Photron FASTCAM viewer', which also allows for pictures to be taken. If the observed particles are fluorescent, the appropriate light source and filter are turned on to observe the particles in the microscope.
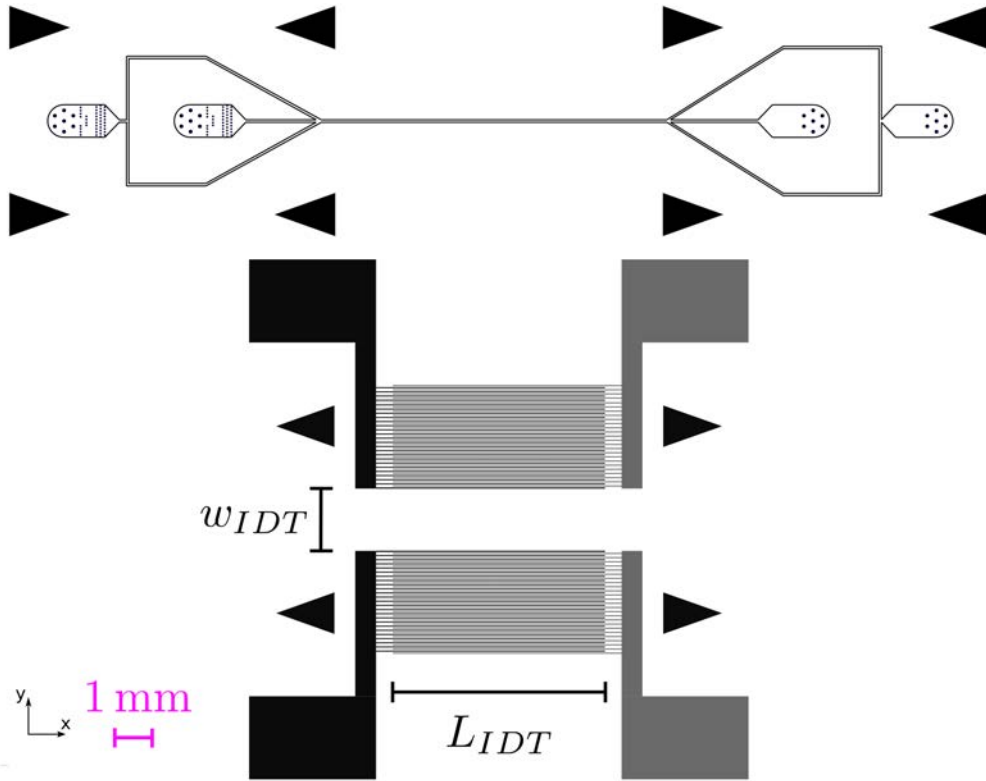
Figure 4.1: Design masks used in photolitography to create the PDMS master mould, and the IDT substrate chips. PDMS design contains two inlets, two outlets, two junctions and an active region where SSAW in the substrate interact with the fluid. Substrate design contains design of two IDTS. IDTs are closely spaced electrode lines that are connected to ground and signal inputs. The arrows indicate alignment marks, used when bonding the PDMS and substrate together. $w_{\text{channel}} = 60\,\mu\text{m}$, $w_{\text{IDT}} = 15\lambda = 1500\,\mu\text{m}$, $L_{\text{IDT}} = 5100\,\mu\text{m}$

4.2 Factors influencing experiment

When considering the entire process from designing a chip to running experiments, a plethora of circumstances influence the microchip's behaviour. The following sections will describe certain aspects of the process that may influence the behaviour and discuss their relation to the numerical modelling of the problem. While many of the factors mentioned may only affect the system marginally, the superposition of insecurities can make the behaviour of the system radically different from the one expected based on simulations. The main points of the following sections are summed up in Table 4.2.

4.2.1 PDMS mask design

The achieved particle manipulation is highly dependent on both the cross-sectional geometry of the channel and the geometry in the x,y-plane of the chip. The cross-sectional geometry of
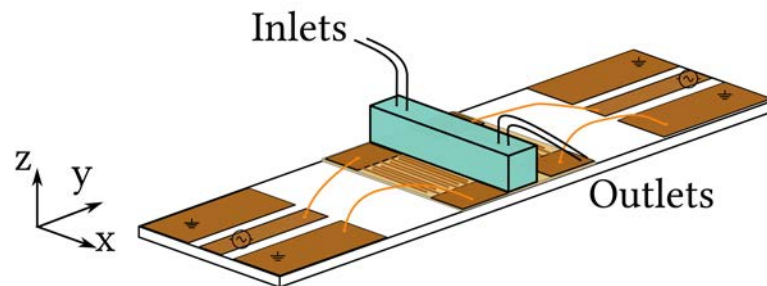
Figure 4.2: The finished PDMS microchannel is permanently bonded to the lithium niobate by oxygen plasma bonding. The lithium is in turn attached to the modified microscope slide using double-sided tape, to enable repeated use of slides in devices. Terminals of the IDTs are wire-bonded to the terminals of the glass slide, shown as orange lines. In this case, the IDTs with the innner-most electrode is connected to the signal, while the outermost is ground. Connections to the signal generator are soldered onto each end of the slide to create the terminals shown.

Factor:	Introduced during:	Influence on:	Accounted for in model:
Channel width	PDMS mask design	Rentention time in channel. Velocity distribution in y,z-plane	Yes
Channel layout	PDMS mask design	Ratio φ_{eq}	No
IDT Wavelength	IDT mask design	Resonant SAW frequency. Ideal excitation frequency	Yes
Channel height	PDMS Master mould fabrication	Rentention time in channel. Velocity distribution in y,z-plane	Yes
PDMS Young's modulus and Poisson's ratio	PDMS chip fabrication	Fluid-solid interface interactions.	Yes
IDT quality	Substrate manufacture	Resonant SAW frequency, SAW amplitude	No
IDT-material orientation	Substrate manufacture	SAW propagation speed. Resonant frequency	Yes
System leakage	Microchannel-substrate bonding	Flow in all three directions and total flow rate	No
Channel-IDT misalignment	Microchannel-substrate bonding	SSAW actuation symmetry	Yes
Channel-IDT skewness	Microchannel-substrate bonding	SSAW-channel parallelism	No
Solution concentration	Experiments	Possible particle-particle interactions	No
Sedimentation	Experiments	Flow conditions and acoustic fields	No
Diffusion	Experiments	Particle distribution across channel	No

Table 4.2: Factors affecting experimental results. A list of factors that may influence particle separation. Note the list covers influences most likely to affect particle separation but is not exhaustive

the chip determines the two-dimensional velocity distribution along the flow direction. It can be approximated by the expression,

$$v_x(y, z) = v_f(A, \dot{V}) \sum_{n,\text{odd}}^{\infty} \frac{1}{n^3} \left[1 - \frac{cosh\left(n\pi\frac{y}{h}\right)}{cosh\left(n\pi\frac{w}{2h}\right)} \right] sin\left(n\pi\frac{z}{h}\right) , \qquad (4.1)$$

where $v_f(A, \dot{V})$ is a function of the cross-sectional area A and total volumetric flow $\dot{V}$, and w is the channel width, and h is the channel height.[21]

The cross-sectional geometry also affects the position and magnitude of pressure and velocity nodes, and consequently the features of the acoustic radiation force. Figure 4.3 shows an analytical solution to the velocity distribution in four different rectangular flow situations, all with no-slip conditions along the walls. Also illustrated is the influence of alignment insecurity as outlined in section 4.2.6. The factors in the x,y-plane of the chip that primarily affect the flow are path lengths and junction angles, as they determine the path of least resistance through the system. In the current chip design, the sheath flow path is much longer than that of the centre flow, which creates a tendency for sheath flow to exit through the centre outlet. Similarly, the more obtuse the angle at the junction near the outlets, the less flow will exit through the outer outlets. This factors into the value of the equilibrium ratio introduced in 4.2.7.

4.2.2 IDT design

The design of the IDT determines the wavelength and resonant frequencies of the generated SAWs. The main resonant frequency appears where wave generation and wave propagation are matched in the IDTs. At resonance, generated wave should have propagated one wavelength - 4 times the electrode width - when the next wave is generated. Consequently, at resonance waves generated in the centre of the IDTs are amplified at each electrode pair it passes. The theoretical resonant frequency is found by matching the time it takes to propagate one wavelength to the period of wave generation, i.e.

$$f_{\text{res}} = \frac{\lambda}{v_{\text{SAW}}} \approx 39.0\,\text{MHz}, \qquad (4.2)$$

where $\lambda = 4w_{\text{elec}}$ is the designed wavelength and v_{SAW} is the material- and orientation-specific surface acoustic wave propagation speed. The section on network analysis, in particular Fig. 4.4 illustrate resonance of IDTs.

4.2.3 PDMS chip fabrications

A master mould is necessary. A master mould based on the design shown in Fig. 4.1 is made on a silicon wafer using optical photolitography. The height of the mould, and thus the channel depend on the photo-resist used and the intensity of the photolitograph. Only a single master mould is needed per design, as it is reused for each chip made.

PDMS is made by mixing Sylgard 184 pre-polymer and cross-linking agent in the recommended 10:1 ratio, and stirring rigorously. The PDMS is degassed in a vacuum desiccator for at least 5 minutes, and poured over the master mould in a Petri dish, to a height of approximately
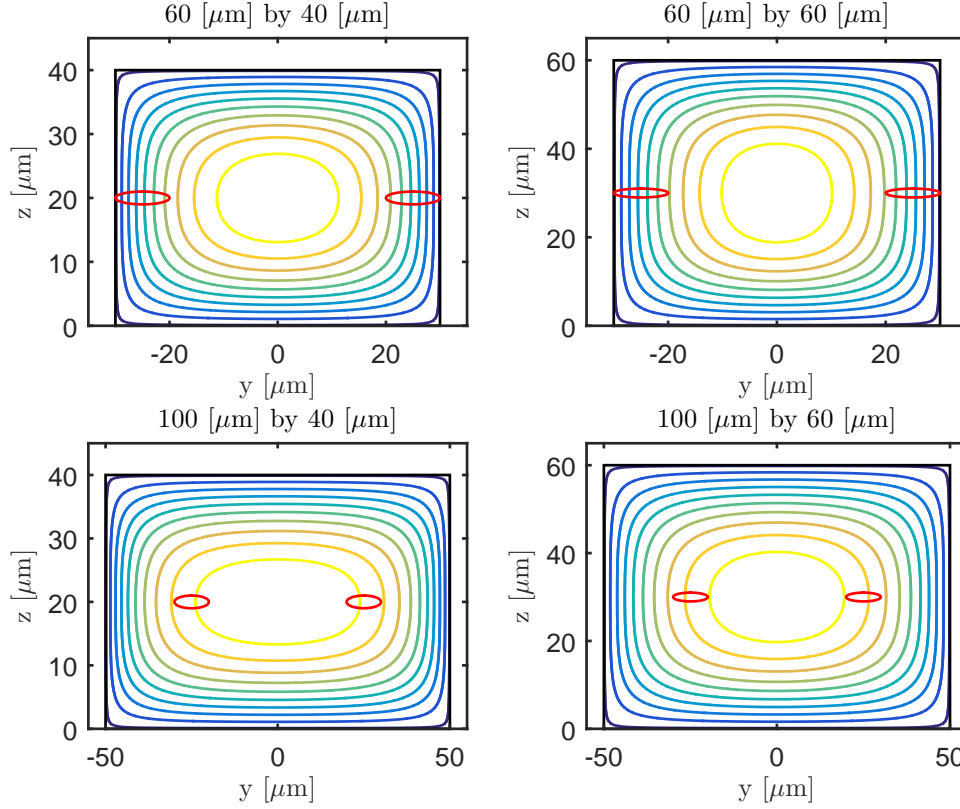
Figure 4.3: Normalized velocity contour plot for various cross-sectional dimensions based on an analytical expression. Contours mark 10 %, 20 %, ... , 90 % of maximum velocity $v_f(A, \dot{V})$. Assuming pressure anti-nodes are spaced $50\,\mu$m apart, the ellipses mark the variation in anti-node position, assuming a $5\,\mu$m insecurity range. While the acoustic fields are dependent of channel geometry, the figure illustrates the necessity of alignment precision resulting from small microchannels.

1 cm. The PDMS is then cured at $65\,°$C for at least two hours. With a scalpel, a cut is made in the PDMS, large enough to gently pull the chip from the master mould, saving the master mould in the Petri dish until next chip is made. The chip is cut to a size so the arrows barely fit on the chip. Along the channel, cuts are made leaving a clearance of approximately 0.5 mm, as shown in 3.1. Finally, holes are punched to form inlets and outlets, in the designated areas.

As mentioned in 2.7, the mechanical properties of PDMS are known to depend on the mixing ratio and curing temperature [16, 17]. Lower ratios of cross-linking and lower curing temperature decrease the longitudinal sound of speed, which increases the Poisson's ratio, increasing the difficulty of numerically modelling the system. Thus it is important to ensure the recipe above is followed. Both for repeatability of experiments, and to enable numerical modelling of the problem. Proper mixing of the PDMS is also crucial, as explained in Section 4.2.6.

Another problem that arises in manufacture is the varying width and height of the PDMS.

As there are no marks in the design to cut by, the width along the channel will invariably differ from chip to chip, and likely even vary between either side of the channel. On top of this, the height of the PDMS varies. Variations in the dimensions may result in discrepancies in acoustic fields, so an approach that ensured nearly identical PDMS chips is desirable.

4.2.4   Substrate manufacture

A 20 by 25 mm chip is cut from a Lithium Niobate wafer, and the major axis of the substrate is marked with a non-permanent marker. After rinsing and drying the substrate, a layer of photo-resist is added and spun, to make a layer of uniform height on the substrate. The substrate is pre-heated for a minute on a hot plate at 55 °C, and subsequently baked at 90 °C for 1 minute. The substrate is placed in a mask aligner, with the major axis of the substrate aligned with to the design mask. The imprint of the UV-light in the photoresist is developed, leaving only exposed photo-resist on the substrate. Using thermal evaporation a 5 nm titanium layer is added on top of the photo-resist, followed by a 80 nm gold layer. After sputtering, the remaining photo-resist is dissolved in acetone, leaving only the metallic IDT deposition on the substrate.

Correct alignment of the mask and the major axis is important, as any deviation from parallelism will change the resonant frequency of the chip. If the IDT is misaligned, the applied frequency must be changed to achieve resonance on the substrate, which in turn changes the behaviour of acoustic fields. Another factor regarding IDT manufacture is the achieved quality. The metallic deposition or photoresist imprint may both be flawed, leading to a deviation from the design on the final chip. The resonant frequency on chips has been seen to vary, which may be caused by chip deviations from design.

4.2.5   Network analysis

While network analysis adds no insecurity to the experiments, the concept will be utilized in the following chapter, and an introduction here is thus appropriate.

To test the chips produced using a given design, network analysis is performed using a vector network analyser. As it is carried out on an expensive piece of equipment it is only performed once per design. Network analysis is a tool to measure the relation between input and output at different ports of an electronic circuit, described via *scattering parameters* $S_{\alpha,\beta}$, measured in dB. The IDTs on substrate chips can be considered as ports, and the chip a two-port system. Assume power is input at one IDT, here named port 1. The reflection coefficient, $S_{1,1}$ describes the amount of power leaving the system again at port 1, while the admittance coefficient $S_{2,1}$, describes the amount of power leaving the system at port 2, i.e. the other IDT. Vice versa coefficients $S_{2,2}$ and $S_{1,2}$ describes reflection and transmittance coefficients from port 2. Scattering parameters depend on input frequency, with optimal transmittance and minimal reflection at resonant frequencies.

The analysis is performed by alternately inputting power from ports 1 and 2 in a closed circuit and a short-circuit case and measuring the reflected and transmitted powers. The output of the test is the scattering parameters as functions of input frequency over a span of interest - 30 MHz to 40 MHz in this case. The optimal operating frequency of the chip, i.e. the frequency at which most energy is transmitted through, can be found by plotting the scattering parameters

as a function of frequency. At resonance reflection coefficients are minimal, while transmittance values reach maximum values. Physically this means a lot of energy is transported through the system and little is reflected out, i.e. meaning maximum displacements and efficiency. The S-parameters of the original chip design are shown in Fig. 4.4.
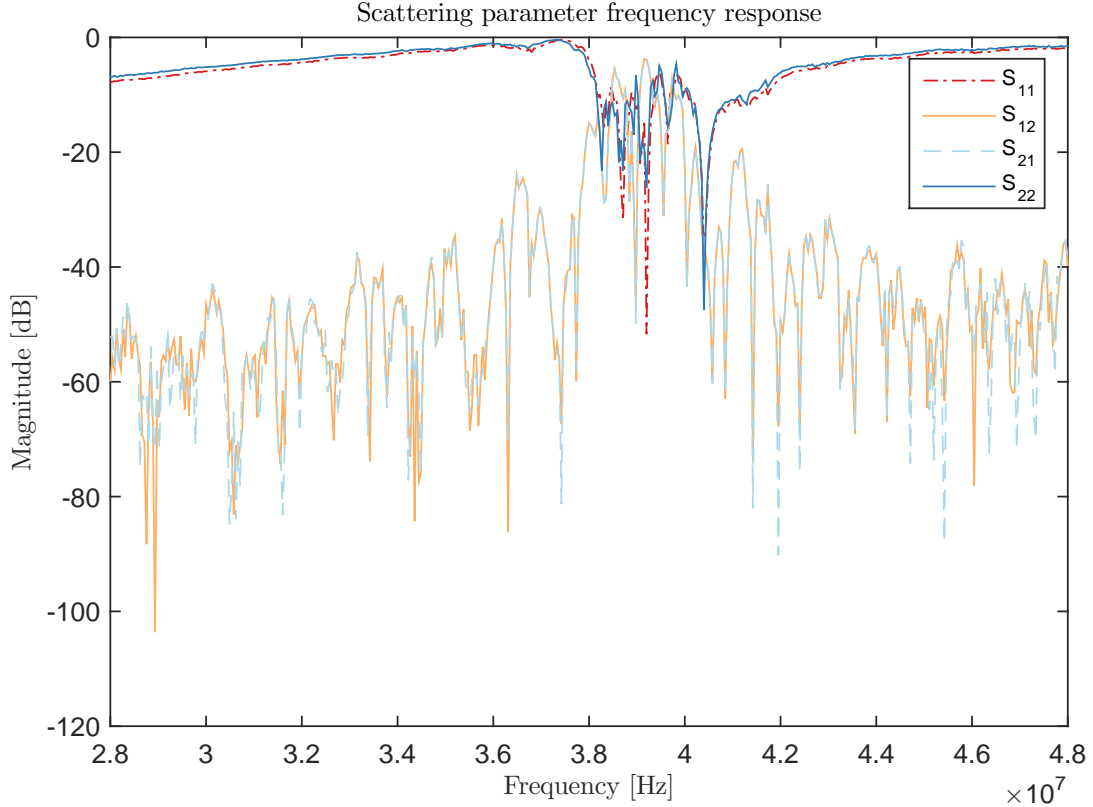

Figure 4.4: IDT Scattering parameters. By performing network analysis on IDT substrate chips, transmittance and reflection coefficients are found as functions of frequency. At resonance, there is minimal reflection in the system, i.e. $S_{1,1}$ and $S_{2,2}$ are low, while transmittance coefficients $S_{1,2}$ and $S_{2,1}$ are at their highest. As explained in Section 4.2.2, this occurs near $\dfrac{\lambda}{v_{\text{SAW}}} \approx 39\,\text{MHz}$. A chip with a misaligned IDT design would show resonance at a different frequency.

4.2.6 Microchannel bonding on substrate

The surfaces to be bonded are activated by exposure to oxygen plasma in a plasma cleaner. A drop of ethanol is applied to the substrate before placing the chip on top of it. The substrate and chip are aligned under a microscope using tweezers, with alignment marks on both designs acting as a visual aids in alignment. As the ethanol evaporates, the activated surfaces come into contact, forming covalent bonds. Thus, the time available to align the substrate and chip is limited by the size of the ethanol drop.

Proper alignment of the microchannel on the substrate is important, in order to obtain symmetry in the y-direction, with regards to the SSAW and flow in the x-direction. The red ellipses Fig. 4.3 illustrate the large variations in x-velocity that can be introduced on the current chip for an alignment insecurity of just $5\,\mu m$. Due to the soft nature of PDMS it can also easily be twisted askew when aligning the chip and the substrate. The IDTs and the channel may thus deviate from parallelism, adding non-zero acoustic field components in the x-direction, i.e. $\partial_x s \neq 0$.

PDMS Hydrophilicity In order to properly bond the chip and substrate, it is crucial to properly mix the PDMS during chip manufacture. If PDMS is not properly mixed, the mechanical properties of PDMS are not isotropic, which cause poor bondings, which in turn cause fluid leakages. Poorly mixed PDMS seems to be turn less hydrophilic during plasma treatment. If leakages occur frequently, hydrophilicity of the PDMS used should be quantified. A quick method developed for this is outlined in Chapter A.

4.2.7   Modified microscope slide and wire-bonding

The modified microscope slide serves as a connector between substrate and signal generator. A gold pattern of two wide rectangles and a single thinner slit are sputtered onto the slides, and SMA radiofrequency connectors are welded onto each end of the slides, connecting the wide blocks to the ground and the single slit to the signal pin.

The substrate chips are taped on to the microscope slide using double-sided tape to allow reuse of the microscope slides. The inner connector pad of both IDTs is connected to signal, and the outer is connected to ground. If the connections to connector pads are asymmetric, there will be a phase difference of between the SAW propagating from the left and right sides of the channel. This will in turn shift the SSAW to the side, causing an asymmetric actuation of the fluid.

Experiment factors

Essentially, four factors are of importance when running experiments on a finished device. The 'flow factors': flow ratio and total flow $[\mu l\,h^{-1}]$, and the 'field factors': signal generator frequency [Hz] and amplitude [V].

Flow factors. The flow rates of the inner and outer flows affect the flow distribution and particle concentrations at the outlets. Consider a channel of length L_c and width w_c as shown in Fig. 4.5. A polydisperse solution and a sheath liquid of ultra pure water are introduced via inlets with volumetric flow rates $\dot{V}_{ps}$ and $\dot{V}_{sf}$. The ratio of flow rates φ between the two flows and their sum $\dot{V}_t$, dictate the concentrations of flows leaving the chip at the outlets.

$$\dot{V}_t = \dot{V}_{sf} + \dot{V}_{ps} \,, \tag{4.3a}$$

$$\varphi = \frac{\dot{V}_{sf}}{\dot{V}_{ps}} \,. \tag{4.3b}$$

Based on these some observations regarding exiting concentrations, when no SAW is present, can be made.

Exiting concentrations. For a given geometry, a ratio $\varphi = \varphi_{\text{eq}}$ exists, at which the two flows do not mix, i.e. all the sheath fluid enters and leaves at the outer outlets. It is assumed that particles will solely be transported by advection, i.e. follow streamlines in the fluid. Based on this the relation between φ and φ_{eq} determines the exiting concentration of both flows. For $\varphi > \varphi_{eq}$, some of the polydisperse solution will exit the chip via the outer outlet, leading to a non-zero particle concentration at the outer outlet, while the flow exiting the inner outlet is undiluted. At equality, the solutions of both flows is unaltered. For $\varphi < \varphi_{eq}$ some of the sheath fluid will exit through the inner outlet, diluting the polydisperse solution. The three cases are illustrated in Fig. 4.5.

(a) $\varphi < \varphi_{eq}$ (b) $\varphi = \varphi_{eq}$ (c) $\varphi > \varphi_{eq}$
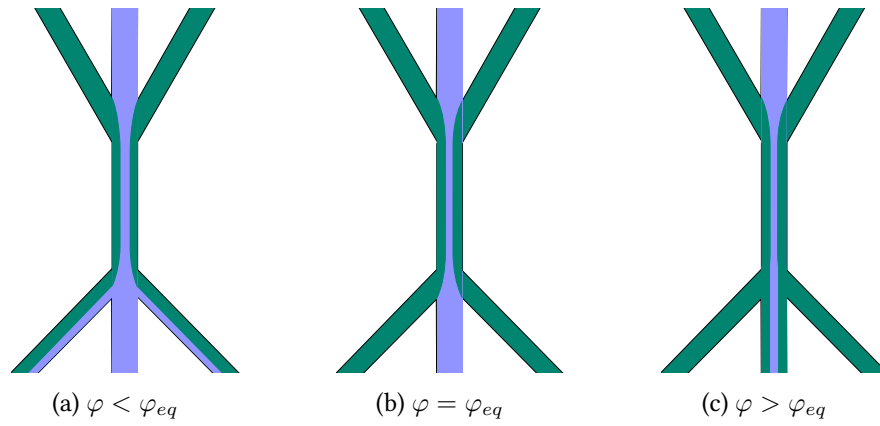
Figure 4.5: Flow scenarios for varying flow ratios. A centre flow containing particles is surrounded by a sheath fluid, containing no particles. Assuming particles are solely transported by advection, the particle paths are described by streamlines. Streamlines are determined by the ratio of flows φ compared to an equilibrium ratio φ_{eq}. (a) If the ratio is lower than the equilibrium ratio, some stream-lines from the centre flow will exit via the outer outlets, mixing particles into the sheath fluid. (b) At equality, the two flows will not mix, and particles will solely exit via the inner outlet. (c) Above the equilibrium ratio some of the sheath flow will exit via the inner outlet, diluting the centre flow.

Diffusion. The assumption that particles follow streamlines requires that no diffusion takes place along the length where the flows are adjacent. The validity of this depends on particle diameter a, and the total volumetric flow rate $\dot{V}_t$. To get a worst-case estimate of the diffusion coefficient, the smallest values of these are used; $a = 0.3\,\mu\text{m}$, $\dot{V}_t = 5\,\mu\text{L}\,\text{h}^{-1}$.

The time a particle spends in the channel is called the retention time, τ. While this time depends on the mechanical properties and entering position in the y,z-plane of particles, a mean value, $\overline{\tau}_{\text{r}}$, can be found based on the channel cross-sectional area A, and length L_{c}, and typical values of the total flow rate,

$$\overline{v} = \frac{\dot{V}_t}{A} \approx \frac{10^{-12}\text{m}^3\,\text{s}^{-1}}{10^{-9}\text{m}^2} = 10^{-3}\text{m}\,\text{s}^{-1}\,, \tag{4.4a}$$

$$\overline{\tau}_{\text{r}} = \frac{L_{\text{c}}}{\overline{v}} \approx \frac{10^{-3}\text{m}}{10^{-3}\text{m}\,\text{s}^{-1}} = 1\text{s}. \tag{4.4b}$$

	$a = 300\,\mathrm{nm}$	$a = 1\,\mathrm{\mu m}$	$a = 10\,\mathrm{\mu m}$
$\dot{V}_t = 10\,\mathrm{\mu L\,h^{-1}}$	$146\,\mathrm{\mu m}$	$80\,\mathrm{\mu m}$	$25\,\mathrm{\mu m}$
$\dot{V}_t = 100\,\mathrm{\mu L\,h^{-1}}$	$46\,\mathrm{\mu m}$	$25\,\mathrm{\mu m}$	$8\,\mathrm{\mu m}$
$\dot{V}_t = 500\,\mathrm{\mu L\,h^{-1}}$	$21\,\mathrm{\mu m}$	$11\,\mathrm{\mu m}$	$4\,\mathrm{\mu m}$

Table 4.3: Diffusion lengths for a selection of flow rates and particle sizes. The span of flow rates and particle sizes shown cover the ones used.

Based on the retention time, an estimate of diffusion length L_d, can be found using the

$$D = \frac{k_\mathrm{B}T}{6\pi\eta a} \quad \approx 10^{-12}\mathrm{m^2\,s^{-1}}\,, \tag{4.5a}$$

$$L_\mathrm{d} = \sqrt{4D\overline{\tau}_\mathrm{r}} \approx 10^{-5}\mathrm{m}\,, \tag{4.5b}$$

where D is the diffusion coefficient, and k_B is Boltzmann's constant. The diffusion coefficient is calculated using the Stokes-Einstein-Sutherland equation, which is valid for spherical particles - much larger than the solvent particles - in a low Reynolds number flow.

As the mean diffusion length of particles is on the order of $10\,\mathrm{\mu m}$, it is deemed unreasonable to neglect diffusion along the channel for the example values used. From Eq. (4.5) it is clear that diffusion length scales with $L_\mathrm{d} \propto \sqrt{a^{-1}\overline{v}^{-1}}$. As polydisperse solutions are used in experiments, diffusion lengths will differ for the particles in the suspension, with smaller particles diffusing to a larger extent. As the smallest particle size was used in calculating the diffusion coefficient, particle diffusion will be smaller for the remaining particles. Similarly, most flow rates used will be higher, leading to less diffusion. Adding further to the complications, the velocity will vary from zero at walls to a value v_max at the centre of the channel, as shown in Fig. 4.3. This leads to particles having widely different retention times, and thus widely different diffusion lengths.

The takeaway is that for sufficiently high flow rates, the particle motion of most particles in the flow can generally be described by streamlines. Deviations from this increases with decreasing particle size and distance from walls. Table 4.3 shows the diffusion length of particles of various size for various volumetric flow rates. It is apparent, that submicron particles even at the highest flow rates shown show substantial diffusion. Note, it is thus easier to separate large particles from small ones, than vice versa.

Sedimentation. Particles moving along the channel may come into contact with walls either due to diffusion or to forces acting on them, e.g. gravitational forces or the acoustic radiation force. As particles near walls and enter the viscous boundary layer, the surrounding fluid velocity substantially decreases, reaching zero at walls due to the no slip condition. As the Stokes drag is proportional to the relative fluid, particles in close proximity to the walls will nearly come to a standstill. Hence, a build-up of particles will form when running experiments for an extended duration. These particles may aggregate into larger agglomerates, which can affect the flow conditions and acoustic fields within the channel. Periodic flushing of the chip with large amounts of ultra pure water may clear out some of the sedimentation, but during runs it is impossible to avoid entirely.

Field factors. The amplitude and frequency of the signal generator affect the character of the SAW. For a given frequency, the voltage amplitude of the signal is directly proportional to

the displacement amplitude of the SAW. The amplitude of the displacement is proportional to the intensity of the acoustic fields generated in the liquid, which in turn is proportional to the acoustic radiation force.

The frequency determines the frequency of the SAW, and also influences the displacement amplitude of the signal, with displacements peaking at resonant frequencies, as mentioned in Section 4.2.2.

Approach

In summary, flow and field factors collectively determine effective particle migration along the channel. The flow ratio affects the tendency of particles to stay within the centre of the chip, while the total flow determines velocity, which in turn influences the effective time particles experience the acoustic radiation force and the degree of diffusion along the chip. Field factors determine the amplitude and frequency of the standing surface acoustic wave, which is related to the magnitude of the acoustic radiation force. By balancing the factors, particles can be selectively sorted based on mechanical properties, as illustrated in Fig. 4.6. The factor balancing is performed using tedious a one-factor-at-a-time (OFAT) approach. This results in low empirical resolution, increases the risk of human error in measurements and data acquisition, and requires simultaneous handling of 4 pieces of equipment. To alleviate these problems and increase the utilization of equipment, the program described in chapter Chapter 5 was developed.

4.3 Relating experiments to numeric model

In order to use experimental results to verify the numerical model, some congruence between the two is necessary. The experiments are inherently 3D, but can currently only be observed in 2D, namely in the X,Y-plane. The numerical model, however, can be used to describe acoustic fields, and estimate particle movement in the Y,Z-plane in the active area. Thus the experiments and the model can only be compared based on the Y-position of particles in a stop flow situation on the device.

As outlined in the above, experiment outcome is influenced by each step of the experiment from conception through execution. In order to numerically model the experiments, all factors should be accounted for in some way. This is, however, in no way feasible. As shown, some factors in Table 4.2 cannot be accounted for in the model in its current state, while others more can. The geometry and mechanical parameters of the model are examples of factors which can readily be changed, if the physical value is actually known.

Other factors such as sedimentation, diffusion and particle-particle interactions are possible to model, but would require implementation of new physics interfaces, at the cost of increased model complexity, i.e. risk of errors,. By adding a third dimension to the model, and modelling the piezoelectric motion, the effect of having non-parallel SSAW and channel could also be modelled, causing higher computational requirements.

In conclusion, a numeric model can always be expanded to take an increasing number of factors into accont. From a simple cost-benefit point of view, it is decided that it is neither reasonable or worthwhile to expand the numeric model to include the all the above mentioned effects, at the current point. It is, however, important to bear in mind that they may come into

play, and to realize that a numeric model only estimates reality as well as its assumptions are valid.
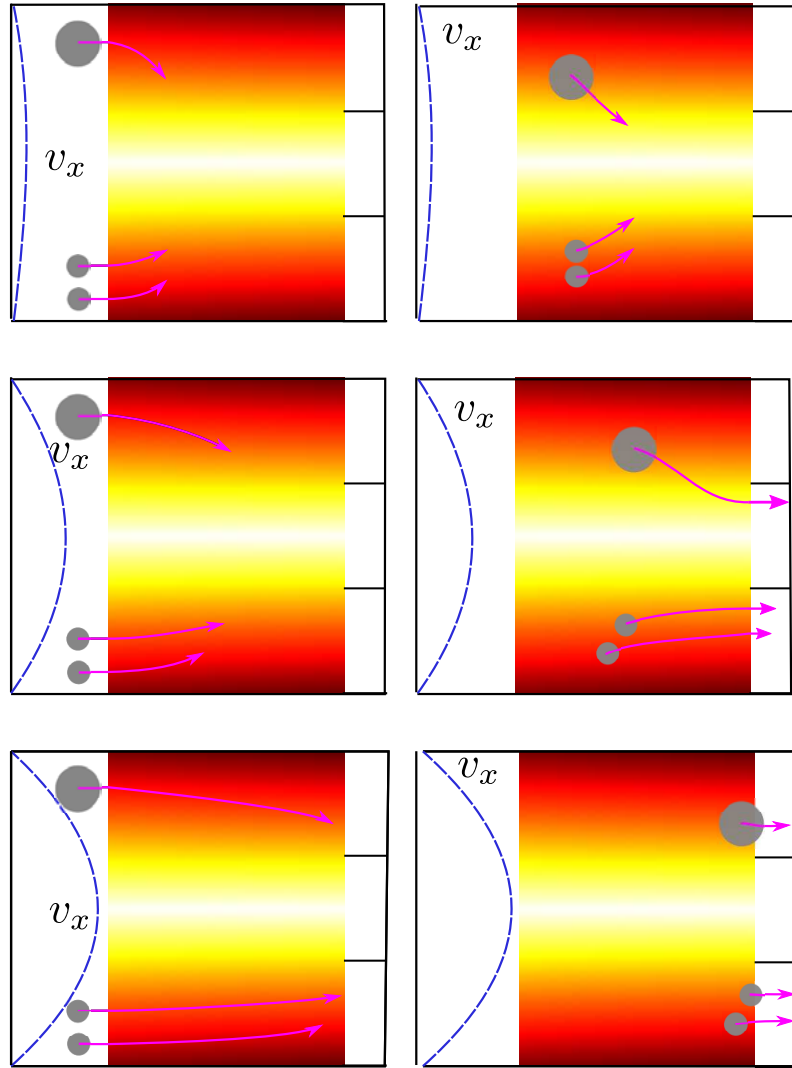
Figure 4.6: Experiment factor balancing. By balancing the advection of particles with the magnitude of the acoustic radiation force, selective particle separation can be achieved. Vertical lines indicate the division into three outlets. (above) At slow velocities, particles have long retention times in the active area. The radiation force dictates movement towards the centre outlet, through which all particles leave. (middle) A balance is struck between advection and the acoustic radiation force, causing particles of a given size to exit via the center outlet, while smaller particles leave in outer outlets. (below) At high flow rates, particles will have little retention time in the active area, and all particles leave through outer outlets regardless of size.

Chapter 5

Automation program

As mentioned in the previous chapter, the method of carrying out experiments at the group stood to be improved. The method requires little decision-making, but demands consistency for results to be useful and a lot of time to get good experimental resolution. As such, the method is perfectly suited for automation. As the author has substantial prior experience with the programming environment LabVIEW, an automation program was developed using this.

This chapter gives an introduction to the programming environment in which the program is developed, describes the development process of the program, and details the program in its current state. For brevity, the program will not be presented in its entirety within the thesis, as the primary focus is on the development of the program, and not the specifics of programming in LabVIEW.

5.1 LabVIEW

LabVIEW[1] is a programming software, catering specifically for engineering purposes. Programs in LabVIEW can be designed to run on PCs or a number of designated data acquisition hardware. The program in question here runs on a PC. LabVIEW is a graphical programming environment meaning functions are represented by symbols and data connections is shown by wires connecting functions. Thus, LabVIEW programs can often be read much like a flow chart would be. Fig. 5.1 shows a minimal comparison between classical text-based coding and programming in LabVIEW.

Programs in LabVIEW are called 'virtual instruments' (VIs). VIs always contain a front panel and a block diagram. The front panel acts as the user interface, while the block diagram contains the programming. Values in VIs are defined in nodes. Nodes are either constants, indicators or controls. Constants appear only in the block diagram, while controls and indicators provide tunnels between the front panel and the block diagram. Controls are values input in the front panel to be used in the block diagram, while indicators are used to display results from the block diagram on the front panel. Fig. 5.2 illustrates the front panel and block diagram of a very simple arithmetic operation. Any VI can be used as part of a larger architecture. VIs used as components are termed subVIs. A subVI will be represented as a symbol in the block diagram of the larger VI.

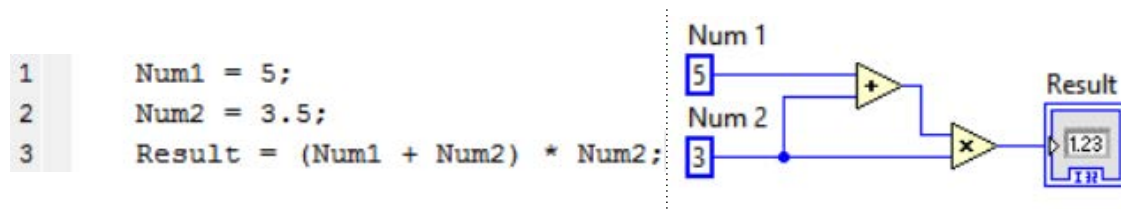[1]Laboratory Virtual Instrumentation Engineering Workbench

Figure 5.1: Text-based programming vs the graphical approach of LabVIEW. In LabVIEW programming elements are represented by symbols. Data flow is visualized by wires connecting said symbols. While the example is simple arithmetic, LabVIEW contains complex functions and data structures similar to those found in other programming languages.

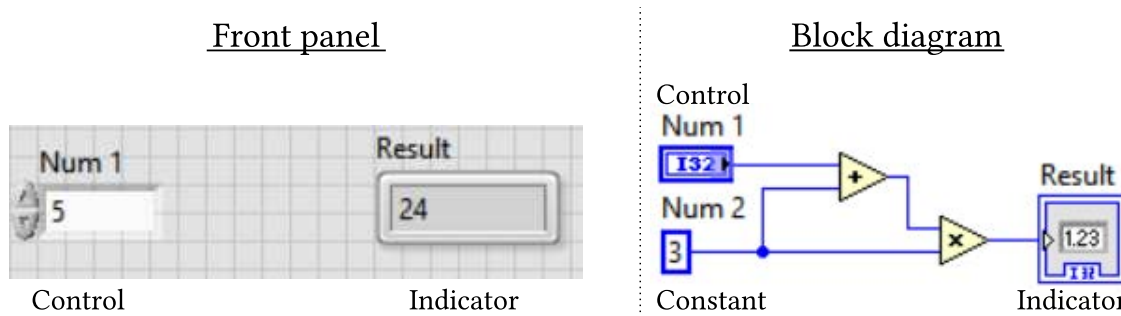When used as a subVI the controls make up the input, while the indicators are output. Proper use of subVIs prevents clutter and makes large architectures transparent.

Figure 5.2: Front panel and block diagram example. The front panel of a program allows for user input in controls, and displays outputs from the block diagram in indicators. The example takes a user input, (Num1), adds a constant (Num2) to it, and multiplies the sum with the constant. The final result is displayed in an indicator (Result) on the front panel.

A point in which LabVIEW differs greatly from text-based programming is execution timing. While text-based coding is rather linear, the order in which functions are performed in a VI is controlled by data flow. This means functions will run when all inputs are available. In Fig. 5.2, this means the multiply function will not execute before the addition function has run and passed on a value. No other factors affect the timing of functions, meaning functions which have no data interdependence can run in parallel if their inputs are available at the same time. Understanding data flow in block diagrams is thus crucial to creating a reliable program. Whereas the VI examples in Figs. 5.1 and 5.2 have very simple data flows, the final automation program needs a complex flow of data to achieve the desired functionalities.

5.2   Program development

The approach used to develop the automation program bears resemblance to the initial stages of a product development process. As such, the approach will be described accordingly, using terms

and methodology described in Ref. [22]. The first five steps in a product development process outlined there are applied here, in the extent possible. Accordingly, members of the Microfluidics Research Group will be termed users or customers henceforth. The steps are as follows; (*i*) identifying customer needs, (*ii*) establishing target specifications, (*iii*) generating product concepts, (*iv*) selecting product concept, and finally (*v*) testing product concepts.

5.2.1 Identifying customer needs

The most fundamental principle of a product is that it must satisfy a customer or user need. Needs can be explicitly stated by users or latent needs the users do not realize themselves. Some user needs are quite individual, but should be considered nonetheless.

Information of user needs are usually gathered using interviews, focus groups or by observing products in use. The user needs of the program were initially mapped by simply taking part in experiments and manufacture. As the program started taking shape and the users started realizing the capabilities of a LabVIEW program, new user needs were gathered by conversations with the users. While one should strive to uncover as many user needs as possible, not all needs are equally important, so the needs were ranked. Table 5.1, shows a list of uncovered user needs in chronological order.

Implicit user needs. The user needs marked in italic in the table indicate unspoken needs, expressed by yours truly. These are needs not specifically stated by users, but nonetheless recognized by developers. Unspoken needs can be either implicit or latent. The need '*The program must be robust*' is an example of an implicit need. While it isn't directly stated, it is clear that software is generally better when it is robust, i.e. it largely behaves in the same manner regardless of the input given. The remaining unspoken needs in Table 5.1 are latent needs. These are needs users have not thought of, but which developers regard as potential needs. In this specific case, the discovered latent needs could readily be discussed with the users, verifying that they would indeed prove useful.

5.2.2 Setting target specifications

User needs are quite objective and as such hard to measure. Therefore, it is necessary to translate the needs to a metric base in order to verify the user need is met. Abstract user needs may need more than a single metric to express them. Vice versa, a single target specification may be used to describe the satisfaction of more than one user need.

While it can be difficult to quantify user needs, metrics can often be set even for rather abstract statements with a little ingenuity. An abstract need such as a demand of intuitiveness may be approximately quantified as, 'all buttons must have tags indicating their function and current state'. While intuition is rather individual, the specification does however set a metric for the transparency of the program, and thus how easily the function is perceived. Note that this is a binary metric, which is entirely acceptable, and quite common for the program as most user needs regard the use of the program.

Table 5.1: User needs and their corresponding target specifications, ordered chronologically from first to last uncovered. Needs in *italic* indicate implicit needs.

Imp.	User need:	Target specification:	Metric
5	We need to control the flows	3 syringe pumps can be controlled at once	Instruments
5	We need to control field	A signal generator can be controlled	Instruments
4	We need to monitor the flow	A live feed from the SLR can be established	Binary
4	We need to record images and movies of the flow	The SLR can save images or recordings of the live feed	Instruments
4	*The program must be robust*	No possible user input causes program to crash	Binary
2	The IDTs must not overheat	Signal generator amplitude may not exceed 15 V	Voltage
2	The program must respond quickly	Response time must be below 100 µs	Time
		All inputs are matched by a response from the system	Binary
3	We need to quickly stop field and flow sometimes	A stop-button that consistently exits program properly is included	Binary
2	The program must be intuitive (or X will not use it)	Buttons have tags indicating their function and current state	Binary
		All input possibilities are visible in a single window	Pixel size
5	We need to be able to control instruments manually	Input values can be set freely - in manual mode	Input
4	Changing values mustn't be more difficult than now	All values are changable within no more than 3 interactions	Clicks
4	*Program must automate experiments*	A list of sets of instrument values can be input	Input
1	We want to have functionality to monitor the device	A camera observing the device can be controlled (Web camera)	Instruments
2	*Program must control oscilloscope*	An oscilloscope can be controlled	Instruments
2	*Program must have basic substrate QC capabilities*	A pseudo-network analysis can be performed	Instruments
4	*Program must systematize data acquisition*	Images are named according to their flow factors and the current date. Suffixes are added to doublet names	Binary
5	*The program may need to be expanded in the future*	New features must be easily implemented	Intangible

5.2.3 Generate product concepts

In the initial stages of development, the user needs to manually control the flow and to pause, and stop the program at any time were not uncovered. This can be achieved by two different approaches/concepts as illustrated in Fig. 5.3; a sequential structure and a state machine. Each structure has its benefits and disadvantages.
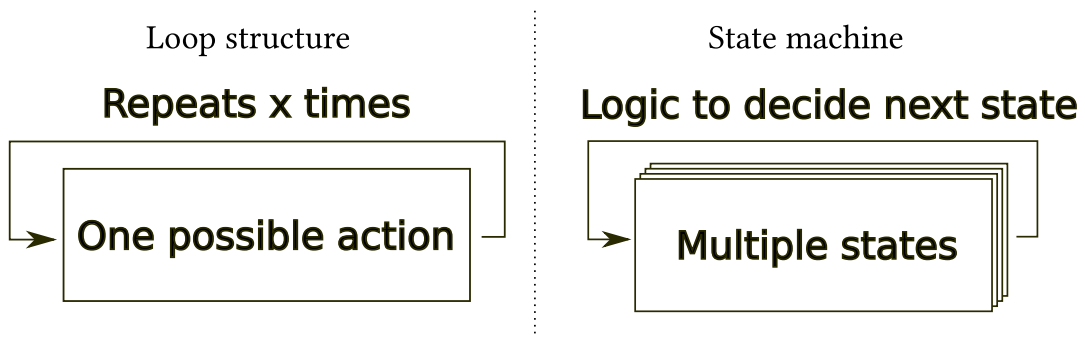

Figure 5.3: Program concepts in consideration. Sequential structures are a linear approach to coding, where a sequence of code snippets is repeated a number of times, e.g. once for each entry in an input file. A state machine is a looped structure, wherein several snippets of code (states) are defined, and a logic is implemented to choose which state to run each iteration. The choice between the two stuctures is a weighing of time to program vs scalability and responsiveness of the program.

Sequential structures are generally very simple. In the following, sequential structures are taken to mean inherently linear structures. This means little time goes into planning them, as the design options are quite limited. As the flow of data is always unambiguous, the functioning of a sequential structure can be inferred at a glance. Furthermore the linearity makes debugging very simple, as errors can only propagate in one direction.

The linearity of sequential structures is also their largest disadvantage. The linearity makes code hard to expand upon, and makes it hard to implement user reactions. Listing 5.1 illustrates the linearity with piece of pseudo-code for a sequential structure.

```
Repeat 100 times;
    Code snippet 1
    Code snippet 2
End repeat
```

Listing 5.1: Pseudo-code of sequential structure

State machines are built up on a simple principle. An initial state is run, a state selector (SSL) logic determines the next state to be run, that state is then run, the next state is determined, etc. State machines are in essence just sequential structures, where the snippet of code run can vary between each iteration, and no fixed number of iterations is set. The greatest strengths of a state machine is its responsiveness - as the state selection can easily be tied up on user input - and scalability. State machines can easily be expanded with new states, as long as the SSL is updated to reflect the new possible states. The layered structure within state machines can make them

rather hard to interpret. Furthermore the complex data flow between states makes debugging challenging, as it can be difficult to determine where errors arise. This holds particularly true when insufficient planning has been done prior to programming the state machine. A far stricter protocol to error handling and data guidance will generally be necessary for state machines than sequential structures. Listing 5.1 shows a piece of pseudo-code for a case structure, wherein two states are run alternately, until terminated by a user input. This is of course a very simplified case. In reality, the case selector logic will be far more complex, and the states more numerous.

```
Next state; State 1
Repeat until condition=1;
  Select state;
    State 1
      Code snippet 1, Next State; State 2
    State 2
      Code snippet 2, Next state; State 1
    State 3
      Condition = 1
  End select
  If 'Stop pressed'
    Next state; State 3
  End If
End repeat
```

Listing 5.2: Pseudo-code of a state machine containing 3 states. State machine will not terminate before 'Stop' is pressed

5.2.4   Selecting and testing product concept

Concept testing and selection involves selecting and comparing a number of concepts. The success of a concept is measured in how well it meets target specifications in Table 5.1. Target specification can be categorized in general groups, as shown in Table 5.2. To compare the two concepts, a comparison of how well they fare in each specification group is made.

Instrument control: Incidentally, the most prominent target specifications - handling instrumentation - are some of the easiest to satisfy and test. The instruments controlled in the program are all connected *via* USB-cables, bar the SLR camera which is connected *via* a IEEE 1394 (firewire) connection. Instrument connected to a PC, can be assigned custom VISA[2] resource names. The port settings necessary for the PC and instrument to communicate are automatically attached to the resource name. Thus instrument connections in LabVIEW are very simple once a VISA resource name has been assigned. Fig. 5.4 shows a VI to control a syringe pump, using its VISA resource name.

Connecting to the signal generator, oscilloscope and web camera follow the same general process. Instrument connectivity procedure is the same regardless of structure used. However, a state machine is better suited at connecting and disconnecting instruments on the fly.

Run mode: The concepts must enable two possible run modes; automated test sequences and manual control. The two modes have a common framework - as the VIs used are largely the same - with the primary difference being the user input mode. In order to obtain two run modes

---

[2]Virtual Instrument Software Architecture

Table 5.2: Target specifications grouping. Specifications

Target specification:	Specification group
3 syringe pumps can be controlled at once	Instrument control
A signal generator can be controlled	Instrument control
A camera observing the device can be controlled (Web camera)	Instrument control
An oscilloscope can be controlled	Instrument control
Signal generator amplitude may not exceed 15 V	Instrument control
Input values can be set freely when in manual	Run mode
A list of sets of instrument values can be input	Run mode
A live feed from the SLR can be established	Live feed
The SLR can save images or recordings of the live feed	Live feed
A pseudo-network analysis can be performed	Data acquisition
Images are named according to their flow factors and the current date. Suffixes are added to doublet names	Data acquisition
No possible user input causes program to crash	Program robustness
A stop-button that consistently exits program properly is included	Program robustness
Response time must be below 100 μs	User responsiveness
All inputs are matched by a response from the system	User friendliness
All inputs are matched by a response from the system	User friendliness
All values are changable within no more than 3 interactions	User friendliness
Buttons have tags indicating their function and current state	User friendliness
All input possibilities are visible in a single window	User friendliness
New features must be easily implemented	Program scalability

using sequential structures, two separate programs must be created, while a state machine can incorporate both modes. Automated tests are run by inputting a file with a list of sets of flow and field values. The program sets the instrument values according to the first input set of values, allows a short time for the system to relax, takes a picture of the channel, and continues to the next set of values. This is automatically performed for all value sets in the input file. Once the end of the list is reached, the automated run is complete.

Running the program in manual mode essentially transforms the program to a control center for the instruments. When running in this mode, users have complete control of flow and field factors, and can start recording images and movies at any time. When running manual mode the program perpetually compares the values it last passed to the instruments, to the ones the user has input. When the values differ, the new user input values are passed to the instruments. The program leaves manual mode when the user specifically selects to do so.
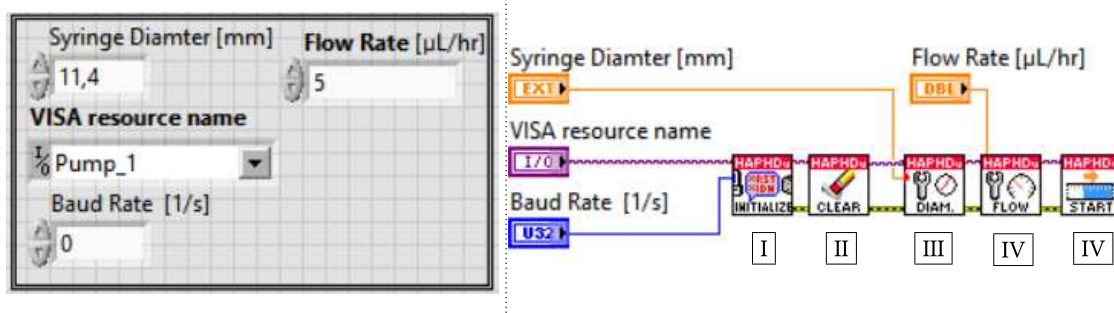
Figure 5.4: VI to control syringe pump. The VI uses 4 controls and contains 5 subVIs, each containing instrument routines. (I) Using the VISA resource name, a connection is established between the PC and the syringe pump. (II) The syringe pump settings are then reset. (III) The diameter of the used syringe is set (IV) and so it the the desired flow rate (V) Finally, the pump is started.

A simplified flow chart of manual and automated run modes in a state machine is shown in Fig. 5.5. For clarity the flow chart shown is rather simplified. In reality, a far more complex SSL is implemented. This causes interconnectivity between practically all states in the state machine, which will not be discussed here. The reader is referred to the appendix for a description of the program functionality.

Live feed: A live feed of the channel flow can be established by connecting to the SLR, capturing an image through it and displaying it on the front panel. When this is performed at a sufficiently high refresh rate, the images will be perceived as a fluid live stream. This may be realized in both sequential structures and state machines, although timing is more easily controlled in a state machine.

Data acquisition: An approximated network analysis can be implemented in parallel with a sequence structure or directly implemented in a state machine. However, as the network analysis requires a different set-up than the manual and automatic run mode, it makes little sense to implement directly in a state machine. Thus, the network analysis should be implemented as a separate program, regardless of the chosen concept. Automatic naming is equally simple to include in both concepts, as it is simply a matter of creating a proper subVI. Due to its importance in automating the data acquisition process, it is described here. In order for recorded images to be useful a consistent, transparent naming convention is required. Without consistency an automated data analysis cannot possibly be carried out. Transparency in naming is important to effectively convey the conditions of an image. Without knowledge of the flow and field factors - and preferably the particle solutions used - images merely illustrate a possible particle separation scenario. Thus, a image naming system was made to ensure that all names contain this information. The format for the images was requested by the users to be

```
'[Pump i Prefix][Pump i flow rate]ulh\_[Field frequency]\_MHz\_[Field amplitude
    ]dbm\_Field\_[on\/off]\_[doublet suffix].[file format]'
```

where i = 1,2,3, depending on the flow set-up. Fig. 5.6 shows part of the subVI naming images taken.
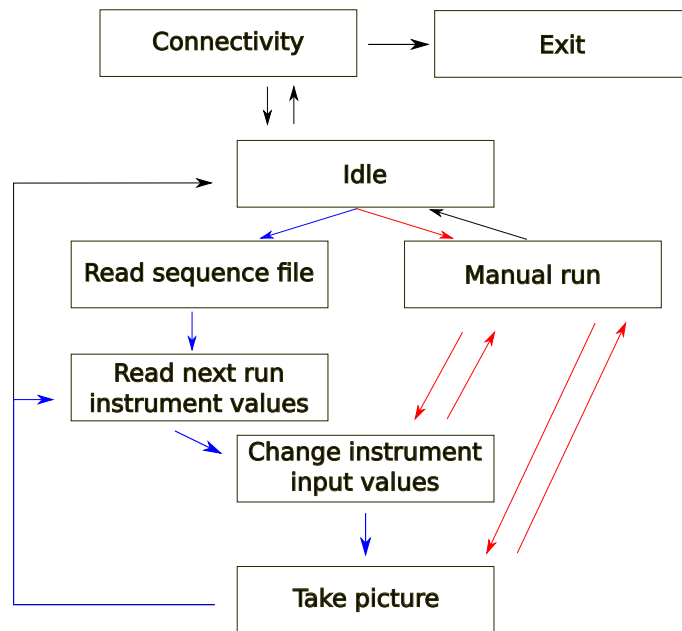
Figure 5.5: Flow chart of the state machine solution to alternate run modes. Illustration of principle flow chart of the state machine employed. Each box represents a state of the state machine while the lines represent the state selector logic. The colour coding illustrates. steps; in an automated sequence test (blue), when running manually (red), shared by both routines (magenta), and to initialize and exit the program (black). Note, the state selector logic shown is a rather simplified version, as the real one would obfuscate the flow chart entirely.

Program robustness: In order for a product to be robust, it must be insensitive to variations in run conditions. In the context of the program robustness means that regardless of user input combinations performance must be consistent. As actual users interaction may differ greatly from the intended one, it can be difficult to predict robustness breaches. Sequential structures are invariably more prone to breaches of robustness, and require a larger amount of debugging and error checking, as more input possibilities are available and data flow is non-linear, unlike sequential structures.

User responsiveness: With regards to timing, state machines are far superior to sequential structures. While a sequential structure can include a point in the sequence wherein user input is polled for, a state machine can continually poll for user input between each state, and react accordingly. User inputs can thus be handled much more quickly in a state machine, than in a sequential structure.

User friendliness: While user input possibilities are limited in a sequential structure, the user interface is independent of the concept chosen.

Scalability: State machines are in their nature very scalable. New functionality is simple added by implementing it as a new state containing while updating the SSL accordingly. Sequential structures can only really scale with very specific functions.
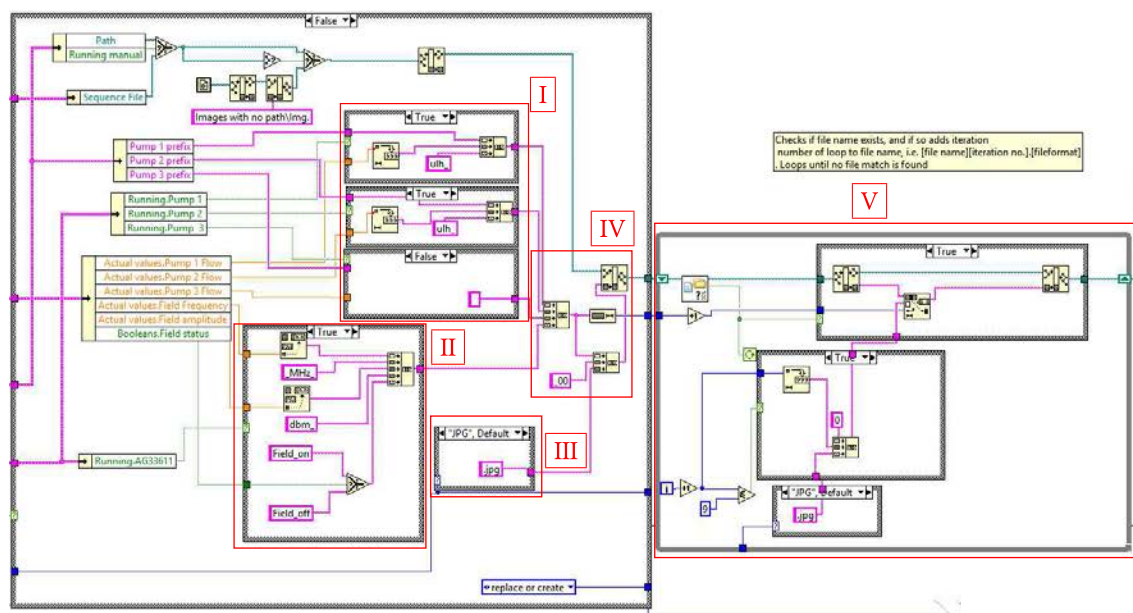
Figure 5.6: SubVI illustrating image naming operation. The image naming is a series of string and path operations; (I) For each currently active pump, flow rates and customizable prefixes, (e.g. contents in syringes) are appended. (II) A suffix describing signal generator is added to the resulting string, and (III) the file extension concludes the name. (IV) The path of the image is added, and (V) after verifying an image with that name does not exist already, the image is saved. If an image with the same name does exist, an integer suffix is added to the end of the name and the file is attempted saved. This is continued until an available name is found. The operation exemplifies well why the program in its entirety will not be presented in the thesis. Even simple tasks take up copious amounts of space. It is however, available to view the code as a .html-file at http://tinyurl.com/hsao8xm.

5.2.5 Final product concept

The categories outlined above vary greatly in importance, with scalability and robustness being particularly important. The choice of concept was came down to weighing the possibility of future expansions in a state machine against ease of programming and debugging in sequential structures. In the end, functionality outweighed the aspect of programming difficulties. Had the time frame for the programming been shorter, the sequential structure approach would likely have been chosen, as a simple, running program is better than a complex, non-functioning program after all.

The programming itself, i.e. the block diagrams will not be shown here. Fig. 5.6 shows part of a subVI, illustrating why the LabVIEW code is not included in the main thesis, as even fairly simple procedures take up a lot of space in graphical programming. For a view of the entire program, refer to the scrollable, zoom-able file 'Main.html' in the shared dropbox-folder, linked to here: http://tinyurl.com/hsao8xm

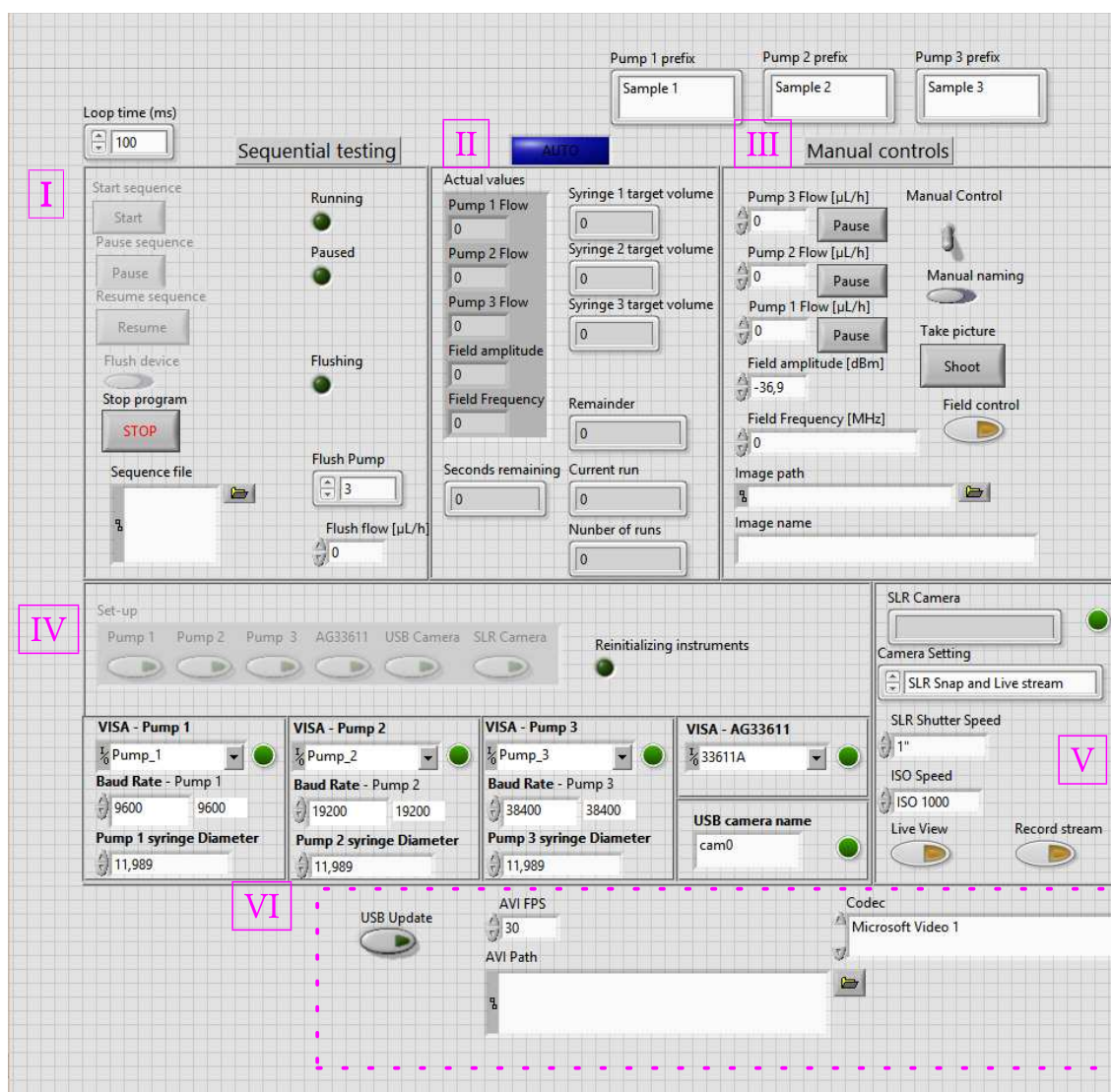Note it may be necessary to download the folder in its entirety to view Main.html

Figure 5.7: Automation program front panel. Controls and indicators on the front panel are sectioned based on their functionality. (I) The controls for running the program in automation mode include buttons to start, pause and resume the automation sequence, and buttons to flush device or stop program entirely. The flush pump, i.e. the pump containing sheath fluid is also designated here. (II) The indicator section shows the current flow and field factors, the volume necessary in syringes in pumps 1 to 3 to carry out entire sequence, and a status in the current automation sequence. (III) The section for manual run mode, contains the necessary inputs to control field and flow factors, and to capture and save pictures. Strings to be used as prefices in the naming convention are entered here as well. (IV) In the instrumentation section users select the instruments needed for the current run mode. The section also contains connection options, which should only be changed if new instruments are introduced. (V) In the view section, options regarding live view, live capture, camera settings and the images shown on displays 1 and 2 are selected. (VI) The video section determines the codec, frame rate and path of video recorded.
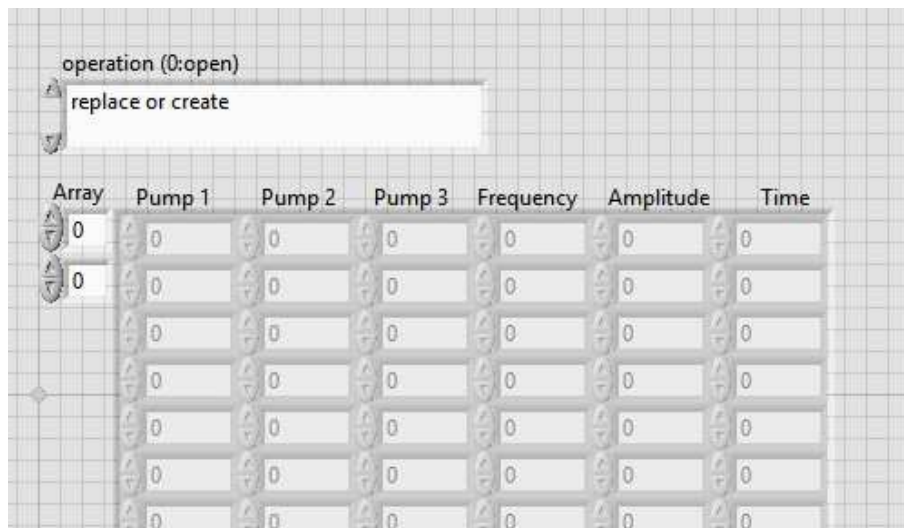
5.3   Supplemental programs

Two quite simple programs were developed to use in conjunction with the automation program; a program to write .csv files to use as input for the automation program, and a pseudo network analyzer.

While input files can be written using any program that saves in .csv format, a program was made to enable users to create files of the proper format. Users need only input values into the program, which then handles formatting.

The pseudo network analyzer was made to quality control substrate chips. The network analysis described in Section 4.2.5 requires a vector network analyzer, which is a rather expensive piece of equipment. The group does not own one such, but was allowed to use one to test each design. In order to be able to perform something akin to network analysis using the instruments at hand, a program with a similar function was made. The program makes use of signal generator and oscilloscope to obtain approximate values of the transmittance coefficients. An alternating current is applied to one IDT (port 1) using the signal generator and the corresponding output at the other IDT (port 2) is measured using the oscilloscope. By sweeping through a range of frequencies, a plot of the transmittance coefficient $S_{2,1}$ is determined, while switching the connections yields $S_{1,2}$.

Fig. 5.8 shows the front panel of the supplemental programs.

(a)
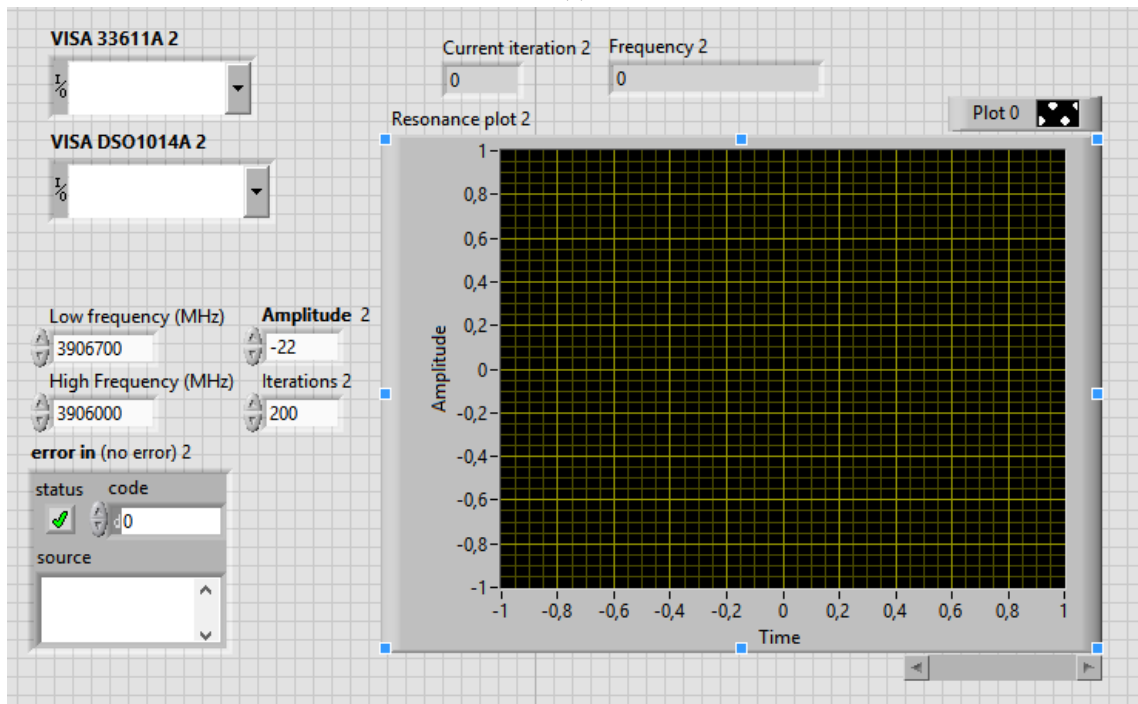
(b)

Figure 5.8: Supplemental LabVIEW tools. Programs to (a) create input .csv-files for the automation programs and (b) run a simple version of a network analysis. The .csv-file maker was developed to ensure no other programs than LabVIEW are necessary to run experiments, while the network analyser was made to provide substrate chip quality control. While providing lower precision and lacking the ability to measure reflection coefficients, the program performs analysis on-site on instruments costing a fraction of a vector network analyser.

Chapter 6

Numerical and experimental results

This chapter will examine the validity of wall boundary conditions as simplifications of modelled interactions between solid and fluid domains. The validity will be examined as a function of solid dimensions, at and off resonance. Due to the heavy computational needs of the numeric model, each simulation is very time-consuming so only a select few simulations have been run thus far.

Also presented in this chapter are a results from a network analysis performed on a new substrate chip design at the Microfluidics Research Group headed by Bjørn T. Stokke, at NTNU and a showcase of how future experimental data can be used to verify the numeric model.

6.1 Comparison methods

In order to consistently compare results found using

The numerical basis for comparing results are the first order acoustic fields. To recapitulate, the physical value of field s, at a time t, is found as the real part of the complex field value

$$s_{\text{physical}}(\boldsymbol{r}, t) = \Re\left[p(\boldsymbol{r}) \cdot e^{-\mathrm{i}\omega t_0}\right]. \tag{2.1}$$

As such, the complex field value s at any time, contains the current physical value $\Re(s)$, as well as the time-dependence of the value $\Im(s)$. To compare acoustic fields, the real part at a given time is thus not representative. Two identical fields may take on different appearances due to a phase difference between them. Vice versa, two fields may bear resemblance at one instant, while being dissimilar at another. A more representative comparison can be made using the absolute value of a field

$$\|s(\boldsymbol{r}, t)\| = \sqrt{\Re\left[p(\boldsymbol{r}) \cdot e^{-\mathrm{i}\omega t_0}\right]^2 + \Im\left[p(\boldsymbol{r}) \cdot e^{-\mathrm{i}\omega t_0}\right]^2}. \tag{6.1}$$

The absolute value of a field value in a given point indicates the maximum value the point reaches during a harmonic cycle, i.e. the amplitude of field value oscillations. Fig. 6.1 exemplifies the difference in comparing instantenous field values and comparing absolute values of fields.

Plots of pressure and velocity fields provide information on physically relatable quantities. In experiments, however, the observed variable is the acoustic radiation force. Thus we will henceforth solely consider plots of the acoustic radiation force - explained in Section 2.6 - on a
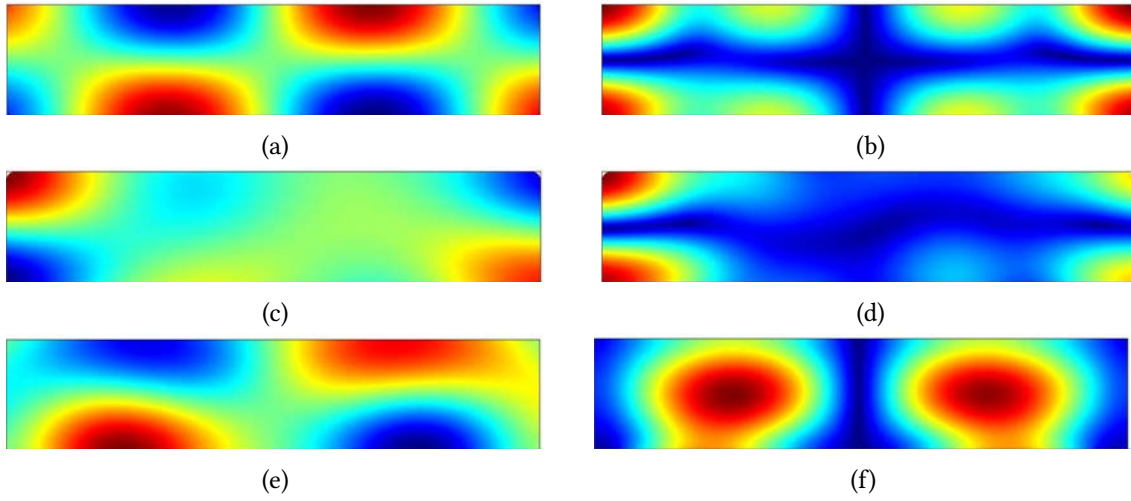
Figure 6.1: Instantaneous v absolute values. Instantaneous and absolute values of first order pressure fields p. When comparing instantaneous values, the hard (a) and lossy wall (e) conditions appear similar while field of the modelled glass (c) is out of phase and stands out. The absolute values, however, reveal the similarity between the hard case (b) and the modelled glass (d). The lossy wall condition (f) is clearly different from the two. In fact, the lossy wall condition yields a travelling pressure field, i.e. one in which the features translate in the channel, while the hard wall and modelled glass yield fields that are stationary, but oscillating.

reference particle to provide a comparison basis with regards to acoustophoresis. Throughout the result section thesis, the reference particle will be a $20\,\mu\mathrm{m}$ polystyrene bead unless otherwise specified. This is a commonly used particle size and material in microfluidic experiments. To illustrate that the radiation force depends on both pressure and velocity magnitude gradients Fig. 6.2 shows contour plots of these alongside force field plots.

6.2   Boundary condition validity

The four study cases introduced in Section 3.3.5 are used to test boundary condition validity; (*i*) the hard wall boundary condition, (*ii*) the lossy wall boundary condition, (*iii*) coupled fluid and glass domains and (*iv*) coupled fluid and PDMS domains. Hard wall validity is tested by comparison of acoustic fields from cases (*i*) and (*iii*), while lossy wall condition validity is tested using cases (*ii*) and (*iv*). The wall conditions are tested by comparing the acoustic fields found using boundary conditions to three full model simulations. The fluid domain dimensions and actuation parameters are kept constant in all four simulations, while three different solid domain dimensions are used, as shown in Table 6.1.

6.2.1   Hard Wall condition

The hard wall boundary condition is compared to modelling the surrounding glass. The resulting pressure and force fields are shown in Fig. 6.3. Note the solid domains are not shown, as only
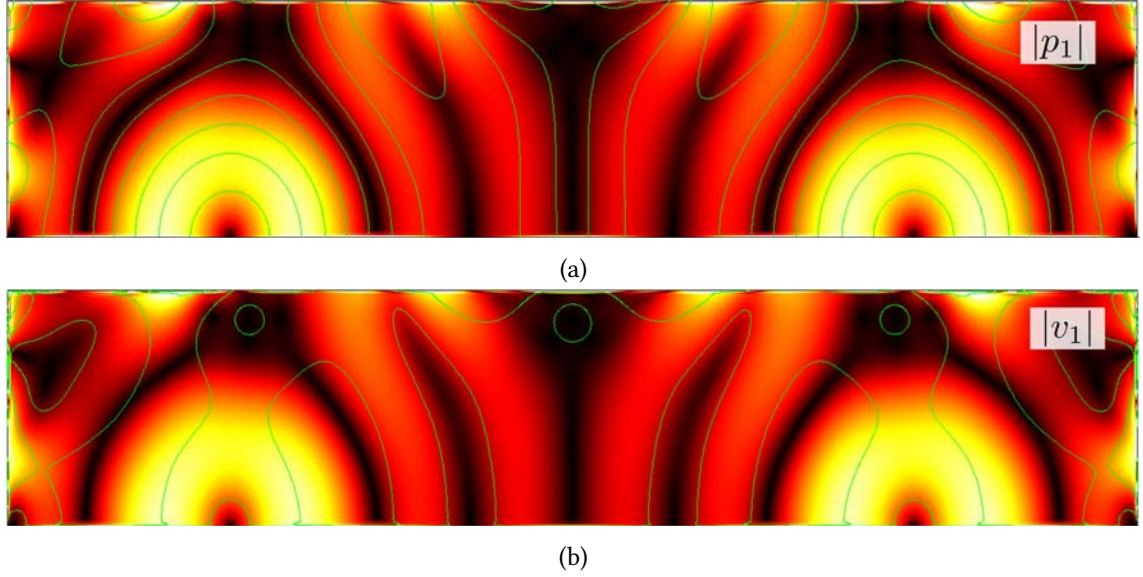
(a)

(b)

Figure 6.2: Radiation force dependencies. Surface plots of the radiation force with contour plots of (a) the absolute pressure and (b) the absolute velocity magnitude added to them. The plots illustrate that the radiation force contains features determined by both fields. Features in (a) along which contour and surface plots show coherence, are primarily determined by pressure gradients, while the same holds true in (b) for velocity magnitude gradients.

the acoustic fields in the fluid are of interest in acoustophoresis. The figure shows that the hard wall condition does not approximate thin borosilicate glass walls at all. Intuitively this makes sense, as the hard wall condition is based on the assumption, that the wall remains completely still. The thinner a wall becomes, the more likely it is to yield to the fluid pressure, i.e. deviate from the assumption. As thickness increases, the modelled solutions more closely resemble the shape of hard wall results, but even at $1.2\,\mathrm{mm}$ the resulting fields still show some differences.

To examine hard wall validity at resonance, the same system is simulated at a resonant frequency estimated in Section 3.4.3 to be $1.24\,\mathrm{MHz}$. The resulting force fields are shown in Fig. 6.4.

While Fig. 6.3 illustrates that the hard wall and full model results do not yield the same acoustic fields, Fig. 6.5 illustrates why. The hard wall condition can be rewritten to displacement form, due to the fluid-solid coupling

$$\boldsymbol{n} \cdot \partial_t \boldsymbol{u}_{\mathrm{s}} = \boldsymbol{n} \cdot \boldsymbol{v}_1 = 0\,, \tag{2.16b}$$

i.e. the fluid is only actuated at the piezo-solid interface when applying the hard wall. In the full model, however, the entire solid structure moves, meaning the solid-fluid interface moves as well. The fluid thus experiences conditions far from the approximation of the hard wall. Fig. 6.5 shows the displacement in the z-direction along the top fluid-solid interface divided by the SAW-displacement u_0. Notice, that the maximum displacements of the thin glass structure exceeds four times the displacement along the solid-piezo interface, indicating that the solid-liquid system has resonant frequencies. This explains quite well, why Fig. 6.3a is so different from Fig. 6.3b, as the most dominant actuation is actually from the solid structure.

Table 6.1: Domain dimensions and actuation parameters used in validation tests.

	Width	**Height:**
Fluid domain	600 μm	125 μm
Model 1 solid domain	660 μm	185 μm
Model 2 solid domain	1200 μm	725 μm
Model 3 solid domain	2100 μm	1625 μm
Actuation parameters:	$f_{\mathrm{SAW}} = 6.65\,\mathrm{MHz}$	$\lambda_{\mathrm{SAW}} = 600\,\mu\mathrm{m}$
Resonant actuation parameters:	$f_{\mathrm{SAW}} = 1.24\,\mathrm{MHz}$	$\lambda_{\mathrm{SAW}} = 600\,\mu\mathrm{m}$
Glass mechanical parameters:	$c_{\mathrm{L,g}} = 5591\,\mathrm{m\,s^{-1}}$	$c_{\mathrm{T,g}} = 3424\,\mathrm{m\,s^{-1}}$
PDMS mechanical parameters:	$c_{\mathrm{L,g}} = 1030\,\mathrm{m\,s^{-1}}$	$c_{\mathrm{T,P}} = 400\,\mathrm{m\,s^{-1}}$

When actuated at an eigenfrequency of the fluid, the hard wall appears to be a much better approximation. This makes sense, as the eigenmode pressure distribution is largely independent of actuation, as discussed in Ref. [20]. As long as the domain is symmetrically actuated at a resonant frequency, the eigenmode will settle in.
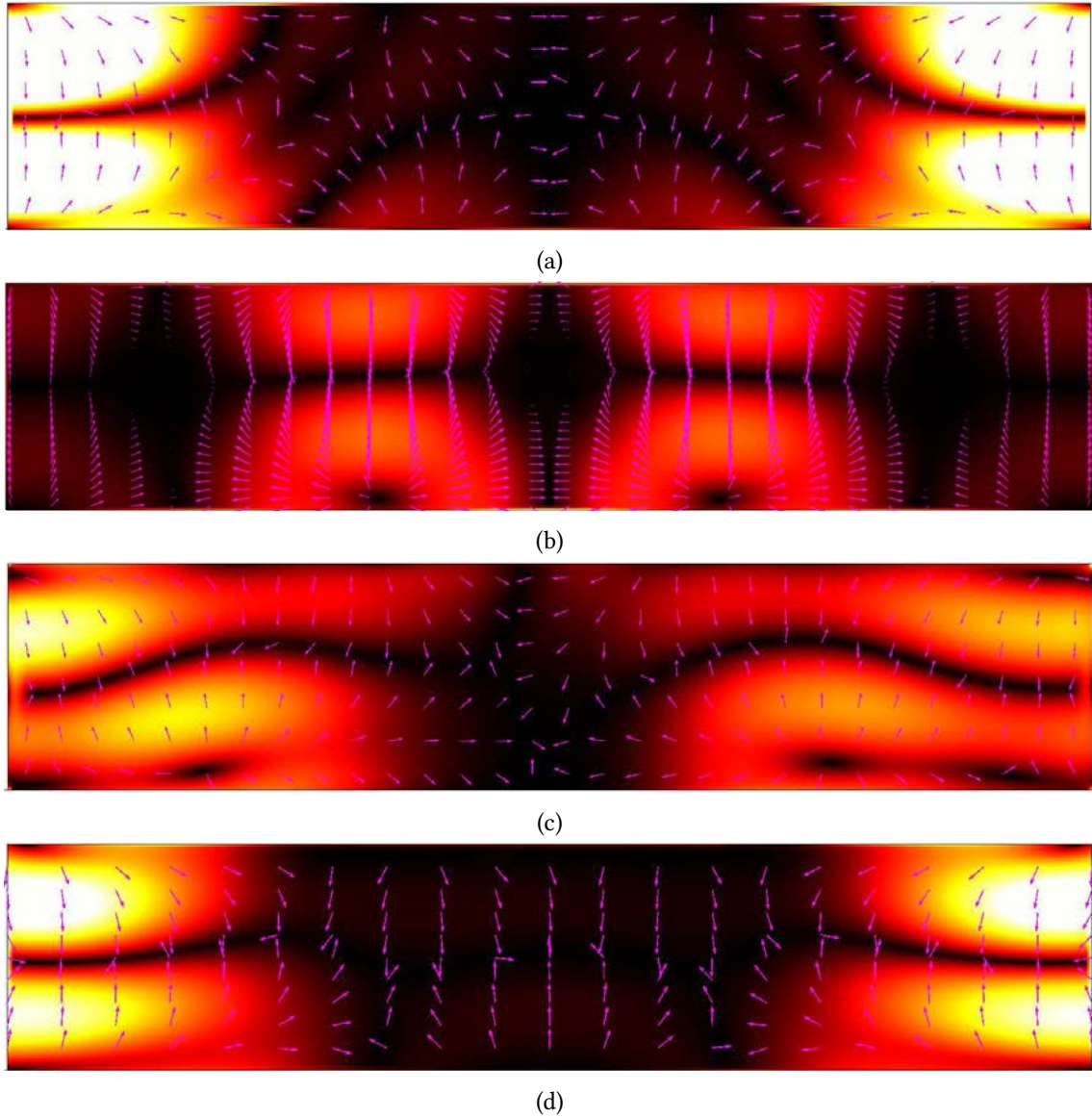
Figure 6.3: Hard wall thickness dependence. The hard wall radiation force (a), is compared to force fields (b) through (d), of a full model with varying glass thickness w_{wall}; (b) $w_{\text{wall}} = 60\,\mu\text{m}$, (c) $w_{\text{wall}} = 600\,\mu\text{m}$, (d) $w_{\text{wall}} = 1500\,\mu\text{m}$. All simulations are actuated at $6.65\,\text{MHz}$. For small thicknesses, walls will yield to fluid pressure, making the hard wall boundary condition a poor approximation. With increasing thickness, the simulations seem to approach the hard wall solution, to some degree.

(a)

(b)

(c)

(d)
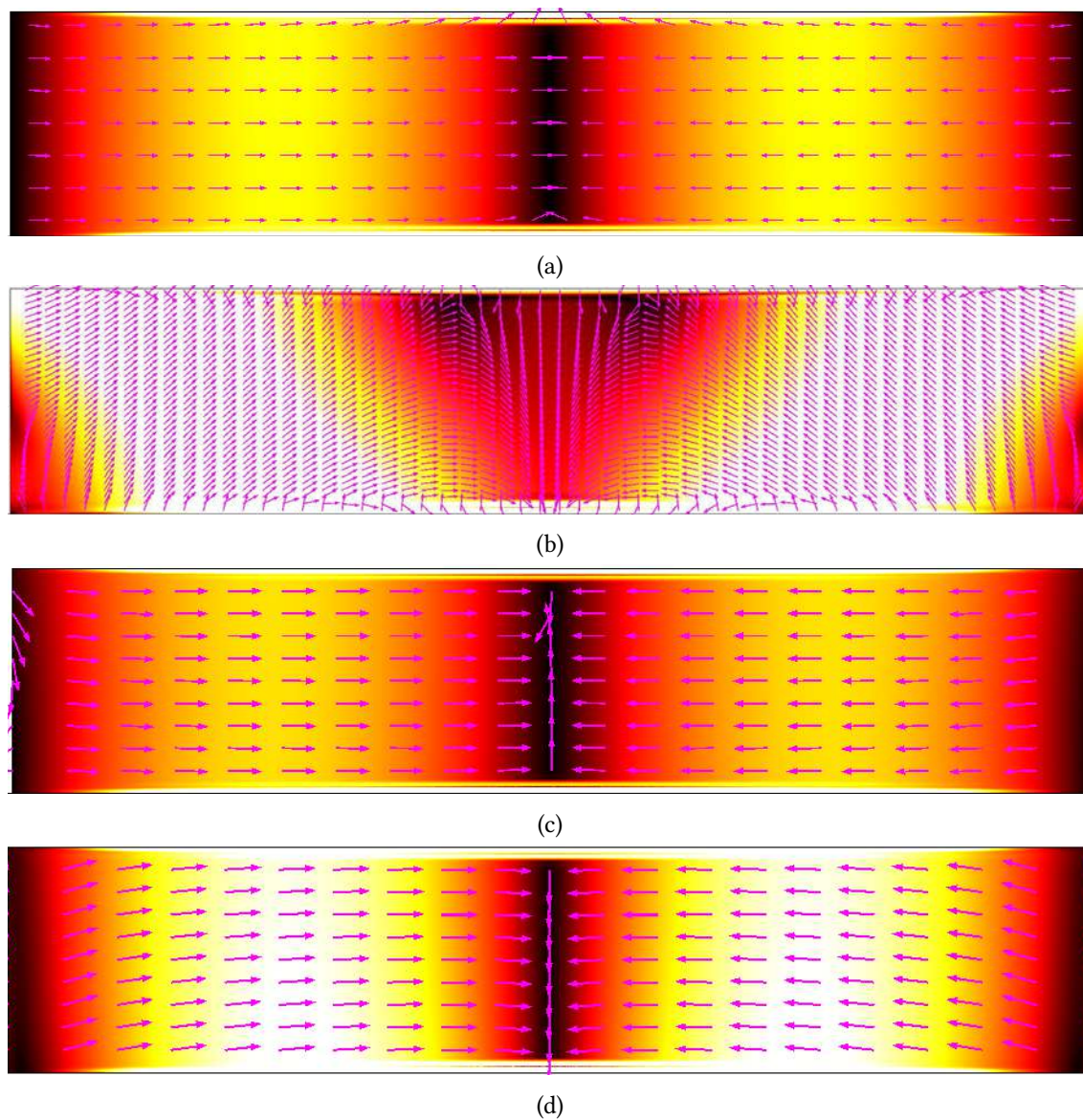
Figure 6.4: Hard wall thickness dependence at resonance. The comparison made in Fig. 6.3 is repeated, but actuated at a resonant frequency of an ideal water-filled rectangle with the dimensions of the fluid domain used in simulations. The resonance in the fluid domain may seem to make the hard wall a better approximation, as the thin case faintly resembles the hard wall condition, while the other two cases are very similar. However, the values vary greatly between the hard wall condition and the simulated cases, ranging from $600\,\mathrm{pN}$ when using the hard wall condition to $50\,\mathrm{pN}$ to $60\,\mathrm{pN}$. The hard wall approximation is thus only a good approximation with regards to the geometries of the radiation force field, but not the actual values.
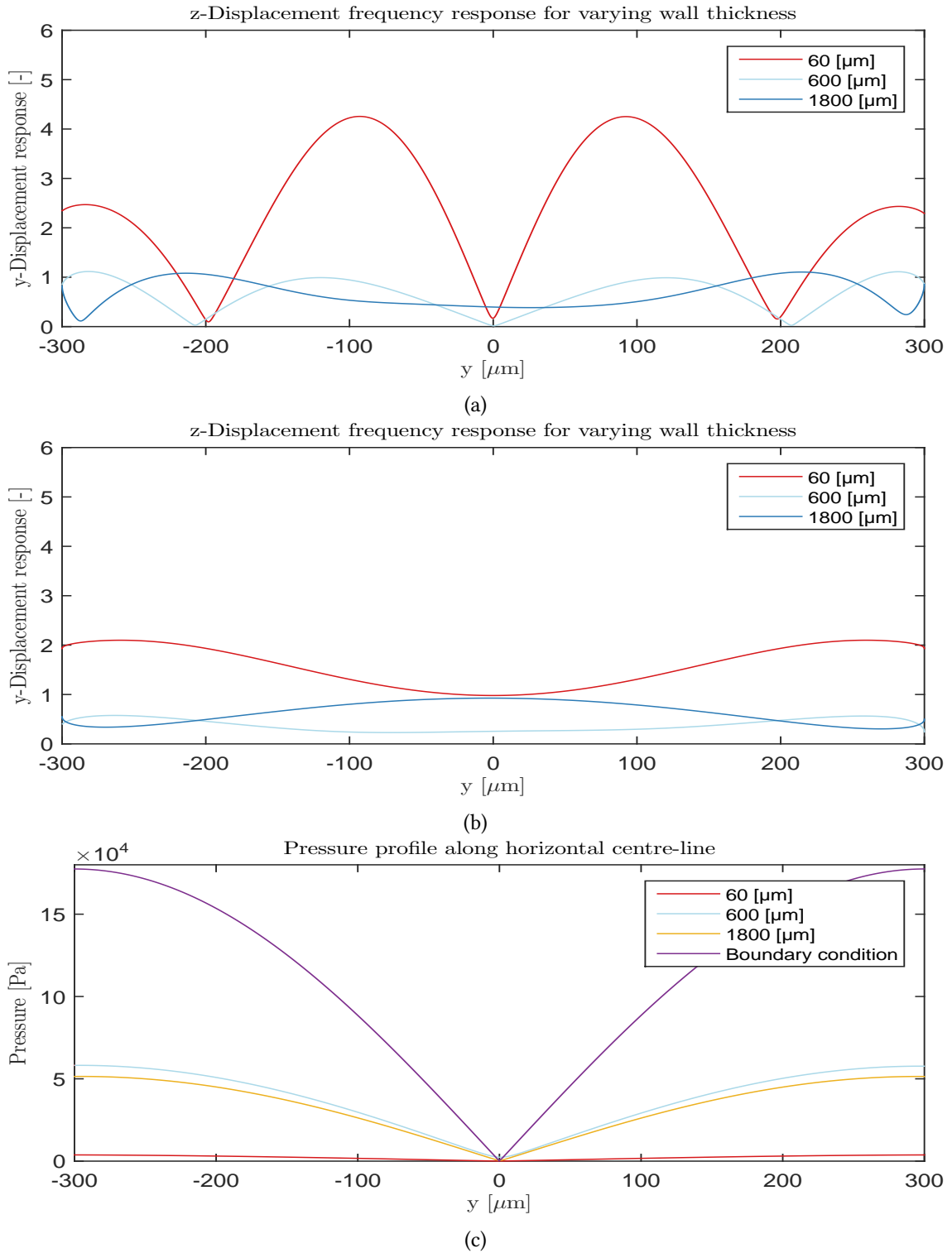
(a)

(b)

(c)

Figure 6.5: Displacement and pressure frequency responses of the solid. The displacements along the top of the fluid domain divided by the displacement of the applied SSAW, at (a) the actuation frequency of Ref. [1] and (b) a resonant frequency $f_{1,0}$. In both cases, the case of thin solid material has a response above unity, meaning the largest actuation of the system is in fact not the SSAW. This amplification of the displacement is indicative of a resonant frequency of the solid-liquid system. (c) shows the pressure profile along the horizontal centre-line of the fluid domain when actuated at $1.24\,\text{MHz}$. The immense difference in values, show that while the hard wall condition may approximate the appearance of acoustic fields well, it does not approximate the value.

6.2.2   Lossy Wall condition

The lossy wall condition employed by Ref. [1] is subjected to the same investigation as the hard wall condition, by comparing its results to those of models including PDMS domains of various sizes. Regardless of PDMS thickness, the solutions do not seem to converge towards any given solution, but rather depends highly on material thickness.

As with the hard wall, the simulations are repeated at a resonant frequency of an ideal rectangular fluid domain. The lossy wall and PDMS result bear no resemblance to the hard wall resonant response though, or to each other.

While the large differences in force fields seem unreasonable, the model has been verified to converge, to satisfy boundary conditions and to yield results similar to those found in the literature. In order to verify that the results from PDMS simulations are indeed correct, experimental validation will be necessary.

The lossy wall condition is predicated upon estimating the movement of the solid wall, based on the pressure within the fluid and the ratio between the acoustic impedances of the fluid and the solid. As with the hard wall condition, it does not take into account, that the solid may be moving, due to an exterior actuation. It also fails to take into account, that a pressure acting normally on a solid will not necessarily only affect the solid in the normal direction. If the solid is compressed in one direction, it will expand in another if it has a non-zero Poisson's ratio. In Fig. 6.8 the velocity of the upper fluid-solid interface is plotted along with the velocity imposed using the lossy wall condition for varying material widths, clearly showing that lossy wall does not approximate the solid motion along the interface.
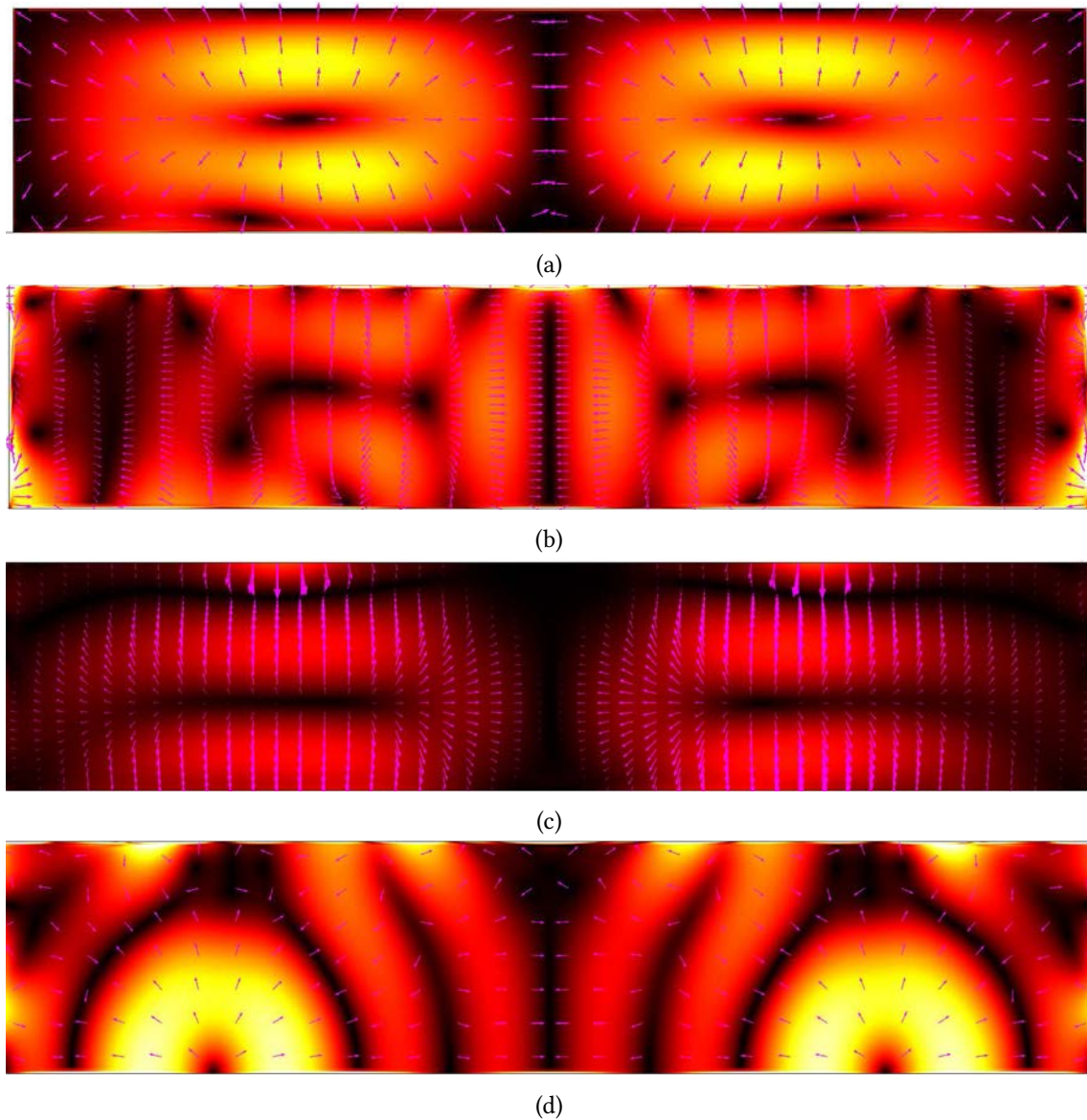
(a)

(b)

(c)

(d)

Figure 6.6: Lossy wall thickness dependence. The lossy wall radiation force magnitude (e), is compared to the force fields, of a full model with varying PDMS thickness w_{wall}; (b) $w_{\mathrm{wall}} = 60\,\mu\mathrm{m}$, (c) $w_{\mathrm{wall}} = 180\,\mu\mathrm{m}$, (d) $w_{\mathrm{wall}} = 600\,\mu\mathrm{m}$. The force fields seem to depend entirely on the width of the material. Regardless of material thickness, however, a pressure node is present along the vertical centre-line - a feature also found using the lossy wall condition. Interestingly, the lossy wall solution somewhat resembles the solution for $w_{\mathrm{wall}} = 180\,\mu\mathrm{m}$, but this seems purely coincidental.
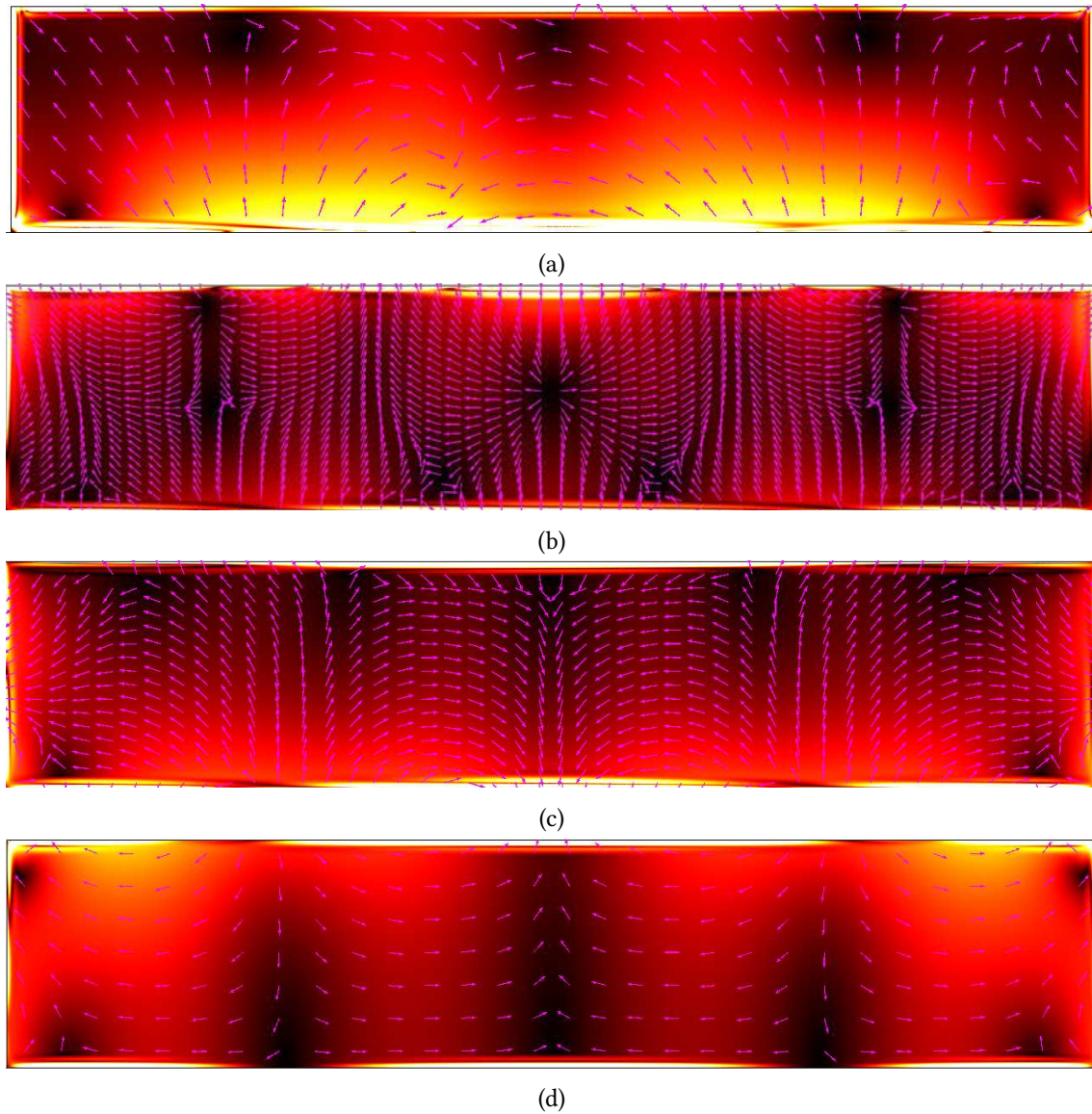
(a)

(b)

(c)

(d)

Figure 6.7: Lossy wall thickness dependence at resonance. The comparison made in Fig. 6.6 is repeated, but actuated at a resonant frequency of an ideal water-filled rectangle with the dimensions of the fluid domain used in simulations. As in Fig. 6.6, the PDMS shows no clear convergence, and radiation force fields differ substantially, even though changes in size are quite small.
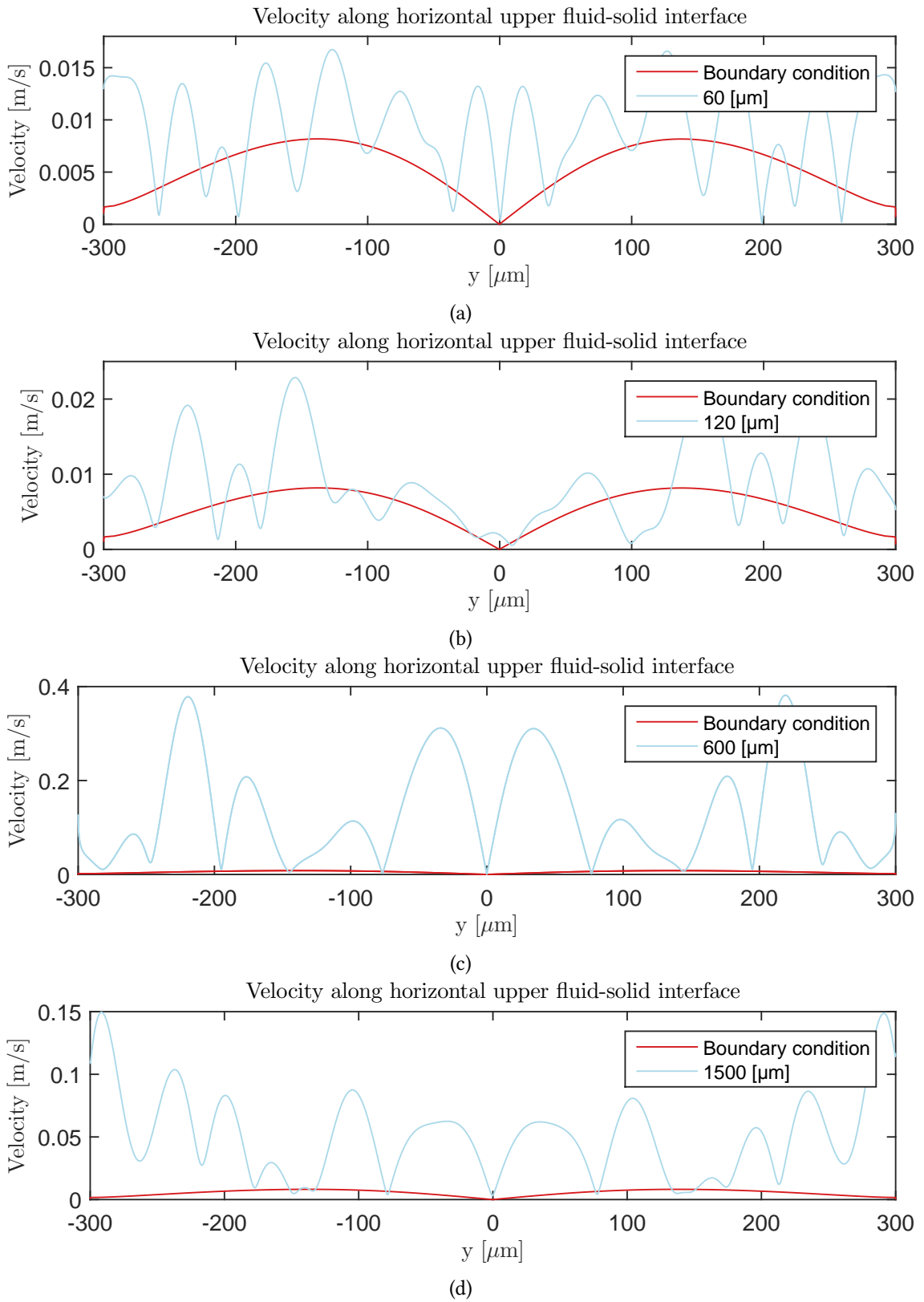
Figure 6.8: Imposed boundary condition versus actual condition for various PDMS widths. It is clear that the lossy wall imposes conditions quite different from the ones found when modelling the surrounding PDMS. No apparent pattern is seen with regards to the velocity as function of width.

6.3   Network analysis

The network analysis module programmed in LabVIEW allows users to perform an approximate network analysis on each IDT substrate made. This is beneficial to quickly check a chip for irregularities. While the vector network analysis instrument provides more comprehensible information of scattering parameters, it is only available on occasions and is rather far from the testing facilities. Fig. 6.9 shows a comparison between transmittance coefficients calculated using the program, to those found using a vector network analyser. While $S_{2,1}$ is too low at resonance, and $S_{1,2}$ is too high off resonance, the resonant frequencies can still be estimated based on their course.
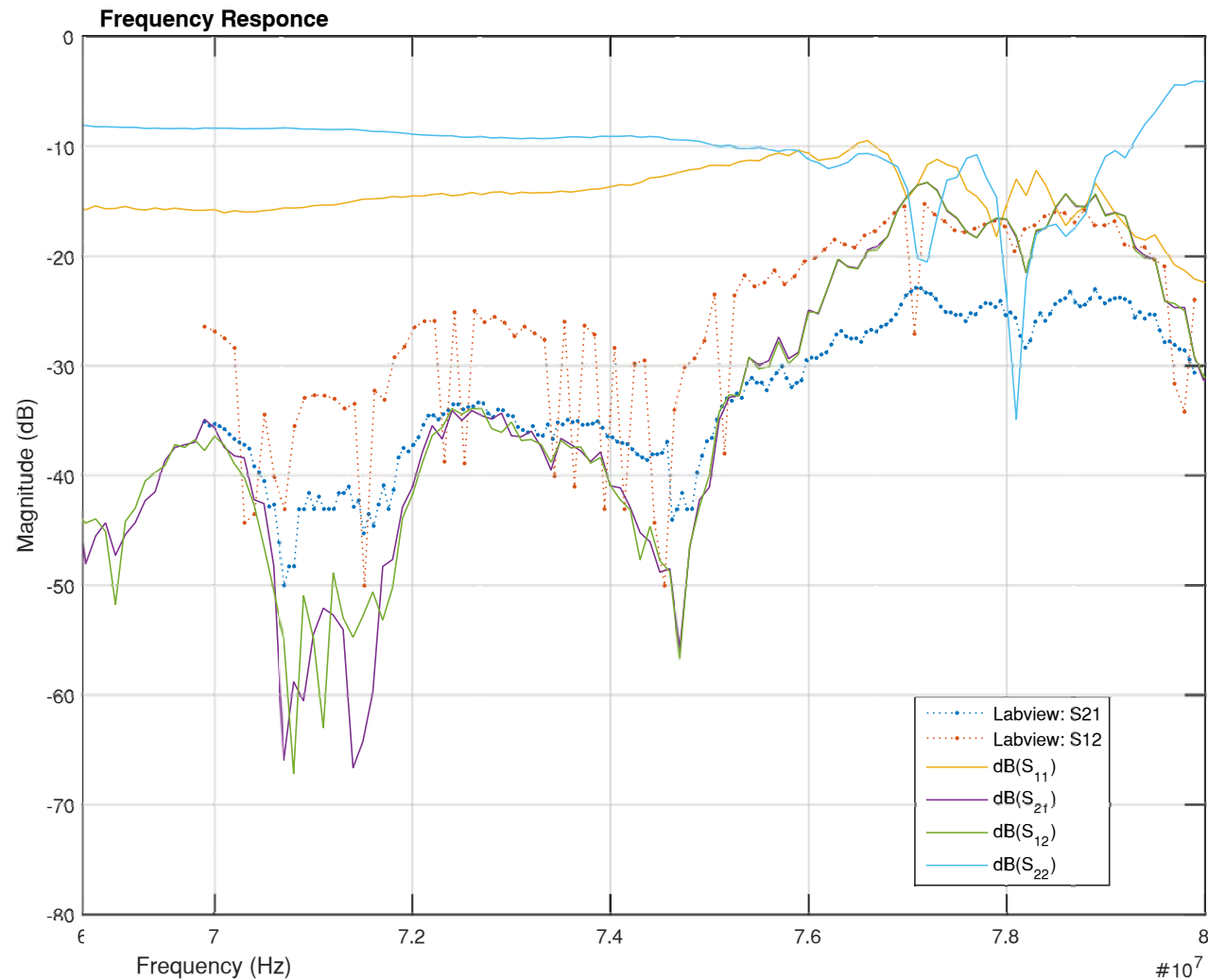
Figure 6.9: Network analysis results on 78 MHz-resonance IDT substrate. Scattering parameters obtained using a vector network analyser are plotted alongside with network analysis results from the LabVIEW program. The LabVIEW program has no functionality to measure reflection coefficients, but transmittance coefficients are largely representative. The measurements made using the LabVIEW program should primarily be used to detect irregularities. Data collection courtesy of Ole Andreas Kivik Kavli, NTNU

Chapter 7

Conclusion and Outlook

7.1   Conclusion

In this thesis, a numeric model has been developed, and introductory steps have been taken into investigating the validity of the hard wall condition as an approximation of borosilicate glass and the lossy wall condition as an approximation for Sylgard 184 polydimethylsiloxane. This has been done partly by examining the acoustic fields resulting arising from using the boundary conditions with their counterparts found in simulations where the linear elasticity of solid was implemented, and partly by comparing the imposed conditions to the actual conditions again from the full model counterparts. As the numeric model is quite computationally heavy, only indicative results have been found so far, and further investigation is necessary.

The hard wall was found to be a reasonable approximation to obtain an idea of acoustic fields within a fluid bounded by borosilicate glass, if the thickness was $1500\,\mu\text{m}$ or above. The app earance of acoustic field could be well approximated at lower thicknesses when actuated at a resonant frequency. However, if exact values are needed, the entire system ought to be modelled, as these depends on system resonance, and the hard wall may over- or underestimate the actual value. This was supported by the comparison between imposed conditions and actual conditions, for which resonance of the solid structure comes into play.

The lossy wall condition was deemed to not approximate the motion of PDMS walls in a microdevice. The resulting acoustic fields showed large differences, and the predicted velocity of the walls was very different from the one found, when modelling the PDMS. Also, unlike the borosilicate glass, acoustic fields within a fluid bounded by PDMS do not seem to converge with increasing material thickness.

Meanwhile, during a stay at the Norwegian University of Science and Technology (NTNU) a piece of software was developed to ease experimental work performed at the Microfluidics Research Group. The software collects all instrument control in a single screen and automates experiments and data acquisition and allows remote monitoring of experimental set-ups. A supplemental microdevice quality assurance program was also developed to be used in conjunction with the automation software.

While microdevice-related technical difficulties have interfered with data acquisition, preventing an experimental validation of the numeric model, the program has been extensively

used by other members of the microfluidics group, working on other microfluidic experiments.

7.2   Outlook

The thesis has a high degree of preparatory work in it, as a PhD fellowship is planned to follow up on the work done here. Thus, concrete steps are planned to improve on both the numeric model and the automation program.

Experimental validation

To truly carry on with the numeric model, it is necessary to experimentally verify it, with regards to modelling PDMS, as the results found from simulations seem strange. This can be done by running stop-flow experiments using the automation software, and capturing images of the acoustophoresis. From this, the pressure amplitudes within the chip can be found, as described in Ref. [23]. Comparison between the pressure fields found in experiments and numeric model should hopefully verify the model.

Numeric model

The discontinuities in stress observed in 3.4.1, and slight assymetries observed in Fig. 6.8, must be dealt with. While they do not seem to influence over-all convergence, it is undesirable to include discontinuities of any form in simulations. In order to better simulate the experiments carried out at NTNU, implementing seconrd order acoustic fields and piezoelectricity in the numeric model is the first priority. By including second order acoustic fields, the numeric model will also be applicable to smaller particles, while implementing piezoelectricity can give insight into the degree of displacement decay occurring along the PDMS-piezo interface. Beyond that, it may be necessary to implement PDMS acoustothermal heating to simulate the dissipation of kinetic energy to thermal energy.

Automation program

A planned improvement of the automation is a live image analysis. Based on this, it will be possible to implement a logic in the program, allowing it to regulate the flow and field factors on its own and measure the corresponding particle purification, if image contrast is sufficiently high, which is the case for fluorescent particles.

Boundary condition testing

As only a scarce amount of boundary condition results was achieved, a lot more testing is necessary to definitely comment on their validity. This mainly requires time and computational power,

Appendix A

Manuscript on PDMS hydrophilicity testing submitted to tips on chips

Simple and Low-cost Contact-Angle Measurements Using a Smartphone with a PDMS-Lens

Jonas M. Ribe[a], Nils R. Skov[b], Ole-Andreas K. Kavli[a]

[a] Department of Physics, Norwegian University of Science and Technology (NTNU) – Trondheim, Norway

[b] Department of Physics, Technical University of Denmark (DTU) - Lyngby, Denmark

Why Is This Useful?

Contact angle measurements are important for characterizing surface interactions with liquids. In microfluidics they are of special interest as they provide insight into the hydrophilic and hydrophobic properties of materials used for making microchannels. In addition, they are important for assembling polydimethylsiloxane (PDMS) devices. A common problem with PDMS devices is getting consistent good plasma bonding. For optimal plasma bonding the contact angle of the oxygen plasma treated PDMS with water should be minimized as shown by Bhattacharya S. et al.[1] However, measuring contact angles with high precision requires a quite bulky and expensive setup, but here we show a method for measuring contact angles only using materials and tools found in a typical microfluidics lab.

What do I need?

- Smartphone
- PDMS (Sylgard 184 kit)
- Plastic cup
- Plastic spoon
- Digital scale
- Desiccator with vacuum pump
- Plastic pipette
- Glass coverslip
- Oven
- Scotch tape
- Syringe pump (*optional*)
- Microscope slides
- Light source
- Adjustable pipette (0.5–1µL)
- DI water

What do I do?

1. Mix a small amount of Sylgard 184 PDMS (10:1) in a plastic cup using a plastic spoon
2. Put the plastic cup with the PDMS in the desiccator and pump down to remove the bubbles
3. Put a small droplet of uncured PDMS on the glass coverslip
4. Mount the cover slip upside down (e.g. between two glas slides) and cure the PDMS at 70°C for 15 min.
5. Center the PDMS lens over the camera of your smartphone and attach it using tape. *Tip: you can also remove the PDMS lens from the coverslip and place it directly on your camera, but it might be more difficult to center.*
6. Test the focus of your camera. For our camera setup the best images were taken with lenses that focus around 1–2cm.
7. Make a sample stage preferably using a syringe pump or some other system you can move. We mounted the smartphone on the syringe holder block with the camera pointing towards the pusher block. Make a sample holder on the pusher block using glass slides or other consumables found in the lab. Align the center of the stage with the center of the camera. *Tip: aligning is a lot easier if done using the sample you want to measure. Put the sample on the block and move it into focus by releasing the pusher block and sliding it away/towards the camera. Increase the height of the stage until the top of sample is centered in the camera.*
8. Place the light source behind the sample and illuminate the stage evenly. *Tip: put the sample stage in front of a white wall and light up the wall.*
9. Place a small drop (0.5–1µL) of DI water on top of the sample using an automatic pipette. Place the drop near the sample edge closest to the camera.
10. Move the sample edge into focus. Turn off the lights in the room and take an image. *Tip: make a box around your sample with an opening in the back to block any other light, but your light source to improve the lighting conditions.*

11. Measure the contact angle of the drop in the image e.g. using ImageJ[3] software with a plugin for contact angle measurements[4] or get a rough estimate using an app on your smartphone[5].
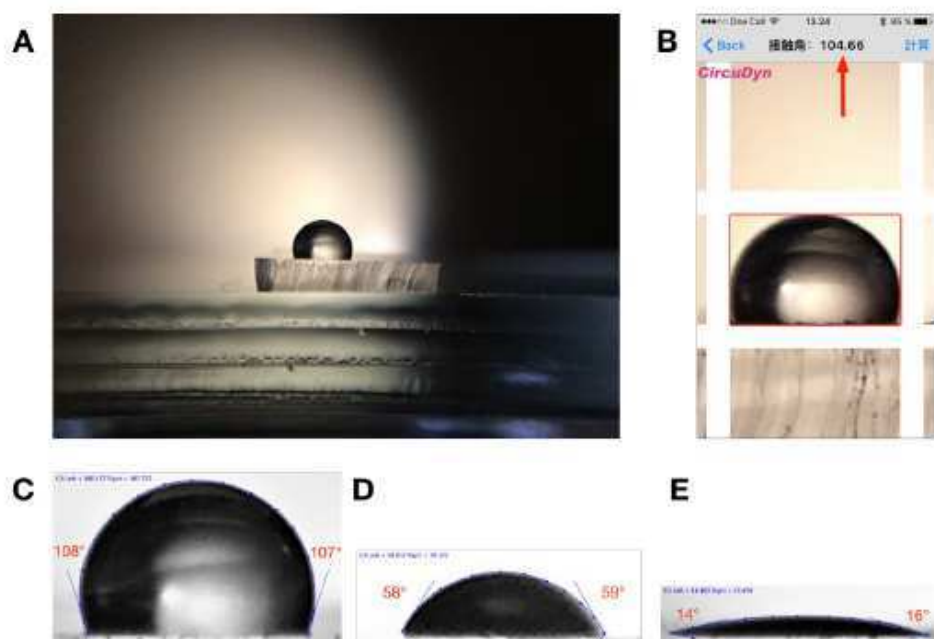
Contact angle measurements of water on PDMS: A) Raw image from iPhone 6S front-facing camera with PDMS-lens. B) Direct measurement using app on smartphone (based on θ/2 calculation) C-E) ImageJ measurements using DropSnake plugin. Unmodified PDMS (C) and PDMS treated with oxygen plasma with increasing intensity(D-E).

What else should I know?

The focal length of the PDMS lens is determined by the volume of PDMS used as described by Lee *et al*[5]. However, it is difficult to control the volume of PDMS using a pipette due to the high viscosity of PDMS. We recommend making a range of lens sizes and testing them on your smartphone camera to see which gives the right focal length. If your digital scale has milligram precision you can use it to measure the amount of PDMS used for each lens. You can add PDMS to an already cured lens to decrease the focal length further. Modern smartphones have both a rear-facing and a front-facing camera and in our experience the crop on the front facing was better for taking focused images of drops. The images taken here were done with an iPhone 6S using the front-facing camera with a 5MP sensor.

Calculating the contact angle from images of sessile drops can be done in multiple ways. A simple estimate can be made by calculating the angle between the base of the droplet and the

height of the droplet and multiplying that number by 2. This is referred to as the θ/2-method and is e.g. implemented by the Contact Angle Measurement app[4] for iOS. More accurate measurements typically rely on curve fitting of the droplet outline. This assumes that the drop has an elliptic (hydrophilic) or circular (hydrophobic) shape. The ImageJ[2] and DropSnake[3] plugin use active contours (energy minimization) to track the outline of the drop and calculate contact angles. This increases reliability, but is slower and in some cases not worth the added complexity considering the precision of the described setup.

References

1. Bhattacharya S. *et al*. Studies on surface wettability of poly(dimethyl) siloxane (PDMS) and glass under oxygen-plasma treatment and correlation with bond strength. *J. Microelectromech. S.* **14**, 590–597 (2005)
2. ImageJ software
3. DropSnake ImageJ-plugin for contact angle measurements
4. Contact Angle Measurement iOS app (*Japanese*)
5. Lee, W. M. *et al*. Fabricating low cost and high performance elastomer lenses using hanging droplets. *Biomedical Optics Express* **5**, 1626–1635 (2014)

Bibliography

[1] N. Nama, R. Barnkob, Z. Mao, C. J. Kähler, F. Costanzo, and T. J. Huang, *Numerical study of acoustophoretic motion of particles in a pdms microchannel driven by surface acoustic waves.* Lab Chip **15**, 2700 (2015).

[2] H. Bruus, *Acoustofluidics 7: The acoustic radiation force on small particles.* Lab Chip **12**, 1014–1021 (2012).

[3] J. T. Karlsen and H. Bruus, *Forces acting on a small particle in an acoustical field in a thermo-viscous fluid.* Physical Review E **92**(4) (2015).

[4] A. Liga, A. D. B. Vliegenthart, W. Oosthuyzen, J. W. Dear, and M. Kersaudy-Kerhoas, *Exosome isolation: a microfluidic road-map.* Lab Chip **15**(11), 2388–2394 (2015).

[5] J. W. Strutt (Lord Rayleigh), *On waves propagated along the plane surface of an elastic solid.* Proceedings of the London Mathematical Society **17**(1), 4–11 (1885).

[6] M. Settnes and H. Bruus, *Forces acting on a small particle in an acoustical field in a viscous fluid.* Physical Review E **85**(1) (2012).

[7] K. Lee, H. Shao, R. Weissleder, and H. Lee, *Acoustic purification of extracellular microvesicles.* ACS Nano **9**(3), 2321–2327 (2015).

[8] R. Guldiken, M. C. Jo, N. D. Gallant, U. Demirci, and J. Zhe, *Sheathless size-based acoustic particle separation.* Sensors **12**(12), 905–922 (2012).

[9] Y. Chen, A. A. Nawaz, Y. Zhao, P.-H. Huang, J. P. McCoy, S. J. Levine, L. Wang, and T. J. Huang, *Standing surface acoustic wave (SSAW)-based microfluidic cytometer.* Lab on a Chip **14**(5), 916 (2014).

[10] J. Shi, H. Huang, Z. Stratton, Y. Huang, and T. J. Huang, *Continuous particle separation in a microfluidic channel via standing surface acoustic waves (SSAW).* Lab on a Chip **9**(23), 3354 (2009).

[11] M. C. Jo and R. Guldiken, *Active density-based separation using standing surface acoustic waves.* Sensors and Actuators A: Physical **187**, 22–28 (2012).

[12] F. Guo, Z. Mao, Y. Chen, Z. Xie, J. P. Lata, P. Li, L. Ren, J. Liu, J. Yang, M. Dao, S. Suresh, and T. J. Huang, *Three-dimensional manipulation of single cells using surface acoustic waves.* Proceedings of the National Academy of Sciences **113**(6), 1522–1527 (2016).

[13] D. Köester, *Numerical simulation of acoustic streaming on surface acoustic wave-driven biochips.* SIAM Journal on Scientific Computing **29**(6), 2352–2380 (2007).

[14] T. L. Fabio Garofalo and H. Bruus, *Performance study of acoustophoretic micro uidic silicon-glass devices by characterization of material- and geometry-dependent frequency spectra*, unpublished as of 18 March.

[15] H. Bruus, *Acoustofluidics 2: Perturbation theory and ultrasound resonance modes.* Lab Chip **12**, 20–28 (2012).

[16] K. Khanafer, A. Duprey, M. Schlicht, and R. Berguer, *Effects of strain rate, mixing ratio, and stress–strain definition on the mechanical behavior of the polydimethylsiloxane (pdms) material as related to its biological applications.* Biomedical Microdevices **11**(2), 503–508 (2008).

[17] I. D. Johnston, D. K. McCluskey, C. K. L. Tan, and M. C. Tracey, *Mechanical characterization of bulk sylgard 184 for microfluidics and microengineering.* J. Micromech. Microeng. **24**(3), 035017 (2014).

[18] B. H. Ha, K. S. Lee, G. Destgeer, J. Park, J. S. Choung, J. H. Jung, J. H. Shin, and H. J. Sung, *Acoustothermal heating of polydimethylsiloxane microfluidic system.* Sci. Rep. **5**, 11851 (2015).

[19] C. P. Nielsen, *Introduction to weak form modeling in comsol.* Note on weak form and COMSOL implementation. version 1.3.

[20] P. B. Muller, R. Barnkob, M. J. H. Jensen, and H. Bruus, *A numerical study of microparticle acoustophoresis driven by acoustic radiation forces and streaming-induced drag forces.* Lab on a Chip **12**(22), 4617 (2012).

[21] H. Bruus, *Acoustofluidics 1: Governing equations in microfluidics.* Lab Chip **11**, 3742 – 3751 (2011).

[22] S. D. E. Karl T. Ulrich, *Product Design and Development* (MCGRAW HILL BOOK CO) (2011).

[23] R. Barnkob, P. Augustsson, T. Laurell, and H. Bruus, *Measuring the local pressure amplitude in microchannel acoustophoresis.* Lab Chip **10**(5), 563–570 (2010).

[24] H. Bruus, *Acoustofluidics 10: Scaling laws in acoustophoresis.* Lab Chip **12**, 1578–1586 (2012).

[25] D. S. M. M. E. P. R. J. W. Cook, Robert D., *Concepts and Applications of Finite Element Analysis* (John WIley & Sons) (2002).

[26] F. Garofalo, T. Laurell, and H. Bruus, *Performance study of acoustophoretic micro uidic silicon-glass devices by characterization of material- and geometry-dependent frequency spectra.* Manuscript in preparation (2016).

[27] M. W. H. Ley and H. Bruus, *Continuum modeling of hydrodynamic particle-particle interactions in microfluidic high-concentration suspensions.* Lab Chip (2016).

[28] Z. Mao, Y. Xie, F. Guo, L. Ren, P.-H. Huang, Y. Chen, J. Rufo, F. Costanzo, and T. J. Huang, *Experimental and numerical studies on standing surface acoustic wave microfluidics.* Lab Chip **16**(3), 515–524 (2016).

[29] M. K. Tan, J. R. Friend, O. K. Matar, and L. Y. Yeo, *Capillary wave motion excited by high frequency surface acoustic waves.* Physics of Fluids **22**(11), 112112 (2010).

[30] M. Travagliati, R. Shilton, F. Beltram, and M. Cecchini, *Fabrication, operation and flow visualization in surface-acoustic-wave-driven acoustic-counterflow microfluidics.* Journal of Visualized Experiments (78) (2013).